GEORG-AUGUST-UNIVERSITÄT
GÖTTINGEN

Fakultät für
Physik

Master's Thesis

Untersuchung von physikalischen Zusammenhängen mit Bezug auf den Kinematic Likelihood Fitter der ATLAS Kollaboration sowie die Entwicklung neuer Transferfunktionen für 13 TeV Kollisionen des Large Hadron Colliders

Studies on physical aspects related to the performance of the Kinematic Likelihood Fitter for the ATLAS collaboration including the development of new transfer functions for the 13 TeV run of the Large Hadron Collider

prepared by

Fabian Sohns

from Hameln

at the II. Physikalischen Institut

Thesis number: II.Physik-UniGö-MSc-2017/03

Thesis period: 1st October 2016 until 31st March 2017

First referee: Prof. Dr. A. Quadt

Second referee: Prof. Dr. S. Lai

Abstract

KLFitter ist ein wichtiges Hilfsmittel im Gebiet der Top-Quark Physik. Mithilfe einer Wahrscheinlichkeitsfunktion werden Objekte, die im Detektor gemessen wurden, den Objekten aus dem direkten Zerfall zugeordnet. Zum einen werden rekonstruierte kinematische Größen mittels Transferfunktionen auf das Parton-Level abgebildet. Hierbei werden Variationen der gemessenen kinematischen Größen im Rahmen der Detektorauflösung, der Hadronisierung und der Showerbildung erlaubt. Zum anderen werden die Breit-Wigner-Funktionen der Top-Quark- und W-Boson-Massen aus den Parton-Level-Objekten gebildet. Für jede Permutation von rekonstruierten Objekten wird die Wahrscheinlichkeitsfunktion maximiert und die Permutation mit dem höchsten Wert ausgewählt. Die Entwicklung der Transferfunktionen für $\sqrt{s} = 13\,\text{TeV}$ erfolgt mit dem Ziel, sämtliche Rekonstruktions- und Schwelleneffekte analytisch zu beschreiben. Nach einem allgemeinen Überblick der Physik des Top-Quarks und des ATLAS Detektors werden Effizienzstudien mit Bezug auf KLFitter vorgestellt. Es wird gezeigt, dass kinematische Schnitte die Performanz von KLFitter limitieren. Im zweiten Teil wird ein Überblick über die Entwicklung der Transferfunktionen für Jets gegeben. Mit TFTool, einem für die Entwicklung von Transferfunktionen entwickeltes Hilfsmittel, werden physikalische Effekte, die wesentlich zum Auflösungsspektrum beitragen, erklärt und beschrieben. Abschließend wird eine Übersicht über die Implementierung der relevanten physikalischen Effekte und damit verbundenen Problemen in TFTool gegeben.

Abstract

The kinematic likelihood fitter KLFitter is an essential tool within the top-quark framework. By using a likelihood function, objects that are reconstructed in the detector are mapped to parton-level objects from the direct decay. This is done by assigning kinematic properties to parton-level via transfer functions. Here, variations of the measured quantities within the detector resolution, hadronisation and fragmentation are taken into account. In addition, the Breit-Wigner functions of the top-quark and W-boson masses are formed on parton-level. For every permutation of reconstructed objects, the likelihood function is maximised and the permutation with the highest value is chosen. The development of new transfer functions for $\sqrt{s} = 13\,\text{TeV}$ aims to analytically describe all relevant reconstruction and threshold effects. After a general overview of the top-[1]quark and the ATLAS detector, efficiency studies related to KLFitter are presented. Kinematic cuts are found to limit the performance of KLFitter. In the second part, an overview of current developments of new transfer functions for jets is given. With TFTool, a tool that was developed to study the performance of transfer functions, physical aspects related to the resolution spectrum are explained and described. Finally, an overview of the current implementation of relevant physical aspects and problems in the implementation are presented.

Contents

1 Introduction

In the second half of the 20th century, several elementary particles were discovered. This raised the prospect of a fundamental theory describing their relations. As a result, the *Standard Model* (SM) of particle physics was developed over the past decades. It is presented in further detail in Chapter 2.

Several discoveries predicted by the model showed that the model describes the fundamental physics reasonably well. The discovery of the top-quark in 1995 by CDF and DØ [2, 3] completed the quark sector of the model. The discovery of a boson, in agreement with the expected properties of the Higgs boson, in 2012 by Cms [4] and Atlas [5] was another big step in the direction of a more complete model. With the theory behind the Higgs boson, developed in the 1960's, the origin of particles' masses could be explained [6–8].

It is known that the SM is not complete. Many astrophysical observations strongly suggest the existence of Dark Matter [9]. Within the SM, no particle fulfills the required properties of Dark Matter.

Another incomplete aspect of the SM is the oscillation of neutrinos. For massless neutrinos, which are assumed in the SM, an oscillation between generations is not possible. However, it was observed and is currently studied by experiments like Superkamiokande [10].

These shortcomings show that extensions of the model are necessary. One possible extension is *supersymmetry.* In superymmetric theories, additional particles related to SM particles are introduced. To test such a hypothesis, it is necessary to know the exact properties of observable particles that are already included in the SM. Along with searches for new unknown particles, this is done by measurements at collider experiments. One example is the Atlas experiment at the Lhc, further discussed in Chapter 3.

Due to its high mass and short lifetime, the top-quark is special within the SM. Hence, measuring its properties is one of the major tasks in modern particle physics. To do so, it is necessary to reconstruct events originating from a top-quark decay in the detector. The KLFitter [1] package provides a statistical method for the event reconstruction in the semileptonic channel.

Within KLFitter, transfer functions are used. They model the detector response of an incoming particle as discussed in section 4.3. In this Master's thesis, the TFTool [11] is used for the development of new transfer functions. Physical aspects related to the resolution spectra of measured particles are discussed, described and possible solutions for the implementation in TFTool are presented. In the final chapter, computational problems are discussed as well.

2 The Top-Quark in the Context of the Standard Model

The SM of particle physics describes the properties and interactions of elementary particles. It includes six leptons and six quarks, together known as *fermions*. In addition to the fermions, there are the mediators of the fundamental forces called *gauge bosons*.

In the following, an introduction of the SM will be given including short descriptions of electroweak unification in Section 2.1.1 and Quantum Chromodynamics in Section 2.1.2. The last Section 2.2 covers the theoretical aspects of top-quark physics.

2.1 Standard Model of Particle Physics

The SM is a quantum field theory with an underlying $SU(3)_C \times SU(2)_L \times U(1)_Y$ symmetry. A graphical overview is given in Figure 2.1. The 12 fermions are organised in three generations arranged by increasing mass. Each generation contains two particles, an up-type and a down-type one. They are distinguished by the third component of the weak isospin I_3 where up-type particles have a positive absolute value (see section 2.1.1). In the fermionic case, the charged leptons ($I_3 = -\frac{1}{2}$) and the corresponding neutrinos ($I_3 = +\frac{1}{2}$) form one generation each, ordered by the mass of the lepton. In the quark sector, each generation contains an up-type quark with a charge of $q = +\frac{2}{3}$ and a corresponding down-type quark with $q = -\frac{1}{3}$. The quarks have $I_3 = \pm\frac{1}{2}$. The lightest generation is made of the u- (up) and the d- (down) quark followed by the c- (charm) and the s- (strange) quarks in the second generation. Finally, the t- (top) and b- (bottom) quark form the heaviest generation in the quark sector.

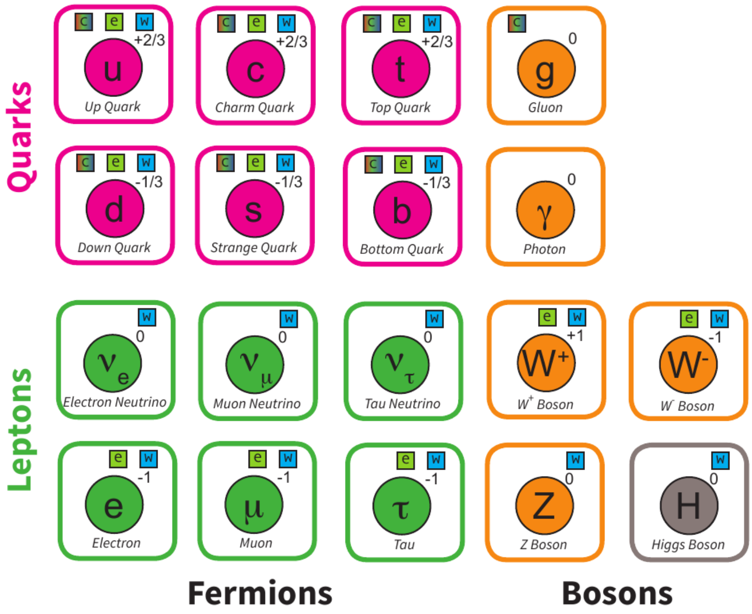

Figure 2.1: The elementary particles of the Standard Model. The small number in the upper corner represents the charge. The small boxes indicate the fields to which the particle couples (colour (c), electromagnetic (e) and weak (k)). The gauge bosons are shown as well.

2.1.1 Electroweak Unification

At first glance, the electromagnetic force seems to be completely different from the weak force. It is mediated by one single massless photon. On the other hand, weak interactions require three gauge bosons, two charged $W^{\pm}$-bosons and one neutral Z^0-boson. Both types of bosons have a significant masses of $m_W = 80.385 \pm 0.015\,\text{GeV}$ and $m_Z = 91.1876 \pm 0.0021\,\text{GeV}$ [12].

It was shown in the 1960's that there is an underlying theory which describes both phenomena. This theory was developed by Glashow [13], Weinberg [14] and Salam [15]. Hence, it is called the GWS-model. Mathematically it is based on the $SU(2) \times U(1)$ symmetry.

Before unification, the electromagnetic force was described by the $U(1)$ symmetry. In Quantum Electrodynamics (QED) the massless photon couples to all particles with a charge Q. In a field theory, it is typically represented by the field A_μ. The coupling term of interacting fermions, e.g. leptons, with spinors $l = l(p)$, can be written as

$$j^{\mu}_{em} A_\mu = g_e l \gamma^\mu l A_\mu, \tag{2.1}$$

where g_e is the electromagnetic coupling constant, j^{μ}_{em} the electromagnetic current and γ_μ the gamma matrices.

In the end of the 1950s, it was experimentally shown by Wu [16] and Goldhaber [17] that the charged weak interaction is, in contrast to all other known forces, maximally parity violating. This means that W-bosons only couple to the left-handed chiral states of fermions and right-handed states of anti-fermions. Therefore, the left (L) and right (R) handed chiral states of the weak interaction, can be represented in the following form:

$$\begin{aligned}
Q_L &= \quad \begin{pmatrix} u_L \\ d_L \end{pmatrix} \quad \begin{pmatrix} c_L \\ s_L \end{pmatrix} \quad \begin{pmatrix} t_L \\ b_L \end{pmatrix} \\
L_L &= \quad \begin{pmatrix} \nu_{e,L} \\ e_L \end{pmatrix} \quad \begin{pmatrix} \nu_{\mu,L} \\ \mu_L \end{pmatrix} \quad \begin{pmatrix} \nu_{\tau,L} \\ \tau_L \end{pmatrix} \\
u_R &= \quad u_R \quad\quad c_R \quad\quad t_R \\
d_R &= \quad d_R \quad\quad s_R \quad\quad b_R \\
\ell_R &= \quad e_R \quad\quad \mu_R \quad\quad \nu_R
\end{aligned} \tag{2.2}$$

While in the left-handed isospin doublets Q_L and L_L two components with $I_3 = \pm\frac{1}{2}$ appear, the right-handed isospin singlets carry $I_3 = 0$. When a fermion interacts with a W-boson, I_3 is changed by ±1. Such a change is only possible in the doublet. As a consequence, W-bosons cannot couple to the right handed singlets as observed in experiment. In order to describe the parity violating behaviour, the vector minus axial vector (V-A) coupling is introduced. The weak charged-current j^+_μ takes the form

$$j^+_\mu = g_W \bar{\nu} \gamma_\mu \frac{1-\gamma^5}{2} e = g_W \bar{\nu}_L \gamma_\mu e_L. \tag{2.3}$$

Here, g_W is the weak coupling constant similar to the electromagnetic one and ν/e represent the spinors for the electron and the neutrino, respectively.

By applying the operators

$$P_L = \frac{1-\gamma^5}{2} \qquad \text{and} \qquad P_R = \frac{1+\gamma^5}{2} \tag{2.4}$$

on the general chiral states, the pure states, e.g. e_L, e_R, can be obtained.

In addition to the described model, leptons and quarks couple to fermions in other generations. This effect, known as flavour-changing-charged currents, was examined in several experiments, such as the observation of charged kaon decays [18]. A description was first proposed in 1967 [19]. Cabibbo introduced the idea of relating the mass and the weak eigenstates by a rotation matrix. This idea was further developed in the following years by Kobayashi and Maskawa [20]. As a result, the CKM-matrix

$$\underbrace{\begin{pmatrix} d' \\ s' \\ b' \end{pmatrix}}_{\text{Weak eigenstates}} = \underbrace{\begin{pmatrix} V_{ud} & V_{us} & V_{ub} \\ V_{cd} & V_{cs} & V_{cb} \\ V_{td} & V_{ts} & V_{tb} \end{pmatrix}}_{\text{CKM-matrix}} \times \underbrace{\begin{pmatrix} d \\ s \\ b \end{pmatrix}}_{\text{Mass eigenstates}} \tag{2.5}$$

describes the mixing of the mass eigenstates in the weak interaction.

Current measured results of the magnitudes $|V_{ij}|$ are given below (see [12] and included references):

$$V_{CKM} = \begin{pmatrix} 0.97425 \pm 0.00022 & 0.2253 \pm 0.0008 & (4.13 \pm 0.49) \times 10^{-3} \\ 0.225 \pm 0.008 & 0.986 \pm 0.016 & (41.1 \pm 1.3) \times 10^{-3} \\ (8.4 \pm 0.6) \times 10^{-3} & (40.0 \pm 2.7) \times 10^{-3} & 1.021 \pm 0.032 \end{pmatrix}. \tag{2.6}$$

Large entries on the diagonal show that quarks dominantly interact inside their generation. The unity of the sum of the squared matrix elements in columns and rows indicates that there are only three generations even though a fourth generation could be included with small entries within the uncertainty [21].

The second part of the weak force are interactions with a Z-boson as the mediator. Opposed to the previously mentioned charged flavour changing currents, flavour changing *neutral* currents are not expected in the SM at leading order (see section 2.2). The coupling is a fermion dependent mixture of vector and axial-vector contributions. The neutral current for a fermion spinor q can be written as

$$J_\mu^{NC} = \bar{q}\gamma_\mu \frac{c_V^q - c_A^q \gamma^5}{2} q, \tag{2.7}$$

with c_V and c_A as fermion dependent parameters.

Due to the different description of the couplings, a unification of charged and neutral weak interactions seems unlikely at first glance.

However, in the electroweak unification, presented in the following, this problem is solved. As we know today, electromagnetic and weak interactions are only subtheories of a more fundamental one. By introducing the *hypercharge* Y for each fermion, defined in the relation

$$Q = I_3 + \frac{Y}{2}, \tag{2.8}$$

the isospin and the electric charge are related. Therefore, the electroweak theory unifies the $SU(2)_L$ group with a vector like $U(1)$ theory. Interaction terms can now be written in the form

$$-ig_W (J^i)^\mu W^i_\mu - i\frac{g'}{2}(j^Y)^\mu B_\mu . \tag{2.9}$$

The unified theory contains three bosonic fields W^i_μ from the $SU(2)$ group and an additional bosonic field B_μ from the $U(1)_Y$ group. Combining these fields with the mixing angle Θ_W (also known as *Weinberg angle*) leads to the known representations of the gauge bosons

$$\begin{aligned} W^\pm &= \sqrt{\frac{1}{2}}(W^1_\mu \mp W^1_\mu) \\ \begin{pmatrix} A_\mu \\ Z_\mu \end{pmatrix} &= \begin{pmatrix} \cos\Theta_W & -\sin\Theta_W \\ \sin\Theta_W & \cos\Theta_W \end{pmatrix} \times \begin{pmatrix} B_\mu \\ W^3_\mu \end{pmatrix} \end{aligned} \tag{2.10}$$

The definitions of the fermionic coupling strengths, mentioned in Equation (2.7),

$$\begin{aligned} c^f_V &= I^f_3 - 2Q_f \sin^2\Theta_W \\ c^f_A &= I^f_3 \end{aligned} \tag{2.11}$$

show the mixing of the weak force, represented by the weak isospin I_3, and electromagnetic force, represented by the charge Q. Furthermore, the coupling strengths and the masses of the W and Z bosons are also related

$$\begin{aligned} g_W &= \frac{g_e}{\sin\Theta_W} \\ M^2_Z &= \frac{M^2_W}{\cos^2\Theta_W} . \end{aligned} \tag{2.12}$$

The question that remains is the origin of the non-zero masses of the weak gauge bosons and of the fermions. The interactions of fermions can be represented by the Lagrange formalism. Introducing an explicit mass term would spoil the local gauge symmetry of the Lagrangian. A solution was provided by Robert Brout, Francois Englert and Peter Higgs, in the mid 1960s which is nowadays known as Brout-Englert-Higgs mechanism [6–8]. With the discovery of the Higgs boson in 2012 [4, 5], their proposal was further strengthened.

The mechanism requires local gauge invariance of the gauge fields as before. By introducing a new scalar field, the Higgs field, and applying spontaneous symmetry breaking, a new coupling term between fermions/bosons and the field is introduced. This *Yukawa coupling* provides mass terms for the gauge fields in the Lagrangian. Even though the mechanism is very important for a complete picture of the SM, a mathematical derivation is not provided here.

2.1.2 Quantum Chromodynamics

Quantum Chromodynamics (QCD) uses the $SU(3)$ group to describe the strong force. The *colour charge* is only carried by quarks and gluons while leptons do not interact strongly. Eight gluons (spin-1) are the exchange particles of QCD that self-interact since they carry the colour charge. Two peculiarities of the strong force, *confinement* and *asymptotic freedom*, result in a unique behaviour of the strong force [22–25].

Confinement Up to a limiting strength, the strong force does not decrease with increasing distance. This makes it quite different from all other known forces. If enough energy is stored within a gluon, it will eventually split apart. Thereby, new hadronic partons are created as sketched in Figure 2.2. In a cascade like behaviour, further gluons and hence partons are produced. The produced quarks further interact with each other to form a colourless state. This is required since coloured states are not observed in nature. As a consequence, quarks produced in processes like $t \rightarrow b + W \rightarrow b + \bar{q}q'$ are not observed as free particles but rather as a bunch of particles (known as *jets*). This makes the observation of quarks different with respect to the observation of leptons.

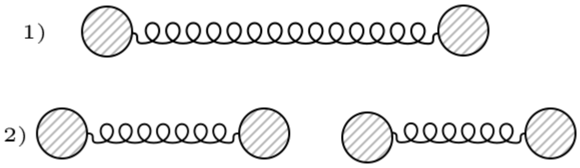

Figure 2.2: Schematic overview of hadronisation. A gluon, interacting between two partons, has enough energy stored to split into a new quark pair. This process appears many times and results in the formation of jets.

Asymptotic freedom The coupling constant α_S of the strong force depends on the energy scale q^2. It is parametrised from a known energy scale μ via the relation

$$\alpha_s(q^2) = \frac{\alpha_s(\mu^2)}{1 + \frac{11N_C - 2N_f}{12\pi}\ln(q^2/\mu^2)}, \tag{2.13}$$

where N_C and N_f are the number of colour and fermionic states available at the energy scale of interest. One consequence of this behaviour is that, for large energy scales, quarks can be assumed to be *asymptotically free*. This means that the coupling strength decreases with higher energies and interactions become less likely. On the other hand, theories that describe QCD at lower energies cannot assume quarks to be free particles. This can lead to divergences and uncertainties in calculations until perturbation theory cannot be applied anymore.

2.1.3 Fragmentation

During the production of jets, highly energetic partons form bound states of two or more quarks. These states are known as hadrons and can be further divided into mesons, if $q\bar{q}'$ form a bound state, or baryons, if three quarks are involved. In order to describe the momentum of the final state hadron, parton fragmentation functions $D_i^h(z)$ are used (also referred to as fragmentation densities) [12, 26, 27]. In principle, they are the final-state analogy to the parton distribution functions further discussed in section 2.2.1. Fragmentation functions $D_i^h(z)$ give the probability that an initial parton i fragments into a hadron h that carries a momentum fraction z of the initial state.

Since hadronisation is a non-perturbative effect and the collinear limit of parton splitting is divergent, fragmentation functions cannot be derived from first principles [27]. Non-perturbative effects are included by convolving phenomenological observations. Typically, functions of the form

$$D_i^h(z, \mu_0^2) = N z^\alpha (1-z)^\beta \left(1 + \gamma(1-z)^\delta\right) \tag{2.14}$$

are used for light quarks that can be derived from an initial energy scale μ_0^2. The parameters α, β, γ, δ as well as the normalisation N, given by

$$\sum_h \int_0^1 dz\, z\, D_i^h(z, \mu^2) = 1, \tag{2.15}$$

depend on the energy scale μ^2, the initial-state quark i and the final state hadron h. Their exact values must be evaluated by experiments. Such a measurement is particularly suited for an e^+e^--collider because of the fixed and known centre-of-mass energy in each e^+e^- collision.

For heavy quarks, the fragmentation is expected to be much harder with the limit for very heavy quarks where the hadron carries all the energy of the initial quark [28]. Furthermore, when a heavy quark is produced with a much higher energy than its rest mass, further perturbative effects intervene and have to be considered in the shape of the fragmentation function. Since this procedure is not always straight forward parametrisations can be used [27]. This leads to several possible parametrisation functions of which the Peterson fragmentation [29]

$$D_i^h(z) \propto \frac{1}{z(1 - 1/z - \epsilon/(1-z))^2}, \tag{2.16}$$

is one of the most common ones [12]. The normalisation again must be considered from boundary conditions, such as the cross-section of all hadrons that contain the initial quark i. The parameter ϵ gives the hardness of the quark considered and has to be extracted from experiment. This accounts for different Example values are $\epsilon_c = 0.05/0.035$ [30, 31] and $\epsilon_b = 0.006/0.0033$ [32] for different calculations (leading/second order).

2.2 Top-Quark Physics

The role of the top-quark within the SM is unique, not only because of its properties but also because of its meaning for physics in and beyond the SM.

In 1973, Kobayashi and Maskawa [20], two of the developers of the CKM matrix, proposed to expand the quark sector by a third generation. This was one possibility to explain the CP violation observed in the 1960s by Cronin et al. [33]. With the discovery of the τ lepton, the third generation lepton, at SLAC [34] and the bottom-quark in 1977 at Fermilab [35], a third generation in the quark sector was very likely. The reasons are the following: The GIM mechanism, proposed by Glashow, Iliopoulos and Maiani in 1970 [36], predicted the existence of a charm-quark. Four years later the second up-type quark was discovered, a strong indication that the mechanism works. Within the theory, flavour changing neutral currents (FCNC) are naturally suppressed and processes with strangeness changes are explained. Originally, the GIM mechanism uses two quark generations, but, from a mathematical point of view, is easily expanded to three doublets.

Since the b-quark was already discovered, there were only two possible types of models, with or without the top-quark. Without a partner for the bottom-quark, the representation would be a singlet, and not a doublet as we know today. However, for the GIM mechanism this would mean that the natural suppression of FCNC would be spoiled. This was excluded from measured limits of FCNC, e.g by the UA1 collaboration. A $SU(2)$ singlet bottom-quark was excluded [37–41].

The second strong argument for the existence of a top-quark is renormalisation of the electroweak theory [13–15, 42]. Keeping the model free of anomalies, e.g. during electroweak unification, is an absolute precondition and unavoidable to proof the correctness of the theory. If quarks exist in three colour states, as it is known today, freedom of anomalies can only be achieved if the number of leptons equals the number of quarks. From measurements at the Large Electron Positron collider (LEP), it is known that three light neutrino generations exist [43] and therefore the discovery of the τ lepton strongly indicates that there must be a doublet partner for the bottom-quark in order to sustain renormalisability.

Roughly 18 years after the discovery of the bottom-quark, the CDF and DØ collaborations with experiments located at the TEVATRON claimed the discovery in 1995 [2, 3]. Nowadays, the exclusion of the $q_t = -\frac{4}{3}$ hypothesis [44, 45] as well as the measurements of spin correlations [46] strongly indicate that the detected particle is the SM top-quark. A recent publication of ATLAS [47] in $\sqrt{s} = 8\,\mathrm{TeV}$ data measured the top mass to be

$$m_t = 172.84 \pm 0.34\,(\mathrm{stat}) \pm 0.61\,(\mathrm{syst})\,\mathrm{GeV}. \tag{2.17}$$

It was confirmed that the top-quark is the heaviest particle in the SM. The mass distribution follows the Breit-Wigner function, a statistical probability function which describes resonances in high energy physics [48, 49]. With a width of [12, 50]

$$\Gamma_t \overset{(@NLO)}{=} \frac{G_F m_t^3}{8\pi\sqrt{2}} \left(1 - \frac{M_W^2}{m_t^2}\right)^2 \left(1 + 2\frac{M_W^2}{m_t^2}\right) \left[1 - \frac{2\alpha_s}{3\pi}\left(\frac{2\pi^2}{3} - \frac{5}{2}\right)\right] = 1.3\,\mathrm{GeV} \tag{2.18}$$

and the resulting extraordinarily short lifetime $\tau_t = \frac{\hbar}{\Gamma_t} = 5 \times 10^{-25}\,\mathrm{s}$, the top-quark decays before it forms bound states ($\tau_{hadronise} \approx 10^{-23}\,\mathrm{s}$) [51]. This allows for measurements of direct decay products from a bare quark without the influence of the strong interaction. This makes the top-quark special in comparison to other quarks and worth studying in detail.

2.2.1 Top-Quark Production

The top-quark can be produced as a $t\bar{t}$-pair in the strong interaction or as a single quark via the weak interaction. The possible leading order Feynman diagrams are shown in Figure 2.3 and Figure 2.6. Pair production is the dominant mechanism at hadron colliders such as the TEVATRON and the LHC due to the different production mechanisms.

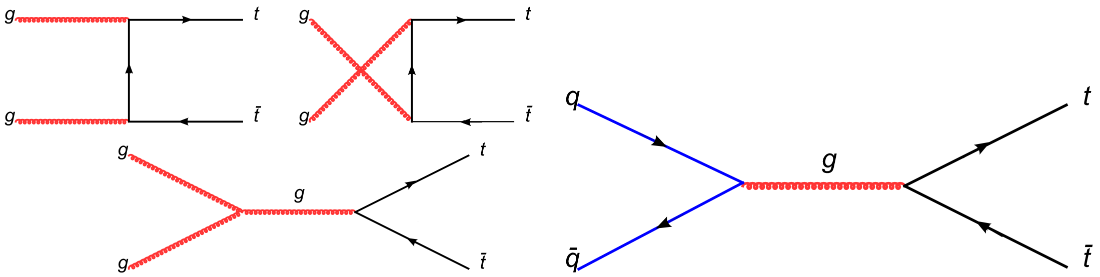

(a) gg-fusion (b) qq-annihilation

Figure 2.3: Top-quark pair production channels at leading-order in the strong interaction. The dominant process at the LHC is the gluon-gluon fusion shown in Figure (a). The dominant process at the TEVATRON was the annihilation of two quarks, sketched in Figure (b).

Using the factorisation theorem, the inclusive cross-section of top-quark pair production can be calculated. Figure 2.4 shows *Parton Distribution Functions* (PDFS) $f_i(x_i, \mu_f^2)$ from the ATLAS experiment for a factorisation scale of $\mu_f^2 = 30000\,\text{GeV}^2 \approx m_t^2$. By convolving the PDFs with the partonic cross-section $\hat{\sigma}$, the cross-section for the $pp \rightarrow t\bar{t}$ LHC production process can be written as [52]

$$\sigma_{t\bar{t}}(\sqrt{s}, m_t) = \sum_{k,l=q,\bar{q},g} \int dx_k\, dx_l\, f_k(x_k, \mu_f^2) f_l(x_l, \mu_f^2) \times \sigma_{kl\rightarrow t\bar{t}}(\hat{\text{s}}, x_k, x_l, m_t, \mu_f, \alpha(\mu_f^2)). \tag{2.19}$$

Here, x_i gives the fraction of the total $\sqrt{s}$ carried by a single parton. Hence, $\hat{\text{s}} = x_k x_l s$ denotes the effective squared centre-of-mass energy in a parton parton collision at a centre-of-mass energy s in the proton proton frame.

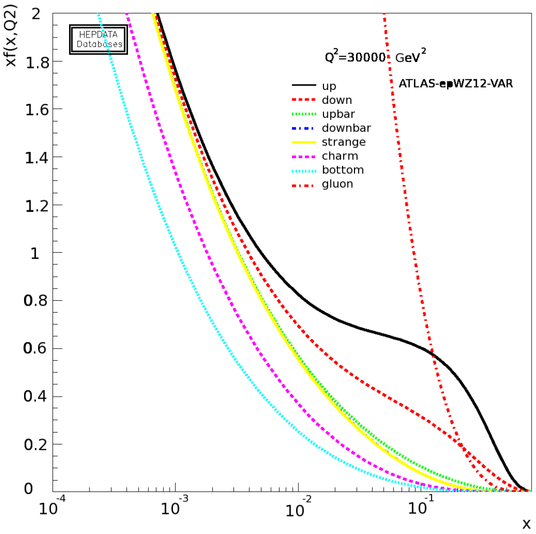

Figure 2.4: Parton distribution functions for several partons as a function of the Bjorken-x for $\mu_f^2 = Q^2 = 30000\,\text{GeV}^2$. The parton distribution functions are generated with [53] for the ATLAS group ATLAS-epWZ12-VAR set.

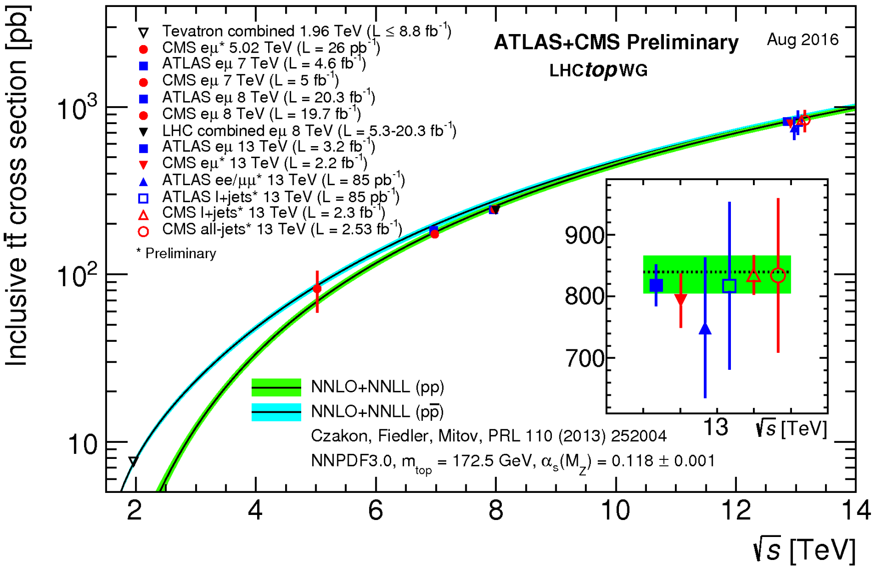

Figure 2.5: Summary of LHC and Tevatron measurements of the top-pair production cross-section as a function of the centre-of-mass energy compared to the NNLO QCD calculation complemented with NNLL resummation (top++2.0). The theory band represents uncertainties due to renormalisation and factorisation scale, parton density functions and the strong coupling. The measurements and the theory calculation are quoted at m_{top}=172.5 GeV. Measurements made at the same centre-of-mass energy are slightly offset for clarity. Figure taken from [54].

A recent summary of cross-section measurements from the LHC and TEVATRON experiments is given in Figure 2.5. Comparing the TEVATRON and the LHC shows that due to the difference in $\sqrt{s}$ the dominant processes on parton-level changed. At the TEVATRON ($\sqrt{s} = 1.96\,\text{TeV}$ in Run II), momentum fractions on the order of 0.2 were necessary resulting in 85 % of top-quarks being produced by *$q\bar{q}$-annihilation* (Figure 2.3(b)). The average momentum fraction for $\sqrt{s} = 13 - 14\,\text{TeV}$ proton-proton collisions is much smaller and therefore, as can be seen in Figure 2.4, gluon-gluon fusion is the dominant production process with ≈ 90 % at the LHC (Figure 2.3(a)).

Single top-quark production becomes important for measurements of the top-quark couplings, further discussed in Section 2.2.3 [55]. There are three different channels at leading order, sketched in Figure 2.6, namingly the s-channel, t-channel and the W associated production. The large irreducible background complicated the TEVATRON searches for single top production. In 2009, however, CDF and DØ announced the observation of single top production processes [56, 57]. Nowadays, single top processes are used for top-quark precision studies in electroweak interactions [58].

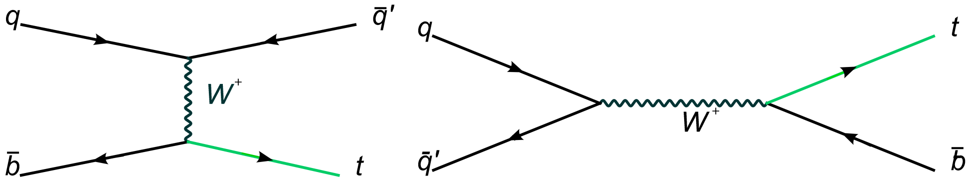

(a) t-channel (b) s-channel

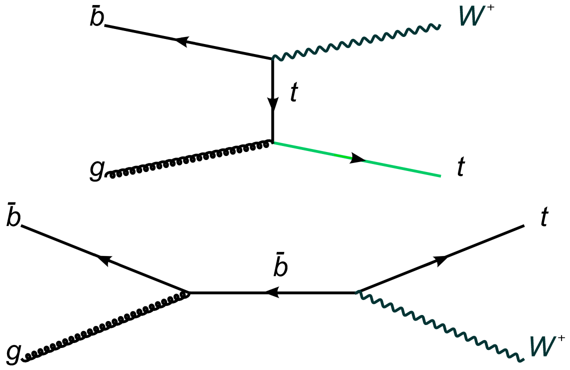

(c) associated W

Figure 2.6: Feynman diagrams at leading order in case of single top production in the t-channel (a) and s-channel (b) modes via the weak interaction. Figure (c) shows the production with an additional W-boson known as associated production.

2.2.2 Decay Channels

The top-quark predominantly decays via the weak interaction into a W-boson and an additional down-type quark. The large CKM-matrix entry of $|V_{tb}| \approx 1$ indicates that the decay almost exclusively results in a b-quark. The decay modes, shown in Figure 2.7, are therefore defined by the W-boson decay products [12].

An depiction of the $t\bar{t}$ branching ratios is shown in Figure 2.8. The values are estimated from the following considerations of the W-boson decay and are in agreement with measurements [12]. Simplified, cross-family couplings in the W-decay can be neglected. This leaves only two quark generations, since the W-boson cannot decay into the third quark generation for kinematic reasoning, and the three lepton generations as possible final states. In addition, quarks can take three different colour states and are therefore three times as likely to be produced. This leads to a ratio of 2:1 between hadronic decays and the leptonic ones. The obtained ratios can be applied to the $t\bar{t}$ decay where two additional down-type quarks need to be respected. From this, the decay channels with the fractions given in Figure 2.8 are obtained.

For two top-quarks, the decay channels can be grouped into three different types, *all-hadronic*, *semileptonic* and *dileptonic* decays [12].

With 46% of decays, the all-hadronic channel dominates. However, due to a large background originating from QCD multijet events, it can be difficult to distinguish background from signal in the analysis.

The dileptonic channel, where both W-bosons decay into either an electron or a muon, offers a good separation between signal and background. On the contrary, the branching ratio is significantly smaller compared to the all-hadronic channel. However, at the LHC,

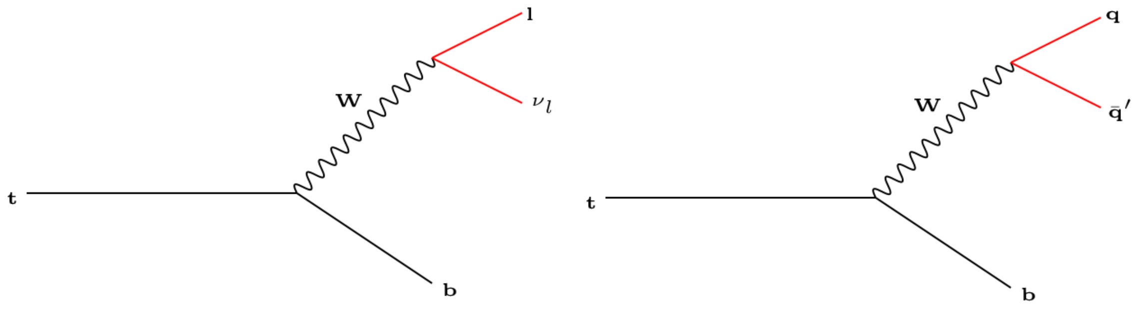

(a) leptonic decay (b) hadronic decay

Figure 2.7: The decay channels of the W-boson define the final states of the top-quark decay. There are two possible decays, either into a lepton and the corresponding neutrino (Figure (a)) or hadronically into an up- and a down-type quark (Figure (b)).

enough top-quark pairs can be produced to compensate for the small branching ratio. What remains are two neutrinos in the final state which decreases the kinematic reconstruction. τ leptons are not directly observed and need to be considered separately.
The same argument holds for the semileptonic channel, often referred to as "golden channel". τ leptons either decay into lighter leptons or form additional jets which need to be distinguished from the all-hadronic case. Semileptonic events offer good statistics with good reconstruction properties. Since there is only one neutrino, the missing energy corresponds to the neutrino energy. Therefore, this channel is often used in analysis.

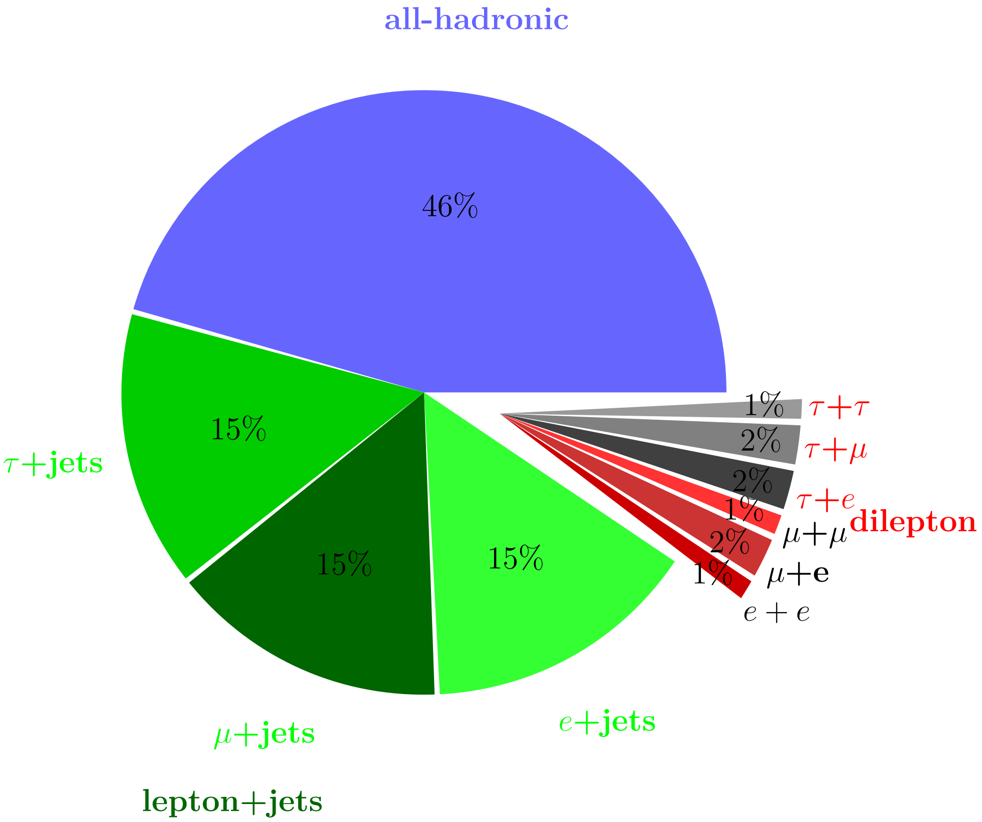

Figure 2.8: Estimated decay rates of top pairs which are in agreement with measurements. The different channels can be grouped into all-hadronic, dileptonic and semileptonic decays which have different (dis-)advantages in analyses.

2.2.3 Top-Quark Couplings

The high mass, which corresponds to a Yukawa coupling of almost one, might play a special role in searches for physics beyond the SM, e.g. in supersymmetric models with more than one Higgs boson which preferably couple to heavy particles [6–8, 59, 60].

Within the SM, top-quarks are important in the Higgs boson production [61–63]. In gluon-gluon fusion, a loop is needed to generate a Higgs boson since no direct coupling to the massless gluons is possible. These loops are dominated by heavy particles and therefore by top-quarks in the SM. This means that the tH coupling influences the Higgs boson production cross-section and is therefore worth studying [64].

In principle, heavy particles not observed yet can also participate in these loops. Knowing the tH coupling precisely therefore helps in searches for new physics.

The direct coupling of the top-quark to the Higgs boson can be observed with tH or $t\bar{t}H$ in the final state. For Atlas and Cms these are intensively studied processes.

Couplings are important properties of the quark itself. The top-quark passes its spin information on the decay products. This is a unique feature of the top-quark in the quark sector since it decays before hadronisation. By measuring the angular distribution of the W-bosons, the fraction of the left-/right-handed and longitudinal polarised states can be measured. Comparing the measurements of the W polarisation with theoretical predictions from a SM top-quark, a validation of the SM tWb coupling is possible.

Since the top-quark carries an electrical charge, it interacts with photons. Measuring this process is important in searches for new physics [65–68]. It is best observed with an additional photon in the final states. The photon can be observed as an additional electromagnetic cluster in the electromagnetic calorimeter. Unfortunately, photons can be radiated by any charged particle, making a distinction from background processes difficult. The radiation of an additional Z-boson in the final state is a similar process worth being studied and allows insight into the weak coupling [69].

3 Experimental Setup

Typically, processes that are relevant for SM physics cannot be freely observed in nature with a significant number of events. To provide enough statistics for high energetic events under controlled conditions, particle accelerators are used. With the shutdown of the Tevatron in 2011, the Lhc [70–73] is the only remaining accelerator able to produce top-quarks. The Atlas experiment [74] is one of the four larger experiments located at the accelerator. In the same way as particle accelerators are needed to produce high energetic particles, special detectors are needed to detect the decay products of rare processes. Reconstructing the decay products then allows to test the SM. Atlas and Cms are general purpose detectors. This allows for cross-checks of measurements between the experiments and studies of almost all processes that are interesting in modern high energy physics. In this chapter, an overview of the accelerator and the key properties of the Atlas detector is given.

3.1 Large Hadron Collider

From 1989 until 2000 the Lep collider was used at the research facility Cern in Geneva. Nowadays, the 27 km long tunnel is used for the Lhc. In two beam pipes protons are brought to collision with a design centre-of-mass energy of $\sqrt{s}$ =14 TeV. In addition, lead nuclei can also be collided.

Before the protons are injected into the main tunnel, several previous accelerators increase the beam energy step by step. The chain of accelerators, shown in Figure 3.1, begins with the linear accelerator LINAC2. Here, energies of 50 MeV are achieved. Before being injected into the *Proton Synchrotron* (PS), the BOOSTER accelerates the protons to 1.4 GeV. In the next step, the protons are passed into the *Super Proton Synchrotron* with an energy of 2 GeV. The 450 GeV proton beam is split up into two parts. Each of them is injected into one of the beam pipes. Here, 16 radiofrequency cavities further accelerate the protons inside the Lhc main tunnel until the beams reach their final energy. The particles are not accelerated in a continuous beam. In total there are 2808 bunches per beam

with approximately $1.5 \cdot 10^{11}$ protons per bunch. 1232 superconducting dipole magnets deflect the beam. This requires cooling of the magnets with liquid helium down to 1.9 K in order to sustain the 8.33 T magnetic field. Furthermore, 392 quadrupole magnets, also superconducting, keep the beams focused.
Knowing the number of bunches n_b and the particles per bunch N_1 and N_2, the instantaneous luminosity can be calculated via

$$L = \frac{n_b N_1 N_2 f}{4\pi\sigma_x\sigma_y}, \tag{3.1}$$

where f is the revolution frequency and σ_x and σ_y are the horizontal and vertical beam sizes. The design instantaneous luminosity of the LHC is $L = 10^{34}\,\mathrm{cm}^{-2}\mathrm{s}^{-1}$. From the luminosity, the expected event rate of processes with a given cross-section σ can be calculated with

$$\frac{d\mathrm{N}}{d\mathrm{t}} = \sigma \cdot L. \tag{3.2}$$

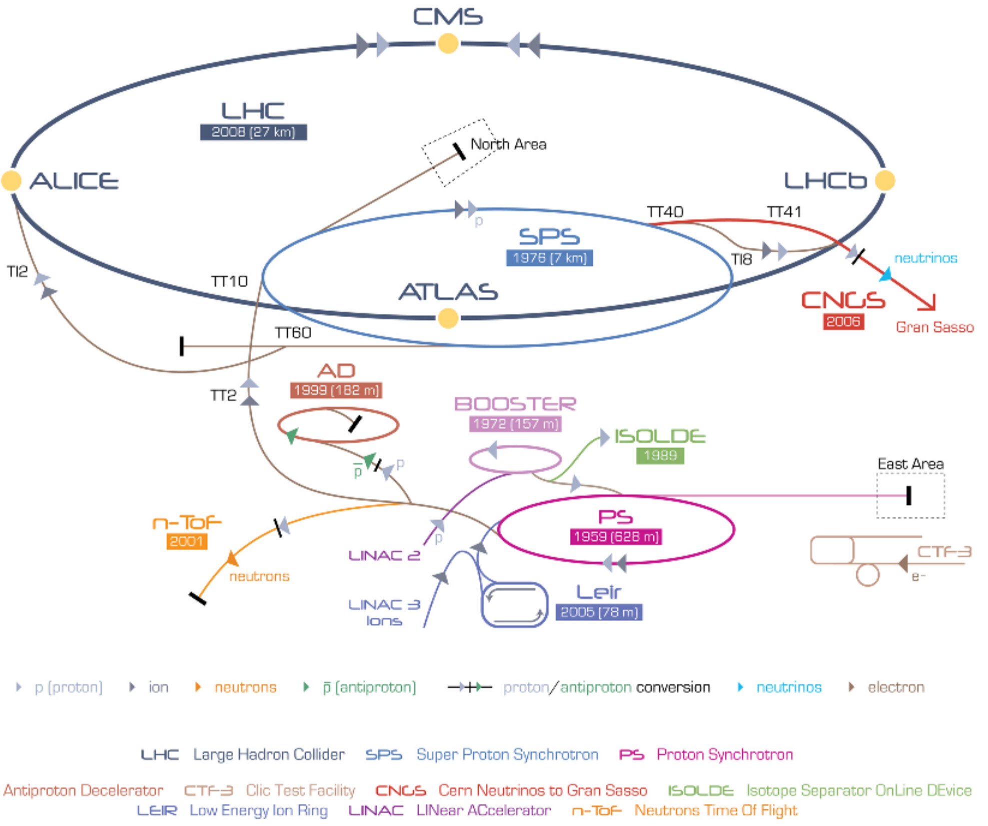

Figure 3.1: The Large Hadron collider and its pre-accelerators. The 50 MeV proton from the linear accelerator in the beginning are injected with 450 GeV into the main tunnel in two oppositely running beams [75].

At each of the four *interaction points*, one of the large experiments is located. By name, these are the two general purpose detectors of the ATLAS (*A Toroidal LHC ApparatuS* [74]) and CMS (*Compact Muon Solenoid* [76]) experiments as well as the more specialised experiments of ALICE (*A Large Ion Collider Experiment* [77]) and LHCb (*Large Hadron Collider beauty experiment* [78]).

The LHC started operating in September 2008. Due to a failure of an electrical connection it was shutdown only a few days later. In November 2009 the beams could be collided again with $\sqrt{s} = 900\,\text{GeV}$.

In March 2010, first collisions of 3.5 TeV beams were established. The 7 TeV run successfully ended in 2010 with $45\,\text{pb}^{-1}$ of data collected. Data taking continued in April 2011 with a slightly upgraded performance and $5\,\text{fb}^{-1}$ total recorded data. Within the 2012 dataset, $\sqrt{s} = 8\,\text{TeV}$ and $15\,\text{fb}^{-1}$ of data, in combination with the 7 TeV data, the Higgs boson was discovered by ATLAS and CMS [4, 5]. In total, $21.3\,\text{fb}^{-1}$ have been collected in the year 2012. From February 2013 until June 2015 the LHC was shut down for a longer time. Upgrades such as the insertion of the new Insertable B-Layer (IBL) for the ATLAS experiment could be performed. Before the winter shutdown in November 2016, $35.6\,\text{fb}^{-1}$ were collected by ATLAS at $\sqrt{s} = 13\,\text{TeV}$, twice as much as in the Higgs discovery dataset. Data taking will continue in 2017 with further improvements.

An overview of the different data taking periods for the ATLAS experiment is given in Figure 3.2(a) as well as an overview of the current period in Figure 3.2(b). Comparing the different periods, it can be seen that due to a better understanding of the collider and upgrades during the shutdowns, the instantaneous luminosity was steadily increased. This results in a steeper rising of total collected data. Due to detector inefficiencies, not all of the delivered data can be recorded and analysed.

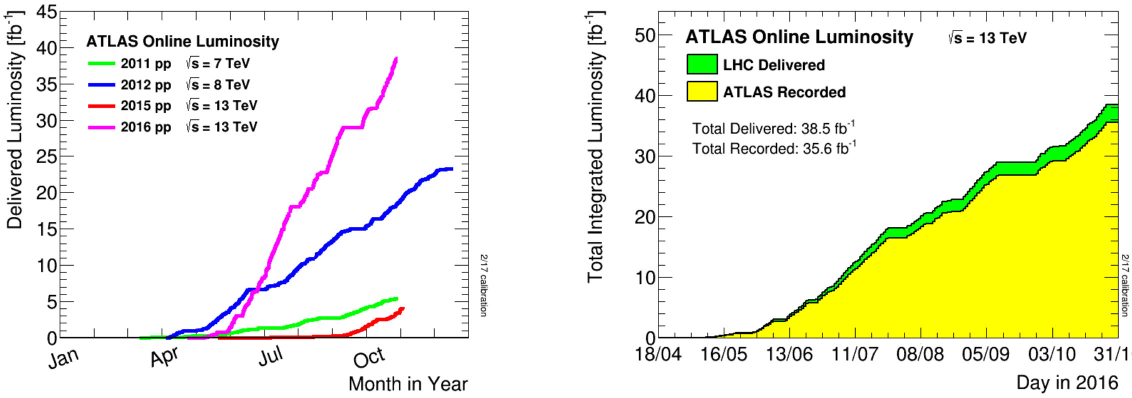

(a) Comparison of data taking periods.

(b) Current period.

Figure 3.2: Figure (a) gives an overview of the integrated luminosity recorded by ATLAS for several data taking periods. Figure (b) shows the current data taking period with delivered and recorded luminosity [79].

3.2 ATLAS Detector

The ATLAS detector [74] is the experimental setup of the ATLAS collaboration [80]. It is the largest detector at the LHC with a length of 44 m and a diameter of 25 m. The whole detector, shown in Figure 3.3, has a weight of about 7000 t. The cylindrical structure around the beam pipe is forward backward symmetric. Except for a region around the beam pipes, the whole 4π range is covered to detect interacting particles and missing energy. Within the ATLAS experiment, the following coordinate system is used:
The origin is located in the middle of the detector. The z-axis points along the beam pipe and the azimuthal angle ϕ gives the position around the beam pipe. For calculations it is useful to define the pseudorapidity as a function of the remaining polar angle Θ between the particle and the beam pipe:

$$\eta = -\ln \tan\left(\frac{\Theta}{2}\right) \overset{E>>m}{\approx} y, \tag{3.3}$$

where y is the kinematic variable called rapidity. It has the property that the particle flux inside a given η-interval is constant and is defined in the following way:

$$y = \frac{1}{2}\ln\frac{E+p_z}{E-p_z}. \tag{3.4}$$

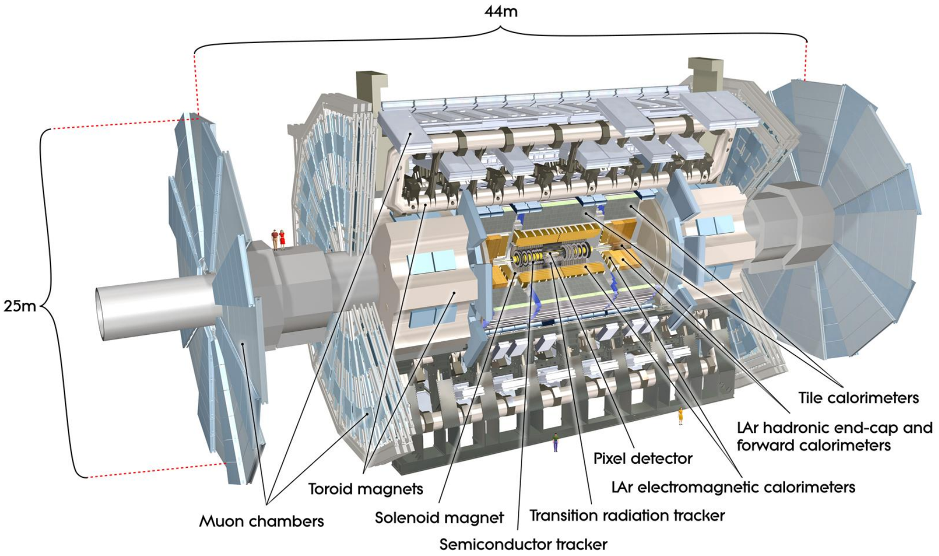

Figure 3.3: An overview of the ATLAS detector. It is made out of several specialised subcomponents for momentum and energy measurements [80].

3.2.1 Trigger System

During Run I, roughly one billion proton-proton collisions needed to be collected per second. To handle the large amount of data, a trigger system [81, 82] was introduced to select interesting events for several analysis. The system reduces the data taking rate for storage from 30 MHz to about 1 kHz.

In a first step, the rate is reduced in a first step to 100 kHz by the hardware based Level-1 Trigger (L1). A decision of L1 is made within 2.5 µs during which data is saved in a pipeline buffer structure. With the remaining events, regions of interest (RoI) are formed, small phase spaces in the $\eta - \phi$ frame.

The high level trigger (HLT) only takes these regions as an input to reduce the event rate down to 1 kHz. This level is software based and uses further information such as resolution and granularity of the sub-components in the region. In opposite to Run I, the HLT is a merged version of the Level-2 trigger and Event Filter computer clusters. The merging reduces the complexity and allows for dynamic resource sharing between algorithms.

3.2.2 Detector Components

The ATLAS detector is composed of several subsystems. Each of them was designed to measure specific properties. Combining the measurements of the components, events can be reconstructed. Closest to the beam pipe is the inner detector. It is surrounded by a solenoid magnet that creates a 2 T strong magnetic field. The bending of charged particles in the field makes it possible to measure the transverse momentum. A toroidal magnet covers the rest of the detector with a peak field of 4 T. This makes it possible to have two independent measurements of muon momenta. In the calorimeters, particles deposit their energy which can then be measured.

Inner Detector The inner detector [83], shown in Figure 3.4, is 6.2 m long and has a diameter of 2.1 m. Three subsystems cover the whole $|\eta| < 2.5$ range. In order to measure the tracks of up to several thousand events per bunch crossing, a high granularity in the inner detector is needed. This ensures a good momentum and vertex resolution for each event.

The pixel detector consists of three barrel shaped layers around the beam pipe with three additional disks on each end. It is located closest to the beampipe. Therefore, radiation hardness is another important property to be considered. During the first long shutdown, the IBL was inserted between the inner pixel layer and the beam pipe as a fourth pixel layer. This was necessary to compensate for radiation damage and to sustain the radiation hardness in the current and future runs. It further increases the b-tagging and overall resolution due to a smaller pixel size of $50 \times 250\,\mu\text{m}^2$. It consists of 14 staves that are loaded with newly developed modules.

The other 3 layers consist of 1744 sensor-chip-hybrid modules. Each of the modules contains a $250\,\mu\text{m}$ thick n^+-in-n sensor with 47232 pixels and a size of $50 \times 400\,\mu\text{m}^2$ each. The pixels are connected to 16 FE chips via the bump bond technique.

The Semiconductor Tracker (SCT) is the second tracking detector installed in the inner detector. Four barrel layers and a total of eighteen endcaps use single sided p-in-n microstrips instead of pixels. The strips are rotated by 40 mrad with respect to each other to avoid ghost hits[1]. Using microstrips results in a worse resolution than in the pixel detector with $16\,\mu\text{m}$ in the R-ϕ frame and $580\,\mu\text{m}$ in the z-direction ($12/90\,\mu\text{m}$ for the pixel detector, respectively).

The transition radiation tracker (TRT) is the outermost part of the inner detector. It is made out of roughly 300,000 straw tubes filled with Xenon. On average, a particle with $|\eta| < 2.1$ passes 36 tubes. The tubes are embedded in a passive material. The spatial resolution is about $130\,\mu\text{m}$. Besides using the transition radiation for tracking, the TRT is used for electron identification. Compared to other particles, the transition radiation between the passive material and the tubes is significantly larger for electrons due to their small mass allowing for an identification of electrons.

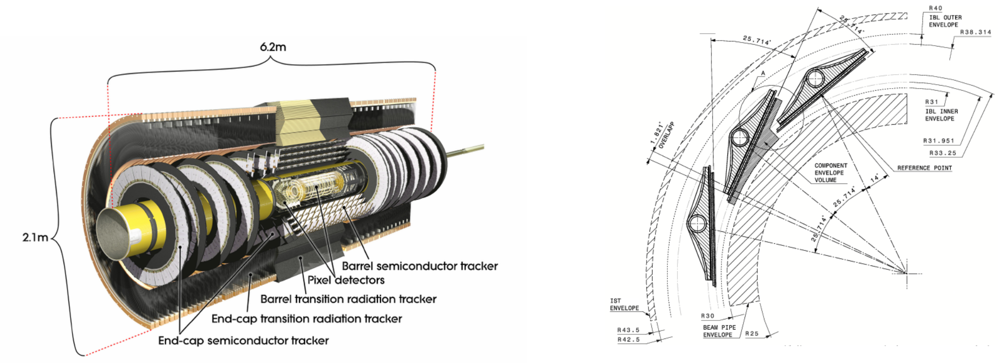

(a) Atlas Pixel detector.

(b) Insertable B-Layer (IBL).

Figure 3.4: An overview of the Atlas pixel detector without the Insertable B-Layer (a) as well as a schematic of IBL (b) which is placed directly next to the beam pipe [80, 84].

---

[1] When two hits occur at the same time in different positions in a grid structure there are two possible true combinations. Shifting the strips moves one of the possibilities out of the detector region.

Calorimeter System The calorimeter system [85], schematically shown in Figure 3.5, consists in total of two calorimeters. The *electromagnetic* calorimeter (ECal) is surrounded by the *hadronic* one (HCal). Both calorimeters are so called *sampling* calorimeters. This means that a passive absorber and an active material alternate within the calorimeter. The passive material needs to provide a high interaction probability of bypassing particles, whereas the active material needs to be efficient in measuring the total deposited energy. In the electromagnetic case, a barrel region and two end-caps cover the range of $|\eta| < 3.2$. Lead was chosen as passive and liquid Argon as active material. The thickness of the materials was chosen to be 24 (26) *radiation lengths*, the length after which the number of particles decreased to 1/e.

If a high energetic photon enters the calorimeter, an $e^+ - e^-$ pair is produced. Now, further photons can be radiated and the process continues. The same holds for a high energetic electron/positron. Bremsstrahlung and pair-production are the dominant processes and hence, other particles can pass through the ECal with only small energy losses.

The HCal is divided into three parts. The thickness was chosen to be eleven *interaction lengths*. This is sufficient to avoid punch-through into the muon chambers. The central part ($|\eta| < 1.7$) is made out of steel absorbers and plastic scintillators. In the forward region, the Hadronic End-cap Calorimeter (HECP) uses copper absorbers and, as the electromagnetic calorimeter, liquid Argon to measure hadronic events in the pseudorapidity range $1.5 < |\eta| < 3.2$. Finally, the Forward Calorimeter (FCal) measures signals in the $3.1 < |\eta| < 4.9$ range. It also uses liquid Argon but in combination with a dense tungsten matrix.

In all three parts, strong interactions with the nuclei of the absorber material result in the deposition of energy. Typically, the interaction length is larger than for electromagnetic components. Mainly due to pions produced in the shower, which then further decay into two photons, every hadronic shower has an electromagnetic fraction.

The resolution of a calorimeter is given by

$$\frac{\sigma_E}{E} = \underbrace{\frac{\mathrm{a}}{\sqrt{E}}}_{\text{stochastic}} + \underbrace{\frac{\mathrm{b}}{E}}_{\text{noise}} + \underbrace{\mathrm{c}}_{\text{systematic}} \overset{\text{ATLAS}}{\approx} \begin{cases} \frac{50\,\%}{\sqrt{E}} & \text{hadronic calorimeter} \\ \frac{10\,\%}{\sqrt{E}} & \text{electromagnetic calorimeter} \end{cases} . \tag{3.5}$$

Typically, the stochastic term is dominant for high energetic particles so that a $\frac{1}{\sqrt{E}}$ behaviour of the resolution can be assumed.

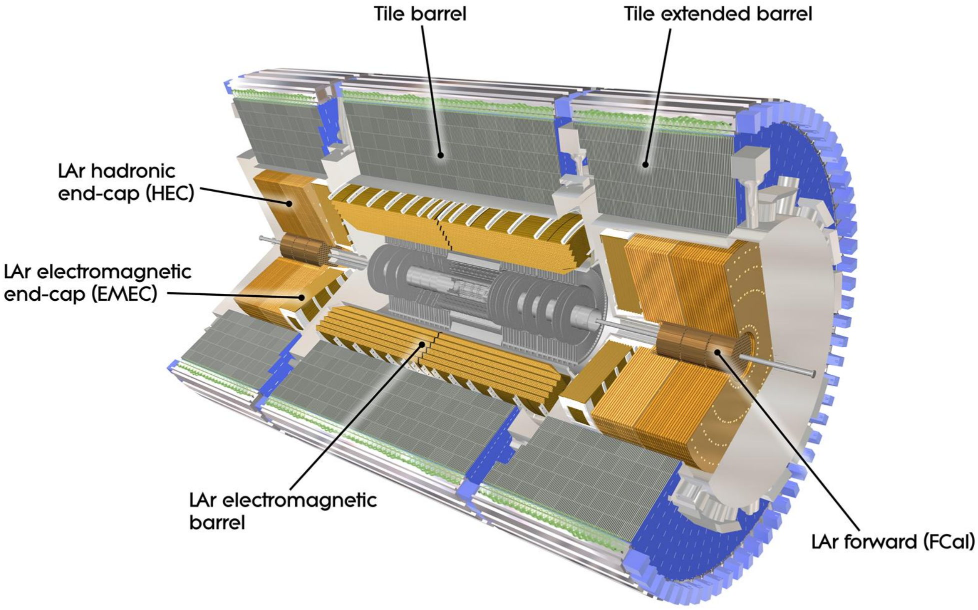

Figure 3.5: An overview of the ATLAS calorimeter system. It is split into two parts, the electromagnetic and the hadronic calorimeter. Both parts have a barrel-like structure with end caps [86].

Muon System The muon system [87] is the outermost layer of the ATLAS detector. The probability to radiate Bremsstrahlung, the dominant process in the electromagnetic calorimeter for electrons, for a particle with mass M is proportional to $\frac{1}{M^2}$. For muons this means that they only radiate roughly $\frac{1}{40000}$ times the energy of an electron in the electromagnetic calorimeter via Bremsstrahlung and ionisation becomes dominant. Accordingly, they pass the calorimeters without a significant energy loss and can be measured separately. To compensate for the missing energy measurement of the muons in the calorimeter, additional muon chambers are used. They are designed to measure the transverse momentum p_T in addition to and independent from the inner detector.

Monitored drift tubes (MDTs) cover a range of $|\eta| < 2.0$ and consist of three layers. For larger pseudorapidity regions ($2.0 \leq |\eta| < 2.7$) Cathode Strip Chambers (CSCs) are used for the detection of muon signals. They consist of Multiwire Proportional Chambers (MWPC) combined with a cathode strip readout.

To trigger muon events, Resistive Plate Chambers (RPCs) are used in the barrel region and thin gap chambers (TGCs) in the end-caps. Both provide a well defined $\mathrm{p_T}$-threshold and an additional orthogonal measurement.

4 Top-Quark Reconstruction

The reconstruction of top-quarks is done by analysing their decay products. One possibility is to assign the measured jets to quarks that directly originated from the top-quark decay, the so called *parton-level*. The comparison with the parton-level can be helpful in analyses since additional information is gained from the assignment. As an example, a likelihood cut can filter part of the events where decay products are faked by additional jets from initial or final state radiation.

In this chapter, an overview of the Kinematic Likelihood Fitter KLFitter, a common analysis tool, is given. Furthermore, shortcomings in its performance are presented. They are a consequence of acceptance cuts that are of interest in general for particle physics. In the second part, the development of new transfer functions for KLFitter is presented. The TFTool, an important tool for studies related to transfer functions, is also presented. After presenting the main physical aspects to be considered, an overview of possible implementations in TFTool is given.

4.1 Kinematic Likelihood Fitter

In order to map measured quantities to the parton-level, the Kinematic Likelihood Fitter package (KLFitter) was developed [1]. It is based on the Bayesian Analysis Toolkit (BAT) [88] and is nowadays a well-established tool in the top-quark community for semileptonic events.

KLFitter uses predefined properties, such as the masses of the W-boson and the top-quark, to define a likelihood for each permutation of jets. If, for example, four jets and a lepton are reconstructed, there are 24 possible permutations for the assignment of the jets to parton-level. The number of permutations can be reduced if b-tagging is applied, since two quarks are then associated with the b-quarks, or increased if more than four jets are considered. KLFitter calculates the likelihood

$$\begin{aligned}\mathcal{L} =&B\{m(q_1q_2)|m_W,\Gamma_W\}\cdot B\{m(l\nu)|m_W,\Gamma_W\}\cdot\\ &B\{m(q_1q_2b_{had})|m_t,\Gamma_t\}\cdot B\{m(l\nu b_{lep})|m_t,\Gamma_t\}\cdot\\ &W\left(\tilde{E}_{jet_1}|E_{b_{had}}\right)\cdot W\left(\tilde{E}_{jet_2}|E_{b_{lep}}\right)\cdot W\left(\tilde{E}_{jet_3}|E_{q_1}\right)\cdot W\left(\tilde{E}_{jet_4}|E_{q_2}\right)\cdot\\ &W\left(\tilde{E}_X^{miss}|p_{x,\nu}\right)\cdot W\left(\tilde{E}_y^{miss}|E_{p_{y,\nu}}\right)\cdot\begin{cases}W\left(\tilde{E}_l|E_l\right), & e+\text{jets channel}\\ W\left(\tilde{p}_{T,l}|p_{T,l}\right), & \mu+\text{jets channel}\end{cases}\end{aligned} \tag{4.1}$$

for each of the permutations and chooses the most probable one. Hereby, B represents the Breit-Wigner distributions for the top-quark with a fixed mass of $m_t = 172.5\,\text{GeV}$ and the W-boson with $m_W = 80.4\,\text{GeV}$. The functions are evaluated for the invariant masses and the energies of the quarks and leptons considered in each function. The Breit-Wigner- and the transfer functions W are normalized to unity.

The role of the transfer functions, further discussed in section 4.3, is crucial in the KLFitter package. Transfer functions describe the resolution of the measured quantities $\mathrm{E_{Meas}}$ and $\mathrm{p_{T,Meas}} = \sqrt{p^2_{\mathrm{x,Meas}} + p^2_{\mathrm{y,Meas}}}$ and allow for variations within the detector resolution in order to better match the mass requirement considered in the Breit-Wigner distributions. This means that a larger contribution of the Breit-Wigner term can be achieved by allowing small fluctuations of the measured values. As an example, a small fluctuation of the jet-energy assigned to the b quark from the hadronic decaying top quark $\tilde{E}_{jet_1}$ can lead to a better agreement of the invariant mass of the three quark system $q_1q_2b_{had}$ with the hadronic W-boson mass. The invariant mass is considered in the expression $B\{m(q_1q_2)|m_W,\Gamma_W\}$. On the other hand, larger fluctuations are less likely. Therefore, a combination of the Breit-Wigner terms and the transfer functions provides a reasonable motivated likelihood for the best permutation.

4.2 Performance Studies

Figure 4.1 shows the efficiency of KLFitter for several criteria. The second bin, labelled as *lJets*, gives the fraction of semileptonic events and is taken as a reference in the following studies. The other bins give the cases that (from left to right) a τ-lepton was found, all partons fulfill the present criterion, all jets are within the first four selected jets, the W-boson has the correct jets assigned, all partons are matched, at least one jet/parton matches two or more partons/jets, all light jets have been found and are unique in addition to being in the first four selected jets, the hadronically/leptonically decaying top quark or both of them have the correct partons assigned or that the reconstructed missing energy matched the neutrino from the leptonically decaying W-boson. To study the performance of KLFitter a matching criterion is required. It allows to evaluate if an assignment between parton and jet is correct. The matching criterion is defined by

$$\Delta R_{\text{parton,jet}} = \sqrt{(\Delta_{\text{parton, jet}}\eta)^2 + (\Delta_{\text{parton,jet}}\phi)^2} < 0.3\,. \tag{4.2}$$

If a jet is assigned correctly to the corresponding parton, the jet-parton pair is label as *matched*. If the jet that corresponds to a parton is within the selected objects of the event but is assigned to another parton it is labelled as *present*. Another important bin in Figure 4.1 is labelled as *All jets present*. In this case, all partons (two b-quarks, and the hadronic W decay products) have a biunique[1] present jet.

In approximately 50 % of all events at least one parton does not fulfil the present criterion. Since always four jets are required in the likelihood function, another jet, originating from initial or final state radiation, is used instead.

In this section, some studies are presented to understand the origin of mismatched events. Within KLFitter, this can be used to improve its performance. The $\sqrt{s}$ =13 TeV MC sample[2] was generated with Powheg in combination with Pythia8. It has a total of approximately 1510000 events of which about 1300000 are semileptonic (86 %). In total, there are around 770000 events in which at least one jet is not labelled as present. This corresponds to 51 % of all events and 58 % of semileptonic events. The selection criteria are exactly one electron or muon with $p_T > 25$ GeV and at least four jets with $p_T > 25$ GeV.

---

[1] For each jet there is only one parton and for each parton there is only one jet that fulfills the matching criterion.

[2] The used sample is:
mc15_13TeV.410006.PowhegPythia8 EvtGen_A14_ttbar_hdamp172p5_nonallhad.merge.
DAOD_TOPQ1.e3836_a766_a810_r6282_p2501

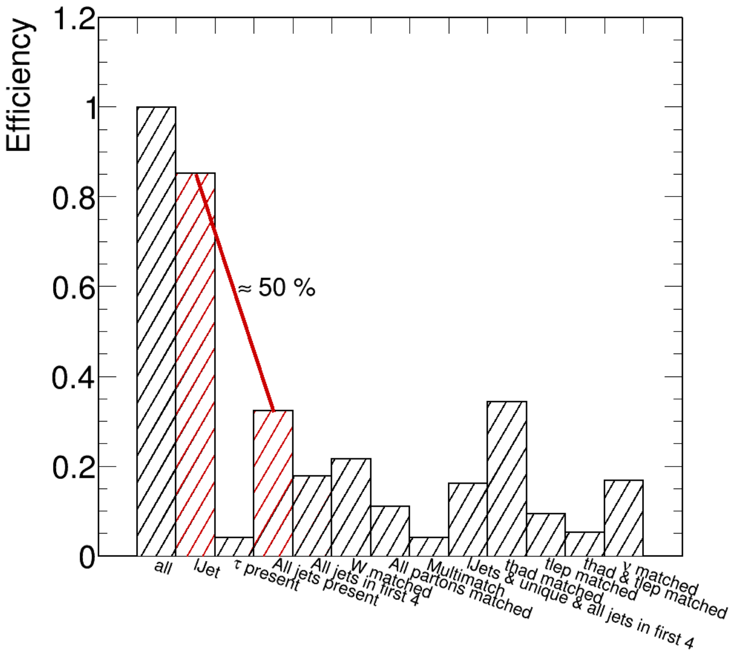

Figure 4.1: Efficiency of the KLFitter matching. The bins on the x-axis show several possible matching criteria. The second bin shows the percentage of semileptonic events in the sample and should be seen as a reference. The fourth bin shows the cases in which all partons have any jet from the event assigned. The difference between the second and fourth bin is approximately 50 % of the total events.

Likelihood Distribution The likelihood distributions of KLFitter can be seen in Figure 4.2. The two shown examples compare matched and unmatched events 4.2(a) as well as present and not present events 4.2(b). It is observed that in the matched/present case, the likelihood drops off faster for lower values of $\log L$. Therefore, a larger peak is observed. The effect is stronger in the matched case. In addition, the likelihood for wrongly assigned events does not drop off at a certain value. It also peaks for higher $\log L$ values as can be seen in the not present/matched cases. This means that, just by looking at the likelihood, wrongly assigned events cannot be distinguished from correctly assigned ones.

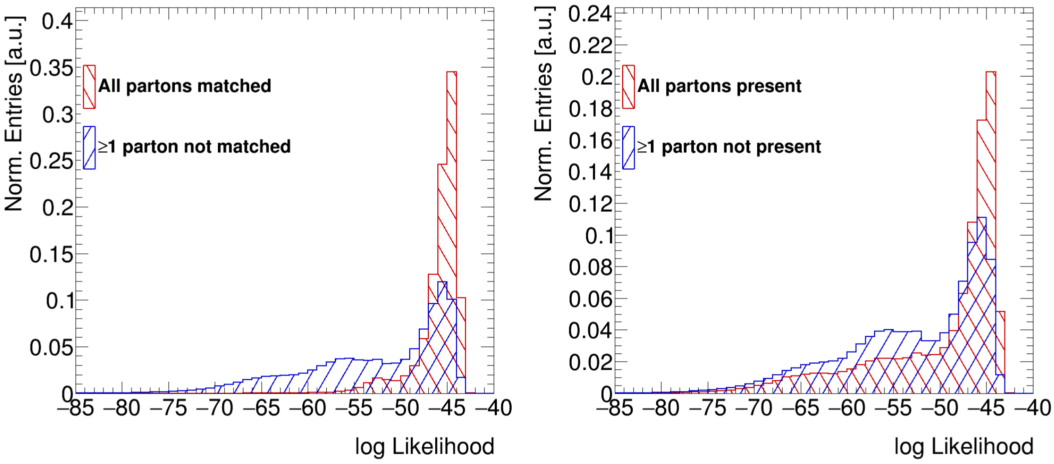

(a) Matched events (b) Present events

Figure 4.2: The KLFitter likelihood distribution compared for (not) matched (a) and (not) present (b) events.

However, by applying a cut on the likelihood, the percentage of entries that are not labelled as present can be reduced as shown in Figure 4.3. For a likelihood cut of $\log L_{\text{event}} = -48$, the percentage of not all-jets-present events could be decreased to approximately 43 % from previously 54 % of semileptonic events. It should however be considered that the total number of remaining events decreases and hence sufficient statistics are required.

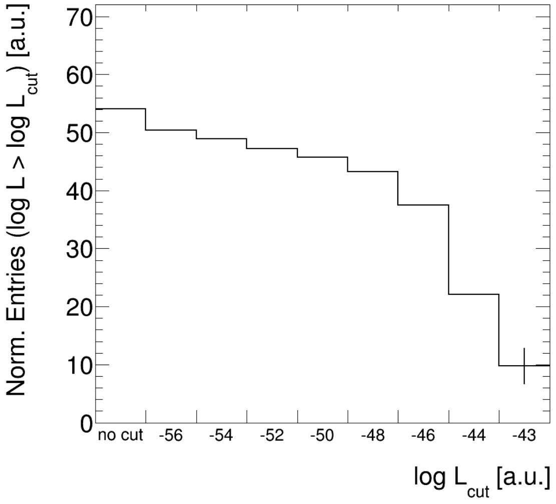

Figure 4.3: The percentage of not all-jets-present events as a function of different likelihood cuts. In some cases the error is below the line width.

Jet Merging When two partons are produced very close to each other the energy depositions in the calorimeter can overlap. The reconstructed jets are then merged and cannot be detected separately. This is one possible reason why one of the corresponding jets cannot be matched to a parton, the jet is included in one big jet that consists of (at least) two individual jets that cannot be easily distinguished anymore. The presented studies are independent of the KLFITTER framework but can be used for the efficiency studies.

The requirement for top-quark pair production is $\hat{s} \geq x_l x_k s$ as shown in section 2.2.1. This means that the top-quarks are produced with more energy than needed for their rest mass. This can lead to significant p_T-values of the quark. The resulting *boost* is passed on to the top decay products which can lead to *jet merging*, sketched in Figure 4.4. The two jets of the W-boson decay cannot be distinguished anymore in this case and appear as one large jet.

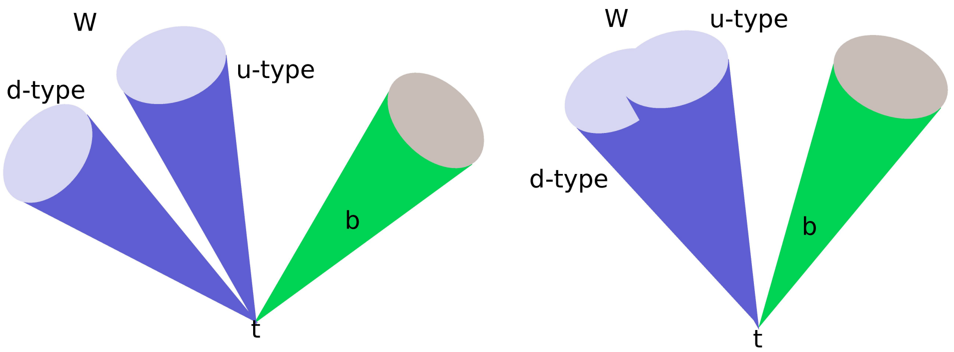

(a) low p_T top-quark (b) high p_T top-quark

Figure 4.4: Overview of jet merging. In the unboosted case (a), the jets can be detected separately, whereas in the boosted case (b), the W-boson decay products appear as one big jet.

In the beginning it was found that reconstructed objects cannot get closer than $\Delta R = 0.4$. This is in agreement with the radius used in the anti-kT jet algorithm within ATLAS [89].

To study the effect of jet merging, the distance of the W-boson decay products on truth level as a function of the top-quark p_T is shown in Figure 4.5. It can be seen that the average distance decreases for a higher top-quark p_T. In Figure 4.6(a) the number of partons with a distance smaller than 0.4 is divided by the number of entries in the given p_T bin. The increase for higher p_T of the t or $\bar{t}$ supports the hypothesis of jet merging for boosted events. However, even though the effect increases for higher energies, the percentage of entries within a small radius is only in the order of $< 1\,\%$. This small value did not change significantly by smearing the ϕ and $|\eta|$ distributions with a Gaussian to simulate small fluctuations around the true values.

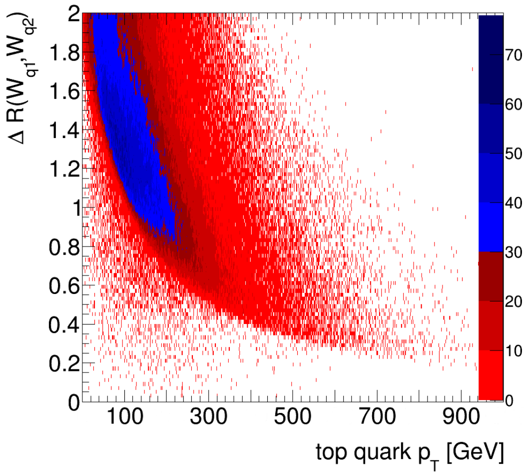

Figure 4.5: Distance between the parton-level W-boson decay products as a function of the top-quark $\mathrm{p_T}$.

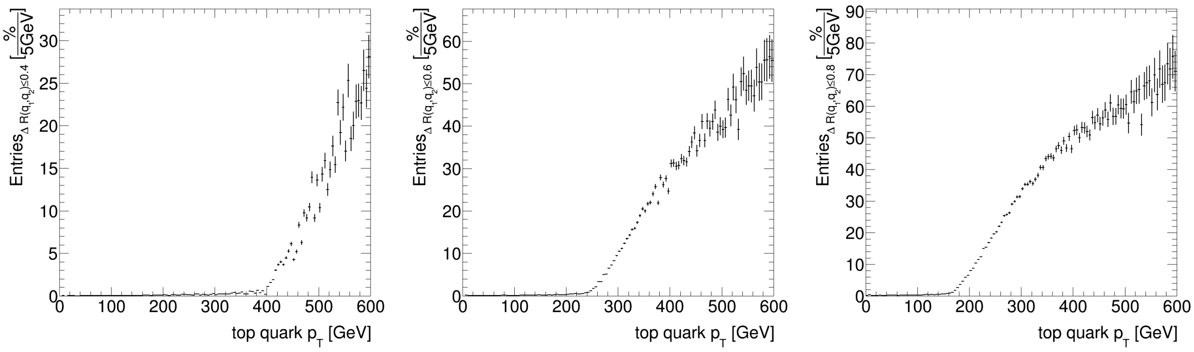

(a) $\Delta R < 0.4$ (b) $\Delta R < 0.6$ (c) $\Delta R < 0.8$

Figure 4.6: Percentage of entries in each bin with a radius smaller than the examined value. A steep increase for higher top-quark p_T can be seen in shifts to larger values for a smaller chosen radius.

Simulating a jet by assuming a radius of 0.4 around the parton-level quark also assumes that possible jets completely merge. To study the effect of partial jet merging, the radius of 0.8 , where the cones around the partons only partially overlap, as well as a medium radius of 0.6 are checked. Figure 4.6 summarises the results. For $\Delta R < 0.4$, 0.22 % of all events are within the cone, 1.64 % for $\Delta R < 0.6$ and 5.46 % $\Delta R < 0.8$. It can be concluded that jet merging is important for boosted events and therefore becomes more and more important for future colliders. However, it does not explain the inefficiency of approximately 50 % observed in KLFitter.

Acceptance Cuts The main reason why some events are not labelled as all-jets-present are the acceptance cuts used in KLFitter. In the reconstruction of truth events from the MC generator, a $p_T > 25\,\text{GeV}$ and $|\eta| < 2.5$ cut is applied. The p_T-cut is needed for background suppression, while the $|\eta|$ cut selects the region covered by the inner detector. Unfortunately, losing signal events by applying these cuts cannot be avoided. The influence of these cuts on KLFitter is presented in this section.

Table 4.1 shows the percentage of truth entries for different parton selections in the case that an event is not labelled as all-jets-present. The last row seen in table is that in 92.3 % of the cases an event with not all partons tagged as present has at least one parton outside of one of the accepted regions on truth level. With respect to the number of entries, this corresponds to 46.8 % of all entries and to 54.1 % of semileptonic events which is in good agreement with the value observed in the KLFitter efficiency shown in Figure 4.1. Furthermore, it can be confirmed that no events are out of the acceptance region on truth level in the case that all jets are present. Figure 4.7(a) and 4.7(b) show the behaviour of the not-all-jets-present events in dependence of additionally applied $\mathrm{p_T}$ and $|\eta|$ cuts. The y-axis represents the ratio of events in the semileptonic case for which either

$$\begin{gathered} p_T < p_{T,\mathrm{cut}} \text{ or } |\eta| > 2.5 \\ \text{or} \\ |\eta| < \eta_{\mathrm{cut}} \text{ or } p_T < 25\,\mathrm{GeV} \end{gathered} \tag{4.3}$$

is true for any parton. Loosening the cuts would decrease the inefficiency. However, changing the cut-values in an analysis needs to respect more than just the performance of the fitter. Often, the main goal is to optimise the event selection with respect to e.g. systematic uncertainties and signal to background rejection.

Table 4.1: Percentages of entries on parton-level out of the acceptance region when not all jets are present.

Parton(s) selected	$p_T < 25$ GeV [%]	$\|\eta\|$ >2.5 [%]	($p_T < 25$ GeV or $\|\eta\| > 2.5$) [%]
u-type	15.8	26.0	29.4
d-type	24.0	35.4	39.6
hadronic b	8.3	20.2	22.8
leptonic b	8.6	23.0	23.0
u/d-type or **bhad** or **blep**	**52.9**	**83.9**	**92.3**

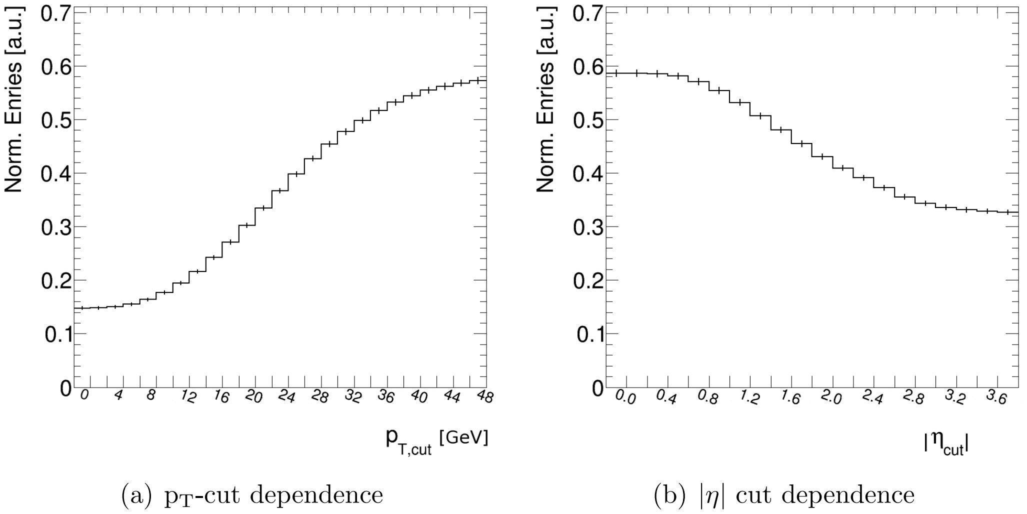

(a) $\mathrm{p_T}$-cut dependence

(b) $|\eta|$ cut dependence

Figure 4.7: Percentage of semileptonic events not in the accepted region for different $\mathrm{p_T}$ (a) and $|\eta|$ (b) cut-values.

4.3 Transfer Functions

In Section 4.1, it was already mentioned that transfer functions are used to describe the detector resolution in the calculation of a likelihood for each permutation. This section deals with the development of new transfer functions and is organised as follows:
After motivating the need for new functions, based on functions that were used during the $\sqrt{s} = 7$ and 8 TeV runs, TFTool, a tool used for the derivation of transfer functions, is introduced. Afterwards, the main contributions to the observed Δ E spectra are presented. Besides the statistical behaviour of an energy measurement, the geometrical dependence between $\mathrm{p_T}$-cut and $|\eta|$ result in an implicit energy cut. Furthermore, neutrinos are produced in additional leptonic decays within a jet and carry away part of the jet energy. This chapter concludes with an overview of the steps needed for a good implementation of the physical aspects within TFTool. The studies presented focus on the transfer functions for light and b-jets. Hence, Section 4.3.7 only gives a short overview of possible effects to be considered for electrons and muons.

4.3.1 Transfer Functions at $\sqrt{s} = 7$ and 8 TeV

For $\sqrt{s} = 7$ and 8 TeV, a double Gaussian function was used to describe the $\Delta E = \frac{\mathrm{E_{Truth}} - \mathrm{E_{Meas}}}{\mathrm{E_{Truth}}}$ spectrum, the relative difference between the parton-level energy $\mathrm{E_{Truth}}$ and the measured energy $\mathrm{E_{Meas}}$. The double Gaussian models the spectrum without providing an explanation of its shape which is part of this thesis. It is defined in the following form:

$$W(E_{\mathrm{Meas}}, E_{\mathrm{Truth}}) = \frac{1}{\sqrt{2\pi}(p_2 + p_3 p_5)} \left(e^{\frac{(\Delta E - p_1)^2}{2p_2^2}} + p_3\, e^{\frac{(\Delta E - p_4)^2}{2p_5^2}} \right). \tag{4.4}$$

The two Gaussians are referred to as big and small Gaussian. The big one is motivated by the energy resolution of the detector, which is assumed, in good approximation, to be Gaussian for a fixed value of $\mathrm{E_{Truth}}$ as discussed in section 4.3.3. The small one was introduced to describe higher order effects in the spectrum, e.g. additional tails that occur in some cases. Even though the description proved to work, it has some shortcomings that make it necessary to study the underlying effects in detail. In the Δ E spectrum a shift of the mean value together with an upper bound of Δ E is observed for low values of $\mathrm{E_{Truth}}$ as shown in Figure 4.8(a) for light jets. Since this leads to a significantly different behaviour of the transfer functions in this region the dependence of the parameters, that are used in the double Gaussian, on $\mathrm{E_{Truth}}$ was only fitted down to $\mathrm{E_{Truth}} = 100$ GeV. The region below was then extrapolated from the fit in order to also provide a description for lower energy regions. Furthermore, the parametrisation functions should be based on physical properties.

By considering a typical energy spectrum for light jets, as shown in Figure 4.9, it can be seen that especially for the first two $|\eta|$ regions ($0.0 < |\eta| \leq 0.8$, $0.8 < |\eta| \leq 1.37$), most of the events are produced with $\mathrm{E_{Truth}}$ values below the cut. This means that the parametrisation was applied to many events based on few. Explaining the shift of the mean value and the corresponding upper bound of Δ E in the spectra is therefore necessary to provide a better description of the $\mathrm{E_{Truth}}$ dependence at low energies for the parameters of the fit function.

In addition, as soon as this effect is not observed anymore at higher values of $\mathrm{E_{Truth}}$,

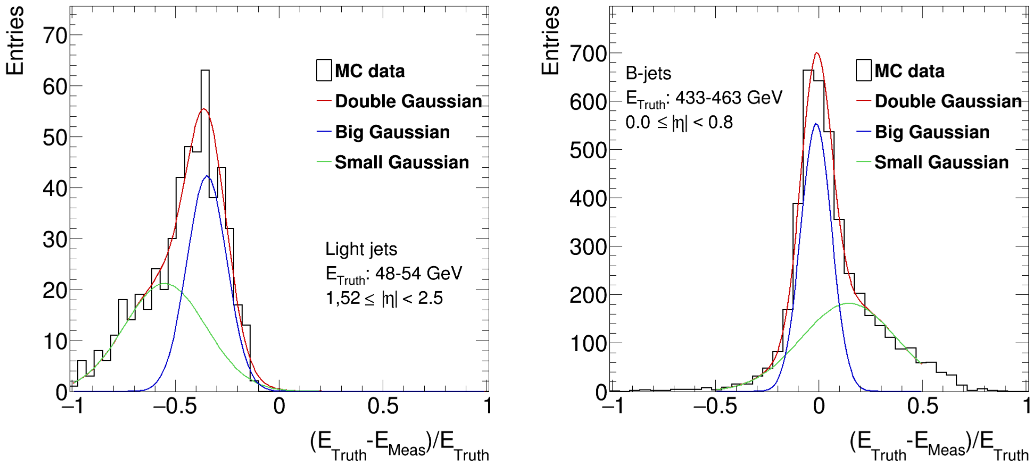

(a) Light jets local fit with edge.

(b) B-jets local fit.

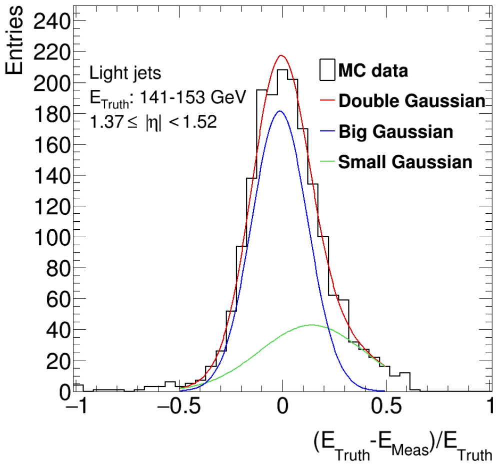

(c) Light jets local fit.

Figure 4.8: Example outputs of the local fits of the old transfer function. Figure (a) shows the upper bound observed in lower $\mathrm{E_{Truth}}$ bins, whereas in Figure (b), the case with a significant tail is shown. Figure (c) shows a rather symmetric example. The spectra are modelled by a double Gaussian function.

the $\Delta\,\mathrm{E}$ spectrum shows a significant tail for $\Delta\,\mathrm{E} > 0$ at higher $\mathrm{E}_{\mathrm{Truth}}$ bins as shown in Figure 4.8(b). How strongly the shift and the right tails are pronounced depends on the $|\eta|$ region as well as the particle type. This makes it necessary to study each particle type in detail.

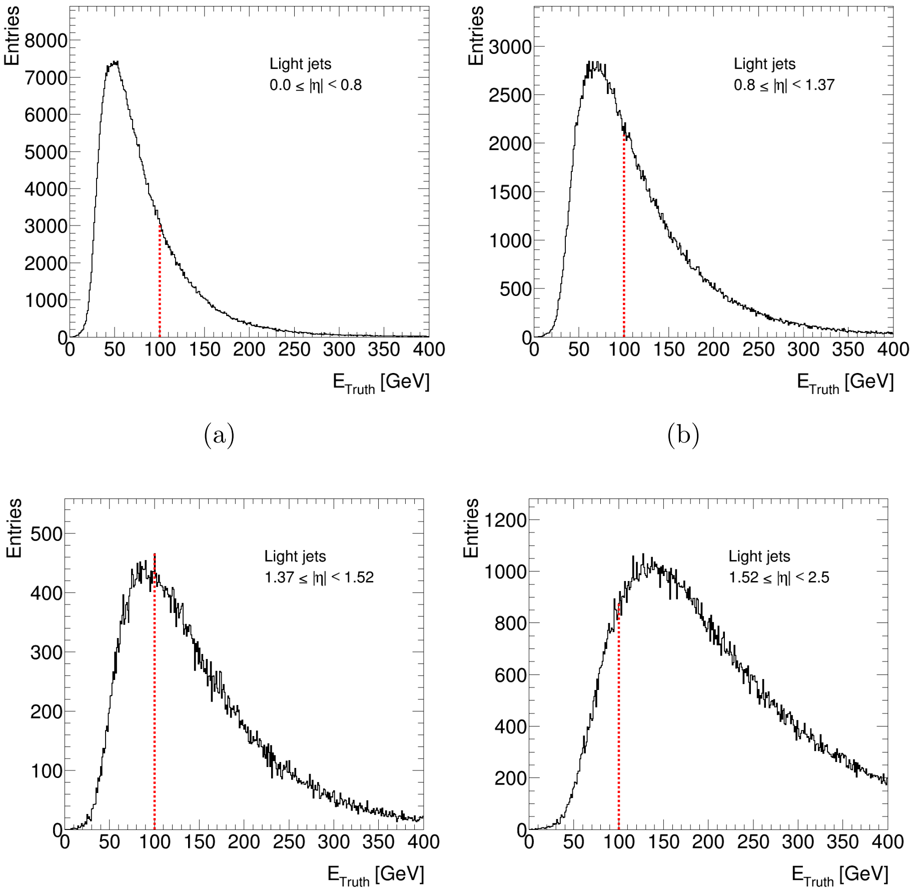

(a) (b)

(c) (d)

Figure 4.9: Parton-level energy spectra of the four default $|\eta|$ regions. The red lines marks 100 GeV that is used as cut-value for the development of transfer functions.

4.3.2 Transfer Function Tool

The challenge for the development of new transfer functions is to provide a parametrisation of the parameters p_i as a function of $\mathrm{E}_{\mathrm{Truth}}$ that describes each $\Delta\,\mathrm{E}$ spectrum. The parameters that are used depend on the function that is evaluated (e.g. six for a double Gaussian function). To allow for this evaluation, the *Transfer Function Tool* TFTool was developed.

The tool uses Mc@nlo generated $t\bar{t}$ events in the lepton + jets channel, similar to the

KLFitter studies. For the development of transfer functions, only biuniquely matched objects are considered.

The events are separated in four $|\eta|$ regions mainly based on detector properties such as the transition between the barrel and the end-cap region. For light jets, b-jets and electrons, the default borders of the $|\eta|$ regions are $0.0\,,\ 0.8\,,\ 1.37\,,\ 1.52$ and $2.5\,$. For muons they are $0.0\,,\ 1.11\,,\ 1.25\,,\ 2.5\,,\ 3.0$ due to different detector properties, such as the transition from barrel to end-cap region, to be considered. Since it is expected that the parameters do not only depend on $|\eta|$ but also on the kinematics, the events are also binned in $\mathrm{p_T}$ for muons or $\mathrm{E_{Truth}}$ in all other cases.

The exact energy region of each histogram that is created depends on the configuration set by the user. Typically, a minimum of 250 events per $\Delta\,\mathrm{E}$ histogram is required with a maximum energy width of 30 GeV. The histograms are then created automatically within TFTool from the measured and the parton-level energy. If not enough entries are available, the energy bins of each histogram are adjusted and the histograms are formed again. If either the energy bin width becomes too large or a user defined maximum value of $\mathrm{E_{Truth}}$ is reached, the histogram binning stops and the histograms from the last iteration are taken as an output. Examples for light jets and b-jets are shown in Figure 4.8.

After the binning, for each histogram in each pseudorapidity region, a *local* fit of the $\Delta\,\mathrm{E}$ spectrum is performed. Here, the transfer function under evaluation is fitted with starting parameters and parameter limits set by the user. After this first fit, for each histogram a set of parameters p_i exists.

In the *parameter estimation* these parameters are fitted as a function of $\mathrm{E_{Truth}}$. In detail this means that in each $|\eta|$ region the parameters p_i are extracted from each histogram and then fitted. The function used for the parameter estimation have to be physically motivated, e.g. $f(\mathrm{E}) = \frac{a}{\sqrt{\mathrm{E}}} + b$ for the resolution parameter of the bigger Gaussian in the case of b-jets, light jets or electrons and a fit with double Gaussian function. Two examples of the parameter estimation for p_1 and p_2 are given in Figure 4.10 for a double Gaussian function (see section 4.3.1).

Typically it is necessary to repeat the *local* fit and the *parameter estimation* several times while changing the parameter limits until a good result is achieved.

In the final step, the parametrisation is taken to *globally* fit the transfer functions to all histograms simultaneously within an $|\eta|$ region. The results for the parameters are then taken as transfer function for KLFitter.

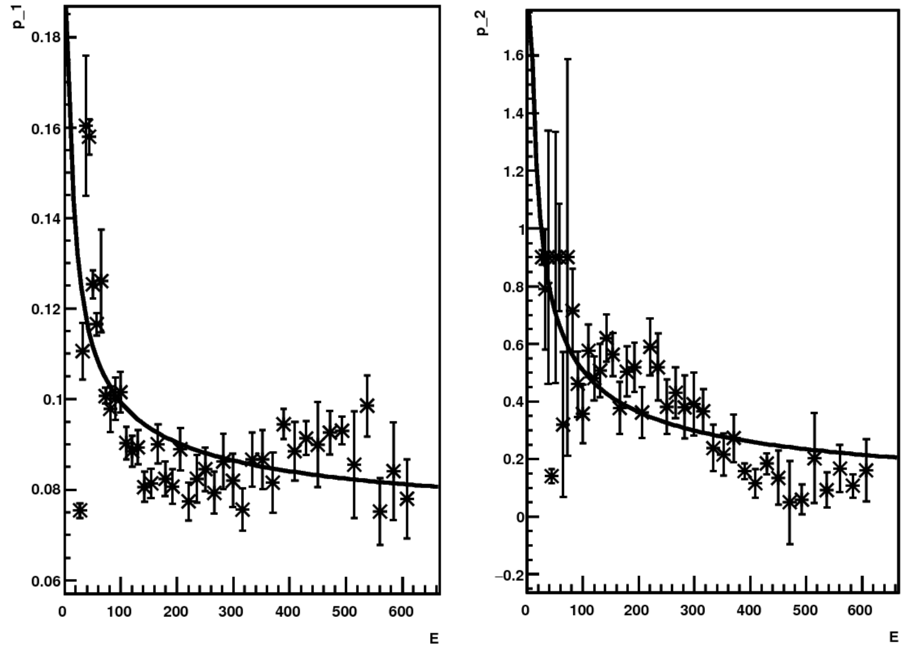

(a) p_1 estimation (b) p_2 estimation

Figure 4.10: Two examples for the output of the parameter estimation for p_1 (offset of the bigger Gaussian) (a) and p_2 (width of the bigger Gaussian) (b) for $0.0 < |\eta| \leq 0.8$ and a double Gaussian fit function.

4.3.3 Energy Resolution

If a monoenergetic beam is measured by a detector, the resulting spectrum will have a Gaussian shape centred around the original beam energy. This is a direct consequence of the statistical behaviour of the energy deposition within the calorimeter. In Equation 3.5, this is represented by the stochastical term. Therefore, the $\Delta\,\mathrm{E}$ spectrum can be described by a Gaussian for a fixed energy of $\mathrm{E}_{\mathrm{Truth}}$ in first approximation.
Within TFTool, energy bins with a width up to 30 GeV (in the default settings) are used. Assuming that all other effects can be neglected, the overall resolution is given by a convolution of the energy spectrum in the energy range being considered and the Gaussian for the detector resolution. The convolution of two functions f and g is defined as

$$(f * g)(t) \overset{\text{def}}{=} \int_{-\infty}^{\infty} f(\tau)\, g(t-\tau)\, d\tau \tag{4.5}$$

$$= \int_{-\infty}^{\infty} f(t-\tau)\, g(\tau)\, d\tau. \tag{4.6}$$

Considering the energy spectrum, e.g. in Figure 4.9, it is observed that the shape changes from bin to bin. Within some energy bins, the shape is almost linear while in other energy bins, e.g. in the peak region, it looks rather like a quadratic function. In an even more detailed approach, the underlying process responsible for the energy spectrum can be studied and evaluated for each energy bin. Anyway, a complete description needs to describe the energy spectrum in each energy bin and convolute the result with a Gaussian resolution function.

On the other hand, the energy bins are chosen to be as small as possible and are often below a width of 20 GeV in the default settings (see Table 4.2). This is below the maximum bin width of 30 GeV applied within the configuration. A limitation of the $\mathrm{E}_{\mathrm{Truth}}$-bin width, that sets the maximum energy range considered in each histogram, has the direct consequence that the maximum value of $\mathrm{E}_{\mathrm{Truth}}$ might be below the default one set in the configuration due to the requirement of a sufficient number of events in each histogram. The advantage of a limited bin width is the guarantee that the energy spectrum does not change significantly within a given bin and can, for simplicity be assumed to be constant. The validity of this assumption depends on the exact energy binning but as shown in Section 4.3.4 and 4.3.5 other effects dominate the resolution spectrum. Hence, in the studies presented, a Gaussian distribution is used as a first approximation for the local fit. The distribution is then modified by considering the description of other effects further discussed below. It should be kept in mind that the actual fitted width of the Gaussian does not correspond one to one to the intrinsic detector resolution due to the assumption of a constant resolution within an energy bin.

4.3.4 Investigation of the Geometrical p_T-cut Dependence

If one considers E_{Truth} bins with relatively low values, it is observed that the mean value is clearly shifted to negative values of ΔE as shown in Figure 4.11. Furthermore, a clear $|\eta|$ dependence of this effect is observed. For larger values of $|\eta|$, the effect is still observed for even larger E_{Truth} bins. Together with the shift of the mean value, an upper bound of ΔE is observed resulting in an edge close to this value. This raises the hypothesis that a cut-off is responsible for the effect. During the generation of the events, the most prevalent cut-off introduced is the $p_T > 25\,\mathrm{GeV}$ cut applied on all reconstructed objects.

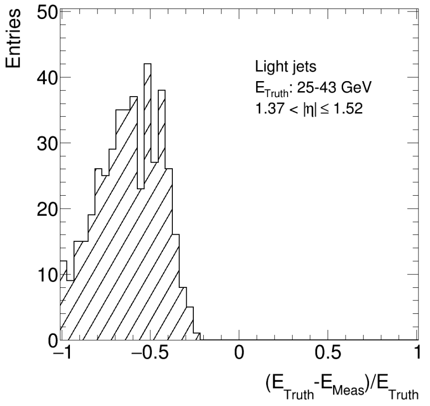

Figure 4.11: Example for the behaviour of the ΔE spectra at lower values for E_{Truth}. An edge close to a maximum value is observed as well as a shift of the mean value.

Considering the energy-momentum relation

$$E^2 = p^2 + m^2 \overset{E>>m}{=} |p|^2, \tag{4.7}$$

where m is the rest mass of the particle, and expressing the magnitude of the momentum by $|p|$ yields

$$E \overset{E>>m}{=} |p| = p_T \cosh\eta \tag{4.8}$$

$$\rightarrow E_{\mathrm{cut}} = p_{T,\mathrm{cut}} \cosh\eta. \tag{4.9}$$

The relation is visualised in Figure 4.12. This means that by applying a cut on p_T, a cut-value on the energy is directly introduced due to their geometrical relation. To verify this effect, the measured energy E_{Meas} is binned in $|\eta|$ with a bin size of 0.1. Afterwards, the minimum value of E_{Meas} in each $|\eta|$ bin is extracted from the energy spectra of e.g. light jets.

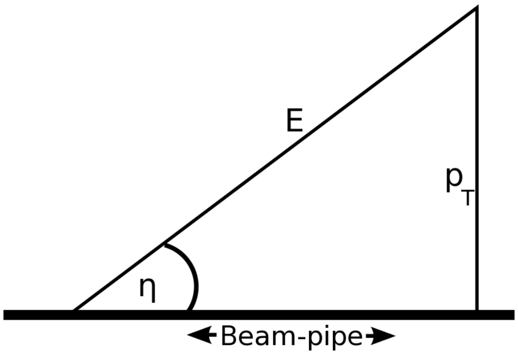

Figure 4.12: Visualisation of the relation between rapidity $|\eta|$, transverse momentum p_T, and energy E, used in Formula 4.9.

In addition, the obtained spectrum is fitted according to Equation 4.9 with the resulting values of

$$E_{\min}(\eta) = (\,0.5 \pm 0.6)\,\mathrm{GeV} + (24.5 \pm 0.5)\,\mathrm{GeV} \cdot \cosh\eta, \tag{4.10}$$

which is in good agreement with the p_T-cut-value of 25 GeV. The result is shown in Figure 4.13. The errors of the fit values are given by the bin widths. It should be noted that $|\eta|$ and the minimum measured energy in an $|\eta|$ bin are highly correlated. Hence, the fit formula is in extraordinary good agreement with each entry.

Figure 4.14 depicts the explanation given above. The entries in the highlighted E_{Truth} bin are only reconstructed if the measured energy is larger than the E_{cut} value of the $|\eta|$ bin considered. Therefore, the measured energy must always be larger than the energy

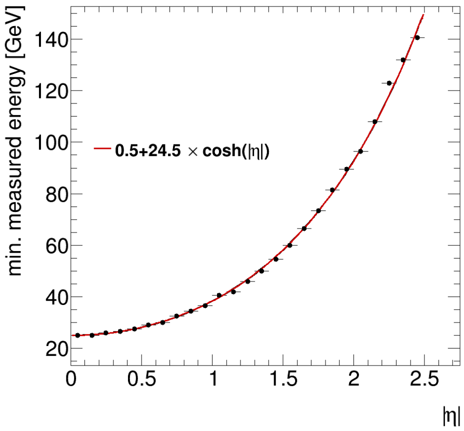

Figure 4.13: The minimum observed energy as a function of $|\eta|$. According to Formula (4.9), the fitted values in Equation (4.10) are obtained.

of the original parton and hence only entries for $\Delta E < 0$ are observed. The distance between the maximum value of the E_{Truth} bin and E_{cut} is the minimal overestimation required and thus results in an edge in the Δ E spectra. For larger $|\eta|$ bins an overlap of many individual cut-values results in a smeared edge in the resolution spectra.
For larger values of E_{Truth}, the cut-value will eventually lie within the E_{Truth} bin. At this point $\Delta E > 0$ becomes possible. At even larger energies, E_{cut} is significantly smaller than the energy of the bin and hence no cut-off effect is seen. This is in good agreement with the observed behaviour.

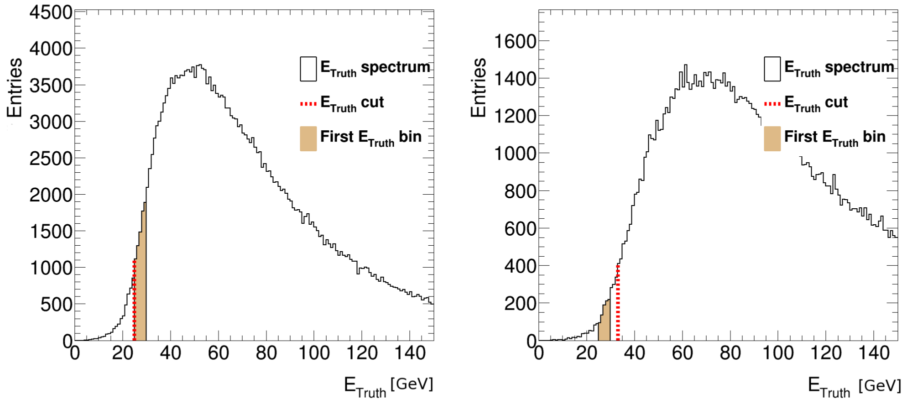

(a) $0.0 \leq |\eta| < 0.8$

(b) $0.8 \leq |\eta| < 1.37$

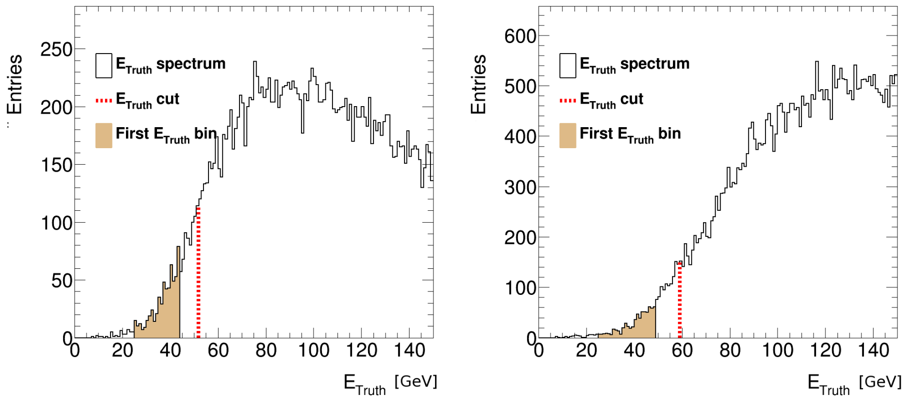

(c) $1.37 \leq |\eta| < 1.52$

(d) $1.52 \leq |\eta| < 2.5$

Figure 4.14: Visualisation of the energy-cut introduced by the p_{T}-cut. Shown is the first bin of a given $|\eta|$ region (brown, filled) as well as the E_{cut} value according to the $|\eta|$ bin (red, dashed line).

Shape of the Δ E spectra To investigate the explanation given above, a simulation of the Δ E spectra is performed. As shown in this paragraph, the behaviour of the Δ E spectra can be reproduced by only assuming the geometrical p_T-cut dependence as the main reason. The simulation is performed in the case of light jets.

At the beginning, for each $|\eta|$ bin, the central regions ($-0.4 < \Delta E < 0.4$) of all E_{Truth} histograms are fitted by a purely Gaussian function as motivated in Section 4.3.3. By taking the width of the spectra into account, the underlying energy resolution is considered. Afterwards, the received widths σ of the Gaussians are fitted in each $|\eta|$ region according to Equation 3.5. The result is shown in Figure 4.15. A cut on the fit is necessary because of the non-Gaussian behaviour at lower energies. This step is similar to the development of $\sqrt{s} = 7$ and $8\,\text{TeV}$ transfer functions. Nevertheless, at low energies, the width of the underlying Gaussian is still expected to follow the energy resolution development and can be extrapolated from the fit.

With the received values for the resolution, the E_{Truth} spectrum used in the MC sample is varied by picking a random number according to

$$E_{\text{sim}}^{\text{Meas}} = E_{\text{Truth}} \cdot \frac{1}{\sqrt{2\pi\sigma^2}} \cdot e^{\frac{(x-1)^2}{2\sigma^2}}. \tag{4.11}$$

In the next step, histograms according to the $|\eta|$ and E_{Truth} binning in TFTool are generated with

$$\Delta E_{\text{sim}} = \frac{E_{\text{Truth}} - E_{\text{sim}}^{\text{Meas}}}{E_{\text{Truth}}}. \tag{4.12}$$

To introduce the $\cosh\eta$ dependence, a histogram is only filled if

$$E_{\text{sim}}^{\text{Meas}} > E_{\text{cut}} = 0.5\,\text{GeV} + 24.5\,\text{GeV} \cdot \cosh\eta_{\text{Truth}} \tag{4.13}$$

is fulfiled according to the fit in the previous section (Equation 4.10). This procedure delivers a simple simulation of the measured energy (and hence Δ E) according to the parton-level energy spectrum by only applying the cut-off effect under study.

In the final step, the Gaussian simulated and the MC Δ E spectra are compared as shown in Figure 4.16. The observed edge can clearly be reproduced. Figure 4.16(b) shows that other physical effects need to be considered in order to explain the tails for $\Delta E > 0$ and the resulting difference in the upper bounds. Other than that, the shape, the upper bound of Δ E and the width agree with the MC sample in all $|\eta|$ regions.

As a conclusion, the energy-momentum relation in combination with the $\cosh\eta$ dependence and a cut on p_T explains the observed Δ E spectra at low energies.

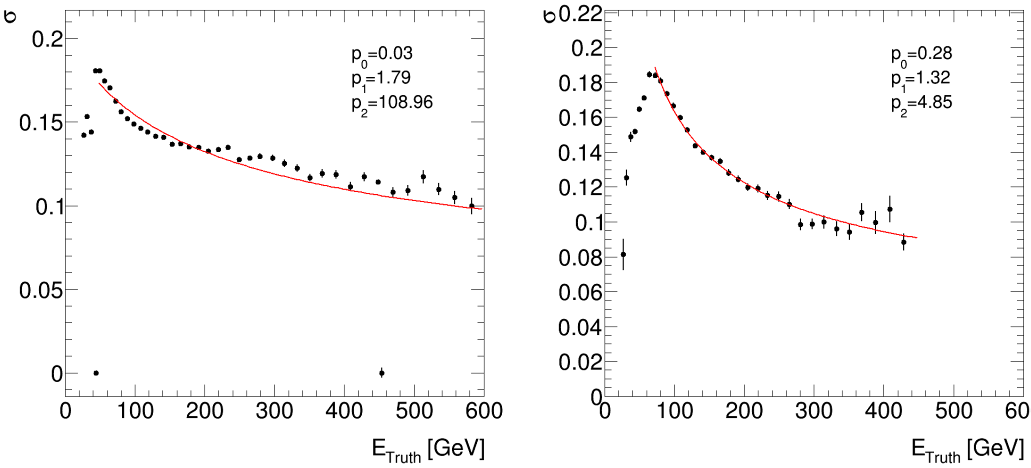

(a) $0.0<|\eta|<0.8$ (b) $0.8<|\eta|<1.37$

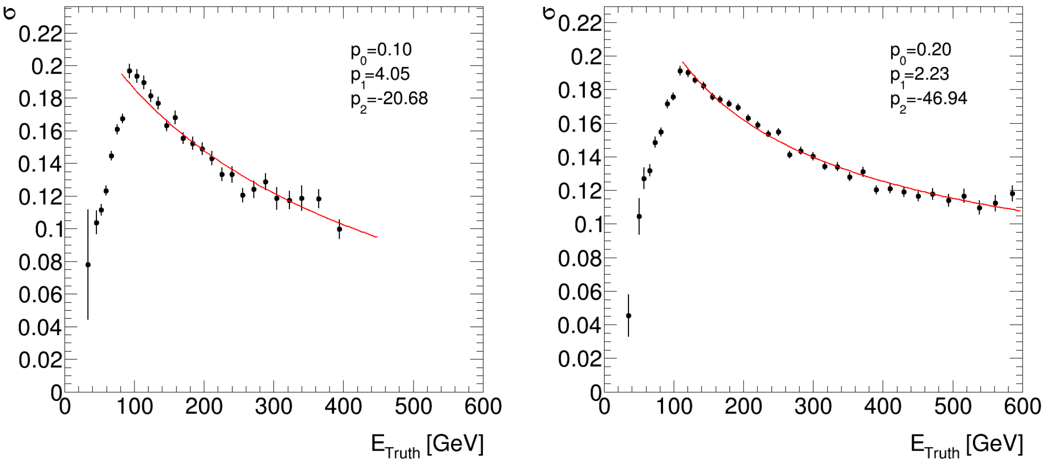

(c) $1.37<|\eta|<1.52$ (d) $1.52<|\eta|<2.5$

Figure 4.15: The widths σ of a simple Gaussian fit in the central region of each E_{Truth} histogram for all four $|\eta|$ regions considered. The widths are fitted according to Formula 3.5. The results are given in the figures.

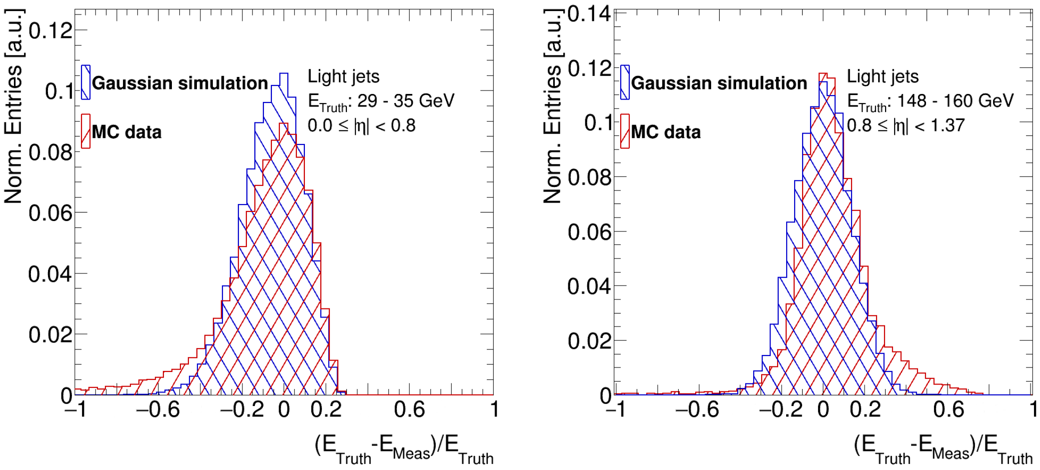

(a) Low energetic
(b) High energetic

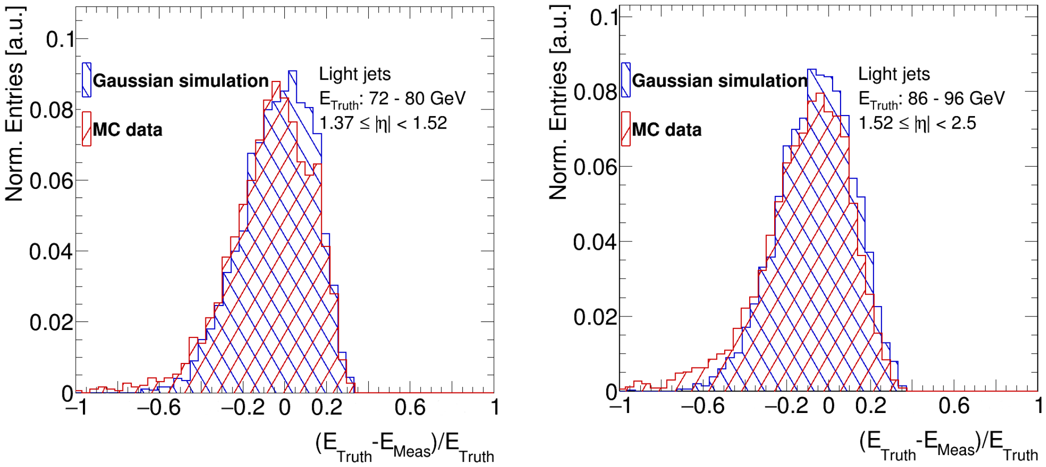

(c) Medium energetic
(d) Medium energetic

Figure 4.16: Comparison of the MC ΔE spectrum and a Gaussian fluctuated E_{Truth} spectrum with E_{cut} according to Equation 4.10. The simulation is done for light jets.

Pile-up Another possible explanation why the measured energy is higher than expected from the parton-level spectrum is pile-up. If more than one parton-parton collision happens at the same time, the measured energy might be an overlap of several events and is hence larger than expected. The mean of events μ per collision, extracted from the MC sample used, is shown in Figure 4.17. To study the influence of pile-up, the Δ E spectra for several selected numbers of events can be compared as shown in Figure 4.18. With the chosen values of μ a large range of pile-up events is considered. Even though the parameter μ has been varied in a wide range, no tendency can be seen in the plots. It can be concluded that pile-up was already corrected for in the calibration of the reconstructed objects and does not need to be considered for the development of new transfer functions.

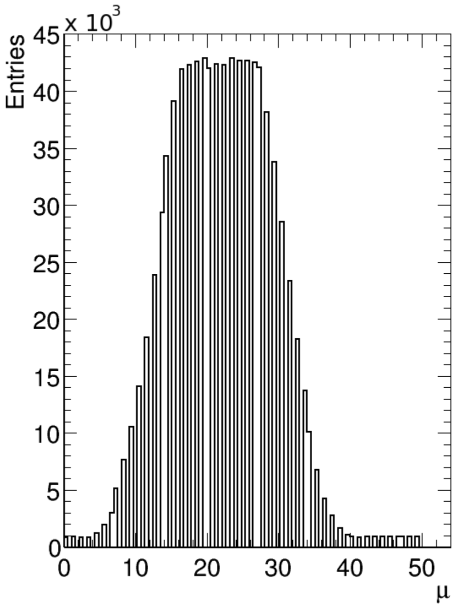

Figure 4.17: Distribution of the number of interactions per event μ.

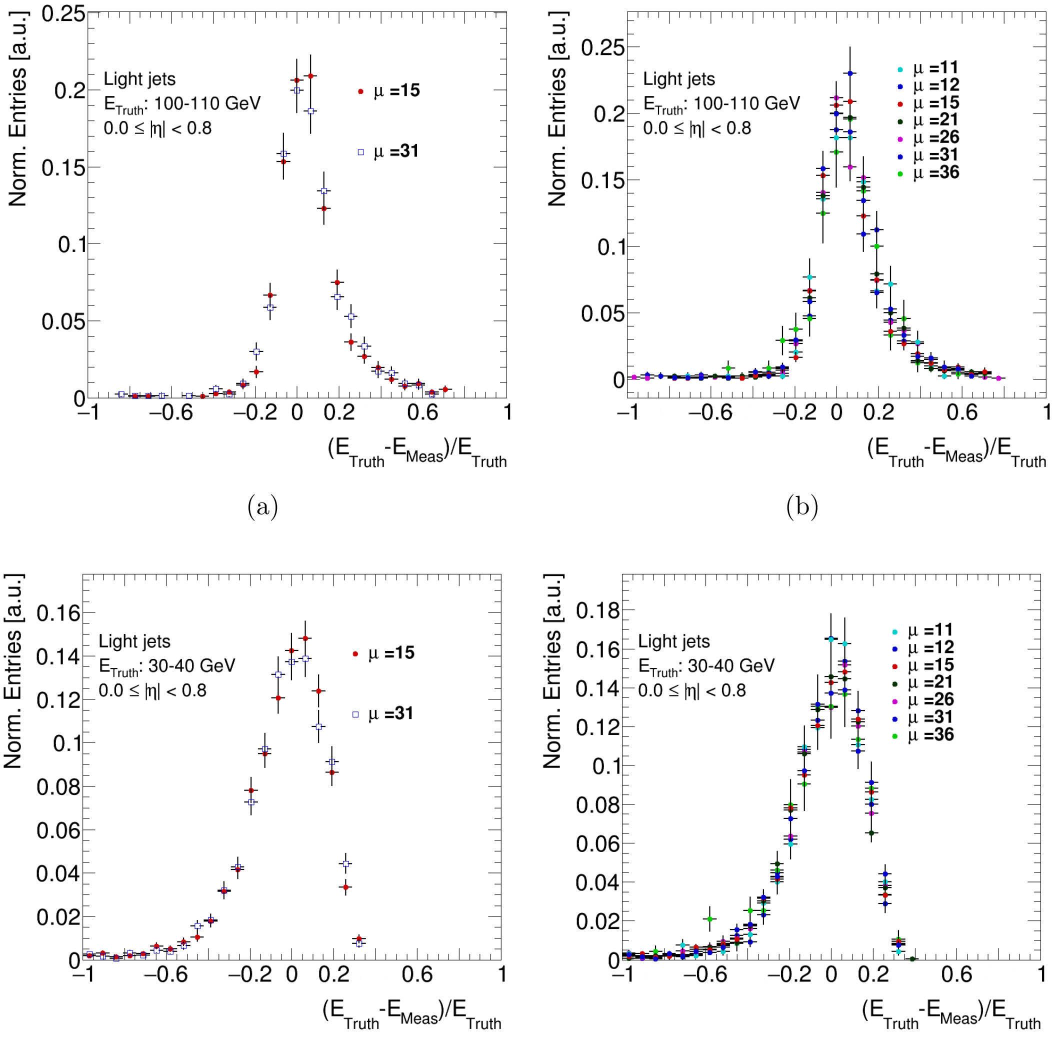

(a) (b)

(c) (d)

Figure 4.18: Comparison of Δ E for different numbers of collisions μ per event. Figures (a) and (c) show an average and a higher pile-up case, whereas Figures (b) and (d), show a more complete overview.

Implementation within KLFitter To account for the shift and the edge in the $\Delta\,\mathrm{E}$ spectra the dependence described in Equation 4.10 needs to be implemented in TFTool. This is done by calculating an upper bound in each $\Delta\,\mathrm{E}$-spectrum that depends on $|\eta|$ and $\mathrm{E}_{\mathrm{Truth}}$. Unfortunately, the default $|\eta|$ binning is very large compared to the functional behaviour shown in Figure 4.13. For the first $|\eta|$-region ($0.0<|\eta|<0.8$) it might be valid to average the value of $\mathrm{E}_{\mathrm{cut}}$ since the hyperbolic cosine does not change significantly in this range. For larger values of $|\eta|$ an average value would be too imprecise.

A smaller binning in $|\eta|$ is therefore a necessity. This has the consequence that either larger $\mathrm{E}_{\mathrm{Truth}}$ bins are needed to sustain sufficient statistics in each histogram or that the energy region that is used for the histograms gets limited. To estimate this effect a bin size of 0.1 in η is chosen in TFTool and 21 additional regions are introduced. From the resulting $\mathrm{E}_{\mathrm{Truth}}$ binning the lower bin boundaries can be readout from the histogram as shown for three selected regions in Table 4.2. Furthermore, the binning in the nominal $|\eta|$-regions (Region 1-4) can be compared.

In the central region ($0.0 < |\eta| < 0.8$) no difference in the energy binning can be observed in the most central region of the new binning ($0.0 < |\eta| < 0.1$). For an intermediate region ($1.0 < |\eta| < 1.1$) the energy bins are in good agreement and only slightly wider. The highest $\mathrm{E}_{\mathrm{Truth}}$-bin, however, is significantly lower around 300 GeV for the same maximum $\mathrm{E}_{\mathrm{Truth}}$-bin width of 30 GeV. In the last chosen region ($2.0 < |\eta| < 2.1$) the first energy bin starts at 69 GeV and not at 25 GeV compared to Region 4. As a consequence, a fit in the lower energetic region is not performed. The bin size for the first bin is already larger than for the other regions. The last bin reaches a maximum energy of 431 GeV which is about 200 GeV less than in Region 4. In summary, it can be said that especially in the higher $|\eta|$ regions the energy binning is affected by a smaller $|\eta|$ bin size up to the point that some energy bins in the lower and higher energy regions are not included anymore.

Nevertheless, the bin sizes do not become too large and it is still possible to perform a fit to a significant number of histograms. For this reason, in the next step, the upper bound in $\Delta\,\mathrm{E}$ can be included in TFTool.

Before implementing an actual function that forms an edge in the $\Delta\,\mathrm{E}$ spectrum, a single cut-value needs to be calculated that originates from Equation 4.9 and translated into relative energy differences shown in the $\Delta\,\mathrm{E}$ spectra. The creation of the histograms and the fitting procedure are two different steps within the code. The issue with this separation is that when the limits for the parameters of the fit are calculated and set, no information of $|\eta|$ or $\mathrm{E}_{\mathrm{Truth}}$ for the fitted histogram are available and hence $\mathrm{E}_{\mathrm{cut}}$ cannot be calculated. One way to solve this is to use the name of the histogram to store and readout the required information. The $\Delta\,\mathrm{E}$ value where the edge is expected can then be calculated and used in combination with a fit function as discussed in Section 4.3.6.

Table 4.2: Lower edge of the $\mathrm{E}_{\mathrm{Truth}}$ bins for an $|\eta|$ binning of 0.1 and the nominal ones in units of GeV.

Histo.	Region 1	Region 2	Region 3	Region 4			
	$0.0<\lvert\eta\rvert<0.8$	$0.8<\lvert\eta\rvert<1.37$	$1.37<\lvert\eta\rvert<1.52$	$1.52<\lvert\eta\rvert<2.5$	$0.0<\lvert\eta\rvert<0.1$	$1.0<\lvert\eta\rvert<1.1$	$2.0<\lvert\eta\rvert<2.1$
0	25	25	25	25	25	25	69
1	29	29	43	48	29	32	91
2	35	35	50	54	35	38	110
3	41	41	57	62	41	44	120
4	47	47	64	70	47	51	131
5	54	54	72	78	54	58	143
6	61	61	80	86	61	65	154
7	69	69	89	96	69	73	167
8	77	77	99	105	77	82	180
9	85	85	109	116	85	91	193
10	95	95	119	126	95	100	207
11	104	104	130	137	104	110	221
12	114	114	141	149	114	120	236
13	125	125	153	161	125	131	251
14	136	136	165	174	136	142	267
15	148	148	178	187	148	154	283
16	160	160	191	200	160	167	300
17	172	172	219	214	172	179	317
18	185	185	234	229	185	193	334
19	199	199	249	244	199	207	353
20	213	213	264	259	213	221	371
21	227	227	281	275	227	236	401-431
22	242	242	297	292	242	267-297	—
23	258	258	314	309	258	—	—
24	273	273	332	326	273	—	—
25	290	290	350	344	290	—	—
26	307	307	380-410	363	307	—	—
27	324	324	—	382	324	—	—
28	342	342	—	401	342	—	—
29	360	360	—	421	360	—	—
30	379	379	—	441	379	—	—
31	399	399	—	462	399	—	—
32	419	419-449	—	484	419	—	—
33	439	—	—	506	439	—	—
34	460	—	—	528	460	—	—
35	581	—	—	551	481	—	—
36	503	—	—	574	503	—	—
37	525	—	—	598-622	525	—	—
38	548	—	—	—	548	—	—
39	571	—	—	—	571	—	—
40	595-619	—	—	—	595-619	—	—

4.3.5 Undetected Neutrinos

For each of the five flavours considered (the top-quark is kinematically forbidden), the Δ E spectra can be compared as shown in Figure 4.19. The spectra do not use the binning of TFTool and show all energy ranges of the central $|\eta|$ region at once. Even though this merges all energy ranges the overall difference between the quark-flavours is not affected. In addition, Figure 4.20 shows a comparison for the central $|\eta|$ region with 50 GeV bins for the bottom and down flavour case. Comparing these spectra shows a shift of the Δ E spectrum to higher values for higher quark-generations.

Considering hadrons also means that lighter ones can be produced by heavier ones. For up and down type quarks, pions are almost exclusively formed in the final state. They dominantly decay either into photons (π^0) or into a $\mu + \nu$ ($\pi^{\pm}$). The neutrino is not measured and hence the energy of the original yet is not measured completely. In addition, pions can be produced by kaons that are formed by an initial strange-quark. Since kaons can decay into a neutrino and a lepton in the final state but are also very likely to produce pions with an additional W-boson in the decay, more neutrinos are expected for kaons than for pions on average. The exact percentage of the leptonic branching ratio depends on the hadron that was formed before the decay. Typical values are in the order of 10-20 % [12]. In summary, the energy losses of a strange-quark should be more distinct than for up and down-quarks due to the decay-chain considered above. In the same way it can be argued for charm and bottom-quarks and the corresponding hadrons. They decay into lighter hadrons during which additional neutrinos can be produced. For a higher generation, more neutrinos are expected from this process and hence the not measured energy is expected to be larger.

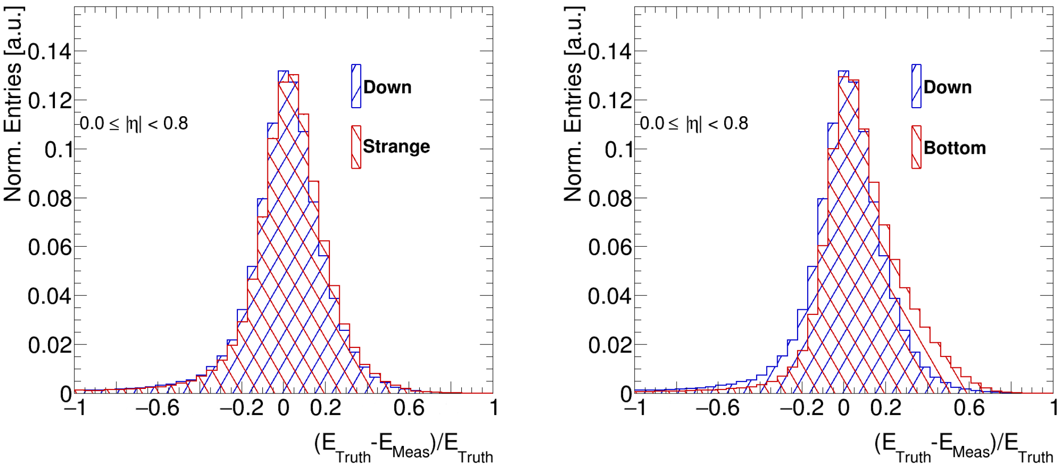

(a) Down vs. Strange

(b) Down vs. Bottom

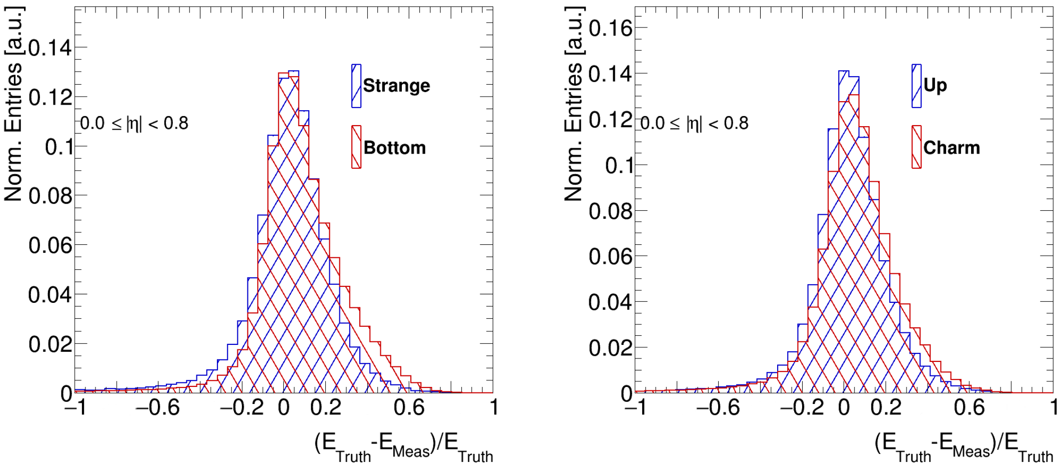

(c) Strange vs. Bottom

(d) Up vs. Charm

Figure 4.19: Comparison of the Δ E spectra for five different quark flavours. The spectra show the overlap of all energy bins in the $0.0 \leq \eta < 0.8$ region. The bin errors are below the minimal line width.

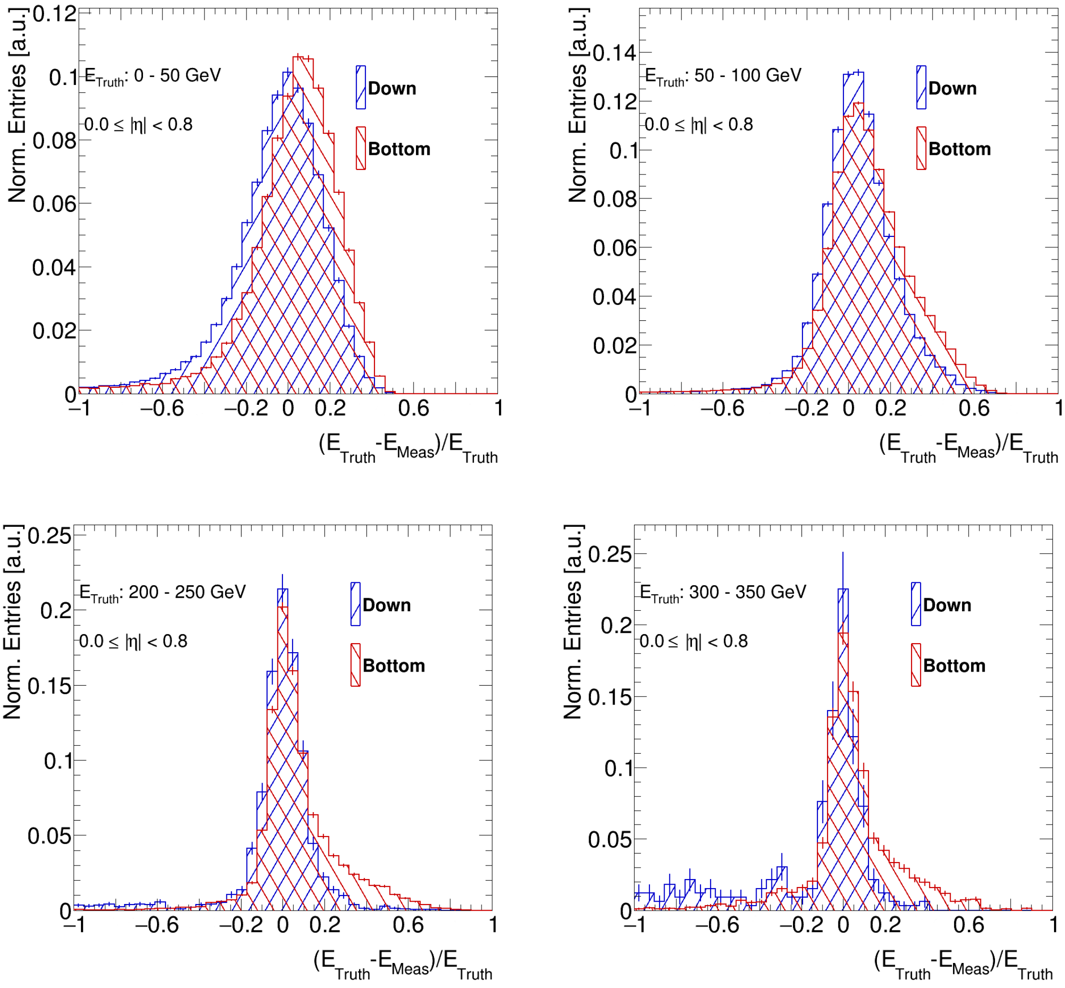

Figure 4.20: Comparison of the Δ E spectra for the bottom and down flavour in the central ($0.0 \leq \eta < 0.8$) region. $\mathrm{E}_{\mathrm{Truth}}$ bins with a size of 50 GeV are shown.

Decays Inside of Jets Since neutrinos cannot be observed directly, the distinction whether a leptonic decay within a jet occurred or not has to be classified by the corresponding lepton.

Before being able to study the effect, the lepton/jet overlap removal in the MC reconstruction must be disabled. By doing so, two objects can have the same η and ϕ coordinates and are not merged into one object. All other cut criteria are unchanged in comparison to the original sample. By disabling the overlap removal, several cases for each parton-lepton combination can be considered as shown in Figures 4.21(a) and 4.21(b).

Before discussing the cases in detail, some general properties of the studies should be mentioned. A jet and a muon are called overlapping if their distance in ΔR is smaller than 0.3. This value is chosen to be consistent with the matching requirement for jets.

The lepton is considered when it is matched or unmatched, whereas the jets are always required to be matched. Otherwise it would not be possible to distinguish different types of jets.

It can be seen in Figure 4.21(c) that the spectrum of leptonic decaying b-jets is wider than the spectra for light jets considered before in TFTool. This can be explained by the event selection. First of all, by default, only one lepton is selected. If there are other ones in the event that do overlap with the jets, they may be outside the cut criteria, e.g. below the $\mathrm{p_T} = 25\,\mathrm{GeV}$ cut. Hence, they are not seen as a selected lepton. The jet energy is additionally reduced by the energy of the lepton which is not considered to belong to the jet anymore, due to disabling the overlap removal. As a consequence, larger energy losses are expected. This also means that speaking of the (not) overlapping case between the lepton and a jet only refers only to the selected lepton in the event and not to all possible leptons. The obtained $\Delta\,\mathrm{E}$ spectra cannot be used to study transfer functions in TFTool and are therefore exclusively useful for these studies. From the cases considered below, the differences between the histograms are of particular interest to distinguish the behaviour of the chosen selection.

Another difference to the default TFTool studies is the changed binning from previously 41 to 11 bins. This is necessary because of the smaller statistics in the overlap and the unmatched case which turns out to be the important one. To allow for cross-checks, the bin size is chosen to be identical in all cases. An overview of the number of entries of the subfigures in Figure 4.21 is given in Table 4.3.

Since, except for b-jets, in experiments it cannot be distinguished between the different up- and down-types of the quarks considered and the effect is expected to be strongest for heavy quarks, b-jets are used for the comparison. As an example, muons have been chosen as lepton.

In the first case, shown in Figures 4.21(a) and 4.21(c), the distance between the selected muon and the jet considered is larger than $\Delta R = 0.3$, they do not overlap. This means that the jet and the muon are not geometrically related. Furthermore, it can be distinguished whether the muon is matched or not. If it is matched, then the muon originates from the W-boson. Typically, this is the optimal case where muon and jet have correctly been reconstructed. Hence, the $\Delta\,\mathrm{E}$ spectrum of the jet should look as expected, centred around zero with additional entries for $\Delta\,\mathrm{E} > 0$ due to additional losses as explained above. In the case that the muon is unmatched it must originate from another source. Since it does not overlap with the jet, it is, again, not geometrically aligned to the jet. This means that the $\Delta\,\mathrm{E}$ spectrum of the jet that is considered is not affected and should look identical to the first one as it is observed.

In the second case, the muon and the jet do overlap. Again, it can be distinguished whether the muon is matched or not. If the muon is matched, it still originates from the W-boson. This scenario occurs if, for example, the objects are boosted similar to the phenomena discussed in Section 4.2. The muon and the jet are still not related in their kinematics and hence the $\Delta\,\mathrm{E}$ spectrum should be similar to the no overlap case. The spectrum in this case is narrower. The explanation for this is that in Figure 4.21(d) it can be distinguished between additional decays inside a jet and decays independent of the jet. In Figure 4.21(c) it can only be be excluded that the selected muon does not overlap with the jet considered. It might be that there is an overlap with another lepton that is not selected. Therefore. the $\Delta\,\mathrm{E}$ spectrum shows an overlap of two underlying contributions. The spectrum for the overlap and matched lepton case on the other hand looks much more similar to the original spectra in TFTool since only a contribution from the selected muon occurs.

Finally, the muon might be unmatched. This is the interesting case showing additional leptonic decays inside the jet with an escaping neutrino. Similar to the unmatched case before, this source might be independent of the jet but due to the overlap with the jet a strong contribution from jet related decays is expected. In Figure 4.21(d) this can be seen by a shift of the mean towards $\Delta\,\mathrm{E} > 0$ which is not observed in the matched case. Overlaying the matched and the unmatched spectra could in principle reproduce the shape observed in Figure 4.21(c) if the number of entries are respected.

The studies discussed above have been performed for leptonic and hadronic decaying b-quarks. Comparing the muon in combination with the b-jet from the leptonically decaying top-quark in Figures 4.21(d) and 4.21(c) with the b-jet from the hadronic case in 4.21(f) and 4.21(e) two main differences can be observed that are not expected at first glance since the b-jets should behave similar.

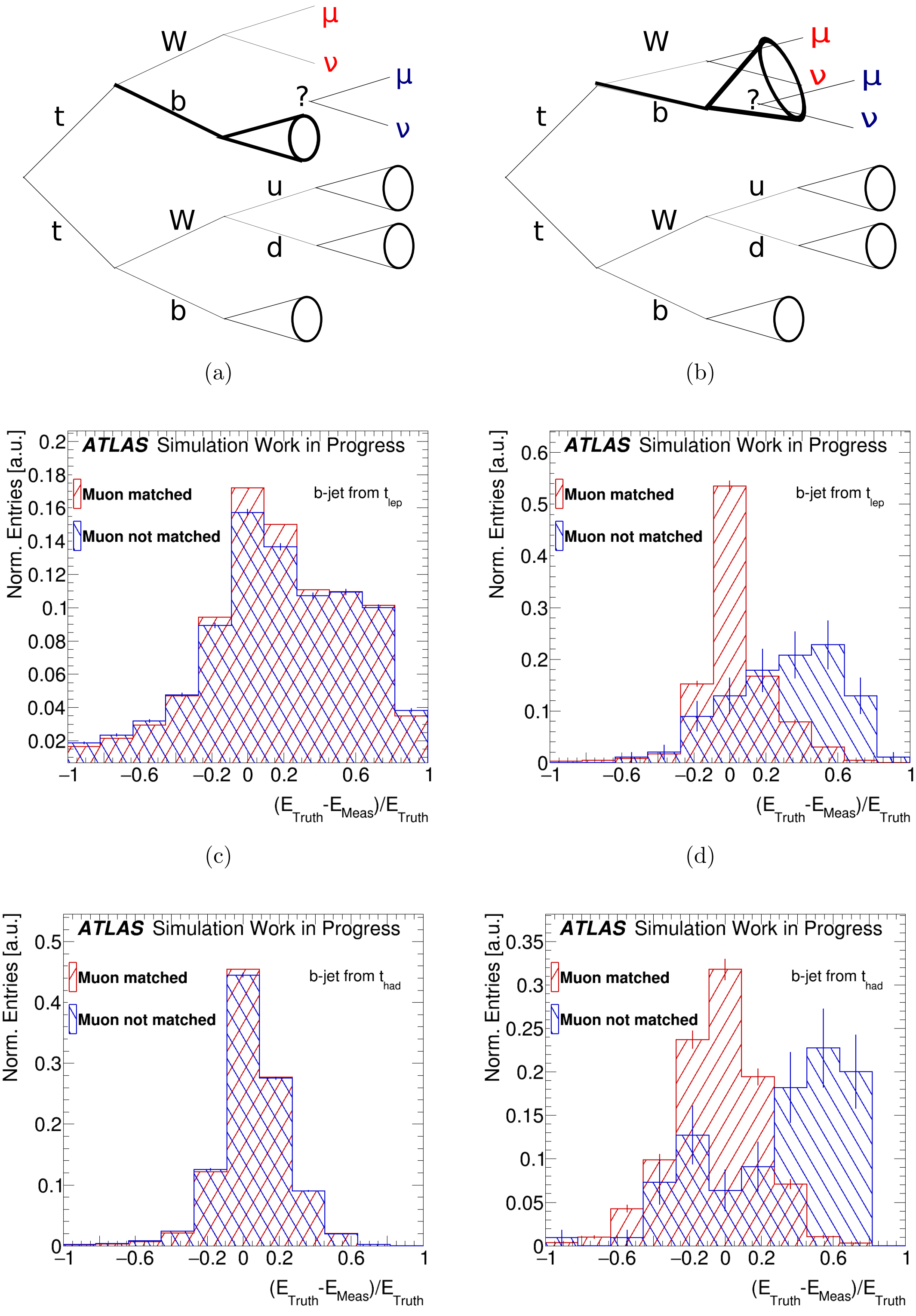

(a) (b)

(c) (d)

(e) (f)

Figure 4.21: Overview of the no-overlap (a) and overlap cases (b) together with several Δ E spectra. Figures (c) and (d) show the spectra for the b-jets from the leptonic side, whereas the spectra for the b-jets from the hadronic decaying top-quark are given in Figures (e) and (f) in the cases of no-overlap (left) and overlap (right) between muon and jet. In both cases, the muon can be matched or unmatched.

Table 4.3: Entries of Figure 4.21 for the studies of additional leptonic decays within a b-jet from the hadronic or leptonic decaying top-quark. In addition, the entries for the spectra of up- and down-type quarks are shown.

Quark	Muon	
Overlap		
	matched	unmatched
b from $\mathrm{t_{had}}$	2112	110
b from $\mathrm{t_{lep}}$	4225	101
up type	4210	207
down type	17024	489
No overlap		
	matched	unmatched
b from $\mathrm{t_{had}}$	$1.08\ \times 10^{6}$	32638
b from $\mathrm{t_{kep}}$	$1.62\ \times 10^{6}$	29462
up type	$1.56\ \times 10^{6}$	52723
down type	$1.62\ \times 10^{6}$	49835

The b-jets from the hadronically decaying top-quark exhibit a smaller width of the $\Delta\,\mathrm{E}$ distribution in the no-overlap case compared to the spectrum for b-jets from the leptonic decaying top-quark (Figure 4.21 (left)). A tail for $\Delta\,\mathrm{E} > 0$ is visible in both cases but for b-jets from the leptonic side the tail is visible as a rather flat plateau between $\Delta\,\mathrm{E} = 0.2$ and $\Delta\,\mathrm{E} = 0.8$, whereas for the hadronic side it is a rather steep edge between $\Delta\,\mathrm{E} = 0.2$ and $\Delta\,\mathrm{E} = 0.6$.

Figure 4.22 compares the entries in different $\mathrm{E_{Truth}}$-bins for b-jets from the hadronically decaying top-quark and the leptonically decaying top-quark. The entries are normalised for each of the two cases considered separately. It is observed that in all cases considered ((no) overlap and (not) matched muon) b-jets from the leptonically decaying top-quark have, on average, more entries in $\Delta\,\mathrm{E}$ spectra with a higher $\mathrm{E_{Truth}}$-bins.

In addition, for higher energy bins, the b-jet from the leptonic side shows a slightly stronger distinct tail for $\Delta\,\mathrm{E} >\ 0$ as shown in Figure 4.23. Further examples can be found in the appendix.

For different energy bins, different physical aspects are relevant. The edge in the $\Delta\,\mathrm{E}$ spectra, discussed in Section 4.3.4, is more important for lower energy bins than for higher ones where the $|\eta|$-dependent energy cut can be neglected. In the latter case, the tail for $\Delta\,\mathrm{E} > 0$ is hence more distinct.

The difference in $\Delta\,\mathrm{E}$ spectrum without energy binning (Figure 4.21) has the following consequence. Higher energy regions where a stronger tail for $\Delta E > 0$ is observed are weighted more for b-jets from the leptonic side than from the hadronic one. This is a direct consequence of the ratio between the entries in the ΔE spectra for the two cases of b-jets. In addition, the energy losses are more distinct for b-jets from the leptonic side. Combining these two effects results in a wider ΔE spectrum for the b-jet from the leptonic side in the overall ΔE spectrum where no energy binning is applied.

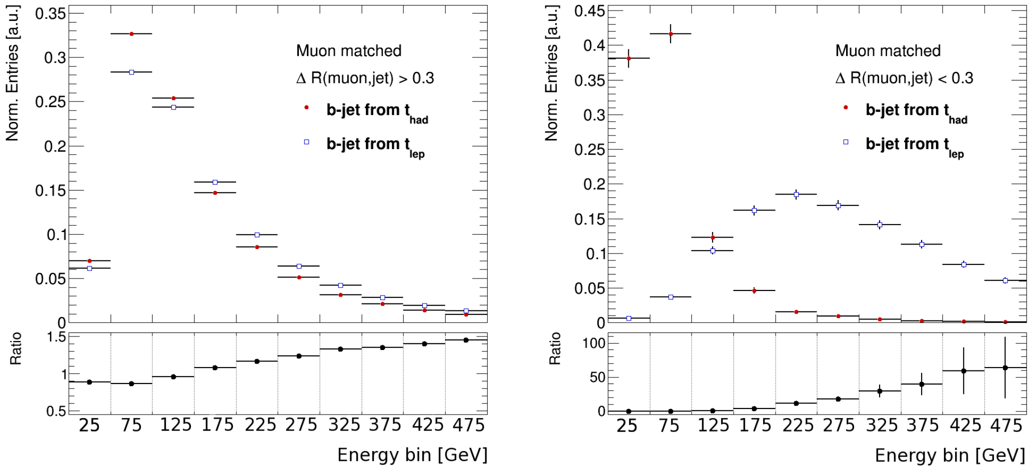

(a) Muon matched, no overlap

(b) Muon matched, overlap

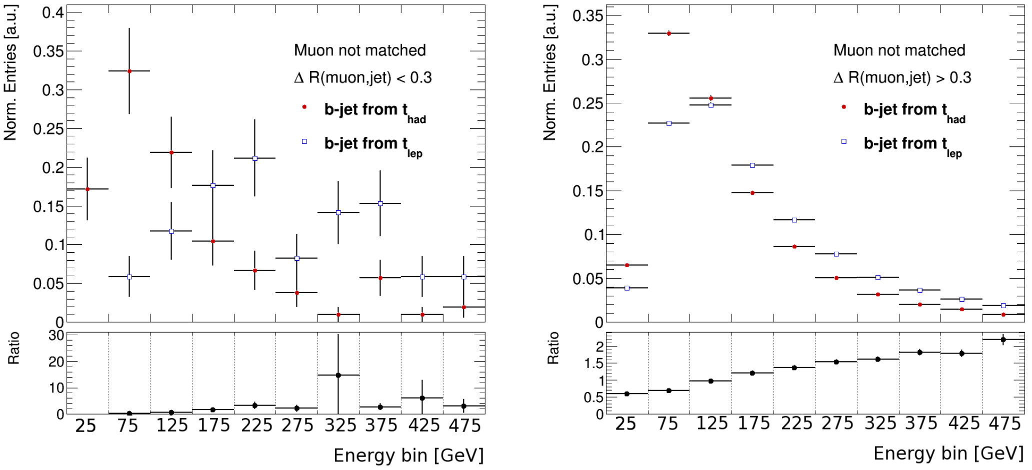

(c) Muon unmatched, overlap

(d) Muon unmatched, no overlap

Figure 4.22: Comparison of the normalised entries in the ΔE spectra for the b-jets from the hadronic and leptonic decaying top-quark for the case of a (not) matched muon and and (no) overlap between b-jet and muon.

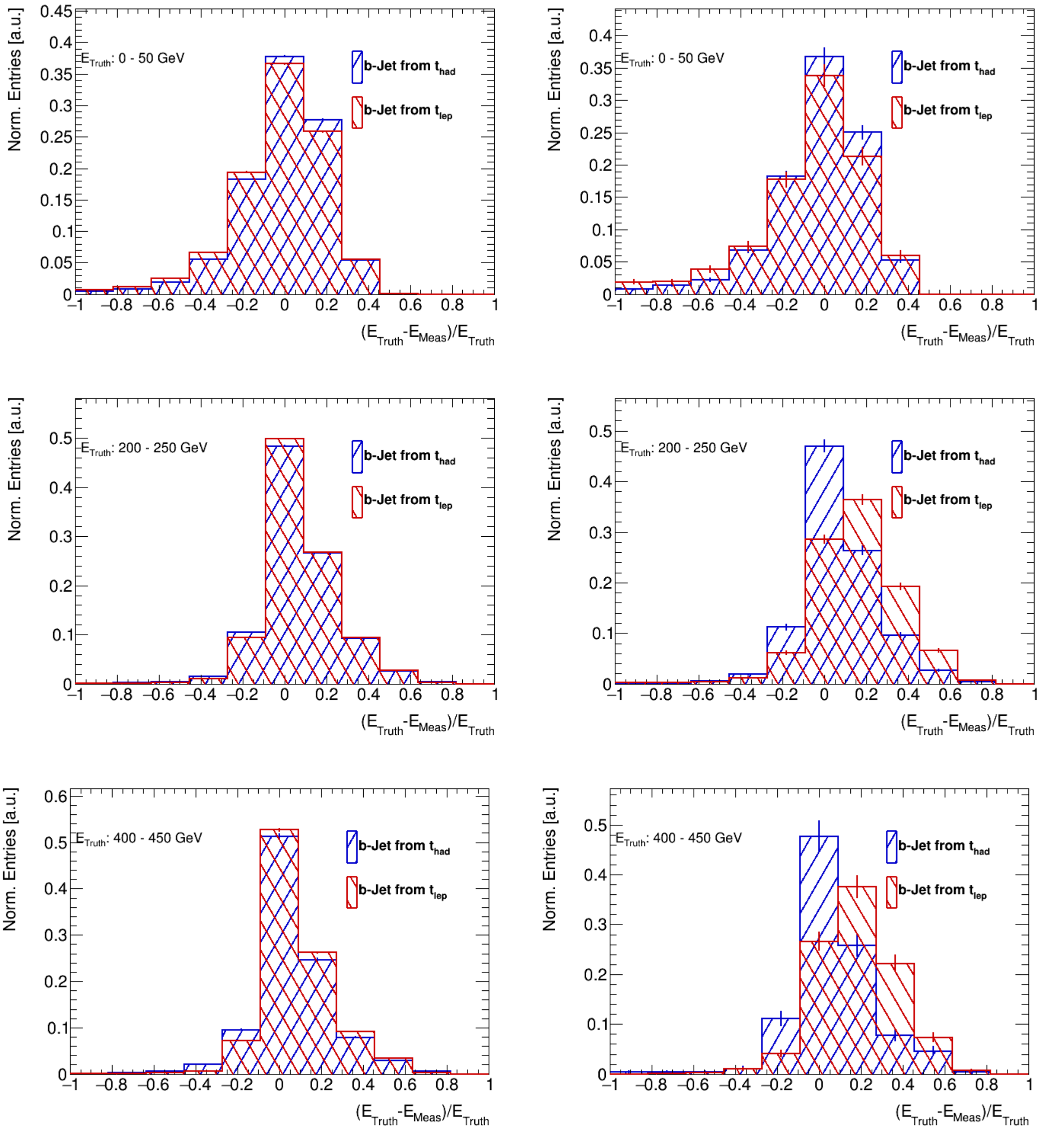

Figure 4.23: Comparison of the Δ E spectra for b-jets from the hadronic/leptonic decaying top-quark in different energy regions. The cases of no overlap between the lepton and the jet for matched (left) and unmatched (right) muons are compared. The bin errors are partly below the line width.

The other difference in Figure 4.21(f) is the second peak around zero in the unmatched muon and overlapping case for b-jets from the hadronic side. It is not observed for b-jets from the leptonic side. This difference can again be explained by the ratio between the entries in the $\Delta\,\mathrm{E}$ spectra for b-jets from the leptonically and hadronically decaying top-quark as shown in Figure 4.22.
First of all, the peak around $\Delta\,\mathrm{E} = 0.6$ originates from the unmeasured energy for both types of b-jets considered. A difference is observed in the central region around $\Delta\,\mathrm{E} = 0.0$. The central peak originates from the $\Delta\,\mathrm{E}$ spectra where the η-dependent $\mathrm{p_T}$-cut needs to be considered. The $|\eta|$-dependency of the $\mathrm{p_T}$-cut causes some b-jets with low energy to fail the $\mathrm{p_T}$-cut. An edge in the $\Delta\,\mathrm{E}$ spectra is therefore expected especially for lower energetic b-jets. In the combined spectrum, these jets do not contribute to the tail for higher $\Delta\,\mathrm{E}$ values and result in a second underlying spectrum. As a result, an overlap between the $\Delta\,\mathrm{E}$ spectrum that contains energy losses and the $\Delta\,\mathrm{E}$ spectrum that shows an edge is observed.
In the case of b-jets from the hadronic side this contribution is more distinct since more jets with a lower energy contribute to the overall $\Delta\,\mathrm{E}$ spectrum as shown in Figure 4.22. For b-jets from the leptonic side the energy of a single jet is higher on average. The η-dependent $\mathrm{p_T}$-cut can be neglected more often. As a consequence, the peak around zero is suppressed in the unbinned $\Delta\,E$ spectrum and the tail for $\Delta\,E\ > 0$ is more distinct.

It was observed that the b-jets from the leptonically and hadronically decaying top-quark have a different distribution of entries in the $\Delta\,\mathrm{E}$ spectra. The only difference between the two types of b-jets is the fact that one of them is produced by a top-quark and the other one by an anti-top-quark. From a kinematical point of view this should have no influence on the energy of the b-jets.
What was found instead is that the difference originates from the matching procedure. Figure 4.24 compares the energy spectra of the b-jet from the leptonic and hadronic side in the case of a matched and unmatched jet. It can be seen that for the case of a matched jet (Figure 4.24 (left)) the b-jet from the hadronic decaying top-quark tends to have less energy on average. This is in agreement with the behaviour observed in Figure 4.22 before where only matched b-jets have been considered. In the unmatched case the behaviour is opposite. The b-jets from the leptonic decaying top-quark tends to have less energy on average. The difference is observed in the reconstructed and the parton-level energy spectrum of the b-jets.

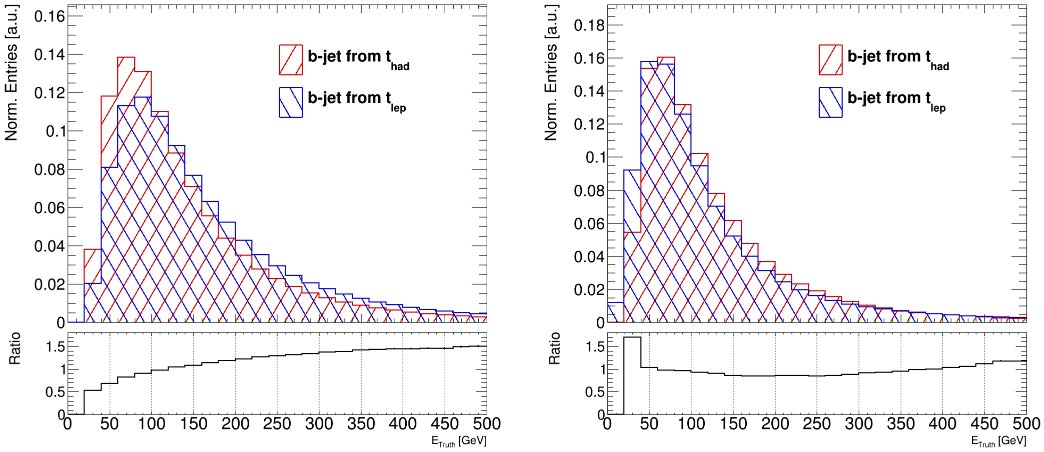

(a) Reconstructed energy.

(b) Reconstructed energy.

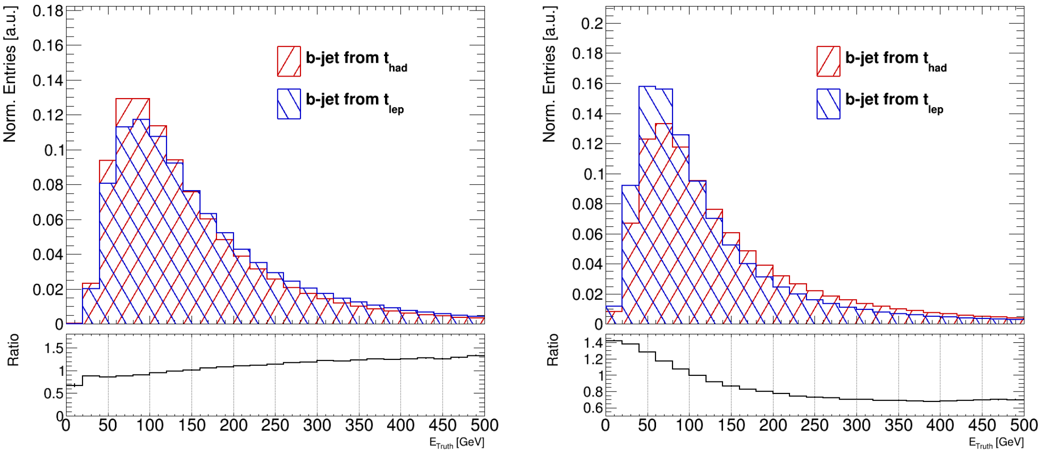

(c) Parton-level energy.

(d) Parton-level energy.

Figure 4.24: The energy spectra of the b-jets from the leptonic and hadronic decaying top-quarks for matched (left) and unmatched (right) jets. The errors are below the minimal line width.

It remains to show that the unreconstructed energy is in agreement with the energy of the neutrinos produced in the decay on an event by event basis. This can be done by considering the parton-level energy of the neutrinos. In the current MC sample this is not possible since only the parton-level information of neutrinos from the W-boson that originates from the top-quark decay is available.

It can be concluded that the phenomena discussed in this section explain the tail for $\Delta\,\mathrm{E} > 0$. At low energy bins the energy losses are not observed due to the edge that is caused by the η-dependent $\mathrm{p_T}$-cut. Only when this cut criterion is negligible, the additional energy losses are observed in the $\Delta\,\mathrm{E}$ spectra.

The origin of the unmeasured energy are neutrinos that are produced in a chain of decays. The neutrinos can originate either from a W-boson, emerging from a hadron decaying into a lighter hadron, or from a leptonic decay of the hadron itself. They are not measured in the detector and therefore the measured energy of the jet is underestimated.

The significance of this result could be improved if more than one lepton is considered at the same time per event. Using the current event selection and allowing multiple muons, only 0.8% of the events contain more than one selected muon. Hence, background contributions of unselected muons are expected.

In addition it was found that the matching procedure behaves different for b-jets from the hadronically and leptonically decaying top-quark. This effect is worth further investigations since the matching criterion is crucial for KLFITTER and TFTOOL related studies.

Implementation within KLFitter It was shown that neutrinos contribute to energy losses in the measured jet energy spectrum. The next step is a description of the energy spectrum of the neutrinos since this directly describes the energy that is unmeasured. Based on this description the not measured energy can be described in TFTOOL and hence the tails for $\Delta\,\mathrm{E} > 0$.

In order to describe the energy spectrum of the neutrinos, the underlying decay that produces the neutrinos needs to be considered, e.g. the decay of a pion into a muon and a neutrino. For this two-body decay, the kinematic properties of the decay products can be calculated as shown in the following.

In the SM the mass of the neutrino is zero and the energy is given by $E_\nu = p_\nu c$. In the rest frame of the pion, the muon moves in the exact opposite direction with the same absolute momentum $|p_\mu|c = |p_\nu|c = |p|c$ (momentum conservation). The mass difference between the pion and the final state muon $Q = M_{\pi^\pm} - m_\mu \approx 33.91\,\mathrm{MeV}$ gives the total energy that can be distributed between the decay products. Therefore, the energy-momentum relationship for the muon can be written as

$$(pc)^2 = E_\mu^2 + 2E_\mu m_\mu c^2 \qquad \text{with} \tag{4.14}$$

$$E_\mu = Q - pc, \tag{4.15}$$

as the total kinetic energy of the muon. This term can be expanded in terms of Q,

$$(pc)^2 = Q^2 - 2pcQ + (pc)^2 + 2(Q - pc)m_\mu c^2, \tag{4.16}$$

from which the energies of the decay products can be calculated via

$$\begin{aligned} E_\nu = pc &= \frac{Q^2 + 2M_{\pi^\pm} m_\mu c^2}{2(Q + m_\mu c^2)} = 29.79\,\mathrm{MeV} \\ E_\mu &= 33.91\,\mathrm{MeV} - 29.79\,\mathrm{MeV} = 4.12\,\mathrm{MeV}. \end{aligned} \tag{4.17}$$

Formula 4.17 shows that the neutrino has a fixed energy in the rest frame of the $\pi^\pm$. To get the energy in the laboratory frame a Lorentz transformation along the direction x of the particle defined as

$$\mathrm{p}'_\mathrm{x} = \gamma(\mathrm{p_x} + \mathrm{vE/c^2}) \tag{4.18}$$

$$\mathrm{E}' = \gamma(\mathrm{E} + \mathrm{vp_x}) \tag{4.19}$$

has to be applied. Since the energy of the pion defines the boost, the shape of the energy spectrum of the pion equals the energy spectrum of the neutrino.

The energy spectrum of the mother particle is given by the fragmentation functions as discussed in Section 2.1.3. For b-quarks, the Peterson fragmentation function (Equation 2.16) yields a good description. For light quarks the more general form (Equation 2.14) can be used.

The neutrino spectrum can then be convoluted with the energy resolution function to obtain a physically motivated transfer function as discussed in the next section.

4.3.6 Implementation of Fit Functions

This section covers the implementation of new transfer functions within TFTool. The functions to be used are based on the physical effects discussed in the previous sections. In addition, alternatives that are not motivated by a physical argumentation are presented that have the same shape as the physically motivated functions but show some advantages in the implementation and the fitting procedure.

$\mathbf{p_T}$-cut dependence Up to now it was found that an $|\eta|$-dependent edge of the $\Delta\,\mathrm{E}$ spectra can be implemented within TFTool. For each histogram an upper bound of $\Delta\,\mathrm{E}$ can be defined within TFTool that only depends on $|\eta|$ and $\mathrm{E}_{\mathrm{Truth}}$. The value is calculated according to the analytic expression from Equation 4.10. Furthermore, the upper bound can be loosened to allow for variations during the fitting procedure. What is still needed is the translation of the value for the upper bound into a functional form that can describe the edge in the $\Delta\,\mathrm{E}$ spectra. One possible option is the combination of a Gaussian, representing the $\Delta\,\mathrm{E}$ spectrum, with a function that provides an edge such as the error function. It is very important that the function that is used can make use of the $|\eta|$-dependent upper bound that can be calculated precisely for each histogram.
Figure 4.25 shows an examples of a variation of an error function convoluted and multiplied with a Gaussian distribution. The error function and the corresponding variation h(x) are defined in the following way

$$h(x) = 1 - \mathrm{erf}(a * (x - b)) \tag{4.20}$$

$$\mathrm{erf}(x) = \frac{1}{\sqrt{\pi}} \int_{-x}^{x} e^{-t^2}\,\mathrm{d}t \tag{4.21}$$

$$= \frac{2}{\sqrt{\pi}} \int_{0}^{x} e^{-t^2}\,\mathrm{d}t. \tag{4.22}$$

The parameter a defines the sharpness of the edge, whereas parameter b defines the position of the edge. The latter parameter therefore corresponds to the upper bound in the $\Delta\,\mathrm{E}$ spectra.
For the convolution, defined in Section 4.3.3, a Gaussian distribution with a width of $\sigma = 0.1$ is used (Figure 4.25, left). For the multiplication (Figure 4.25, right) $\sigma = 0.3$ is used for a better visualisation. In both cases, a typical $\Delta\,\mathrm{E}$ range for jets from -1 to 1 is shown.
It is observed that in this combination only a multiplication of a Gaussian function and the error function could reproduce the shape of the spectra with an edge at zero. Furthermore, it is possible to vary the position and the sharpness of the edge with the parameters defined in the variation. This allows for adjustments during the fitting procedure if necessary but can also be excluded by fixing one of the parameters. In the next step, the multiplication of a Gaussian and a modified error function was implemented within TFTool as a fit function. First examples of fits to the MC sample are shown in Figure 4.26 for different regions. The parameters have been tuned for the light jets case. The shift of the maximum together with the upper bound are fitted reasonably well as can be seen in Figure 4.26(a).

In some cases, however, the fit does not perform perfectly as shown in Figure 4.26(c). As expected, right tails can still not be fitted as shown in Figure 4.26(b) and 4.26(d).

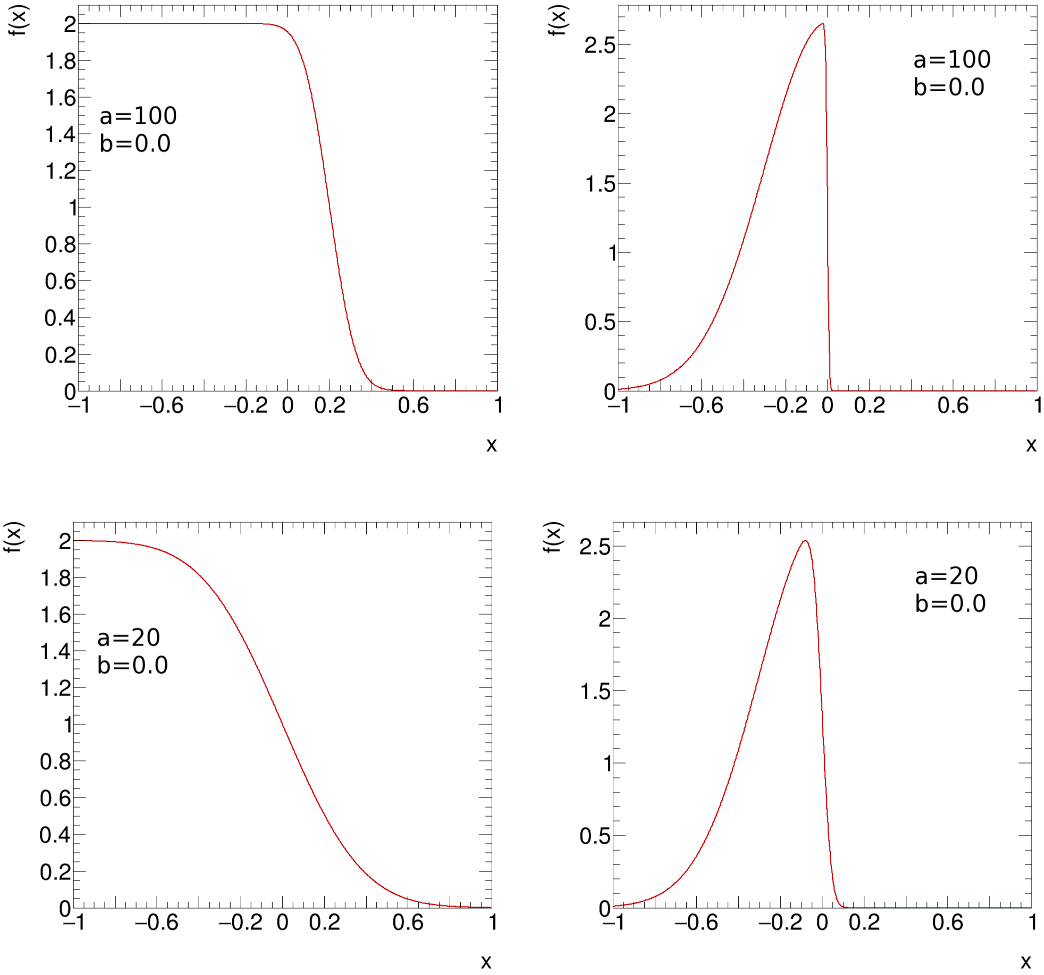

Figure 4.25: A Gaussian distribution ($\sigma = 0.1$, $\mu = 0$) convoluted (left) or multiplied (right) with the variation h(x) of the error function.

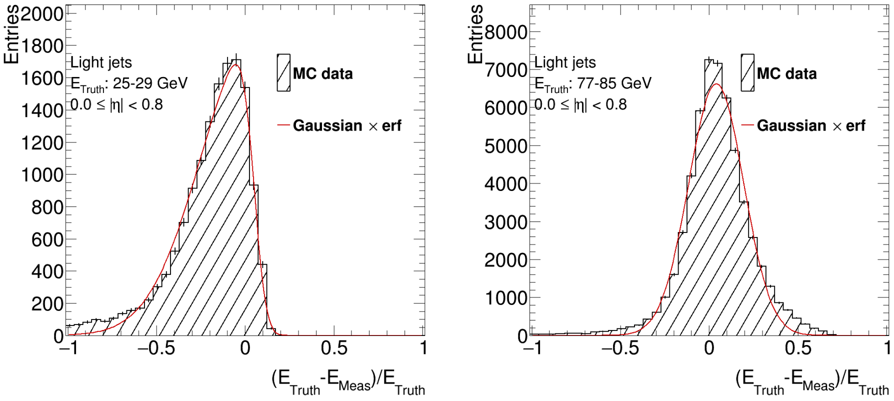

(a) Low energetic light jets (b) Medium energetic light jets

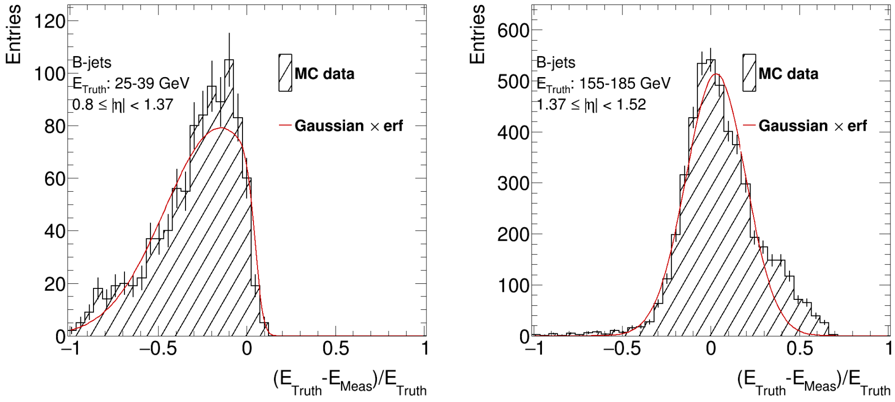

(c) Low energetic b-jets (d) High energetic b-jets

Figure 4.26: Fitted multiplication of a Gaussian distribution and an error function to acknowledge the edge observed in the Δ E spectra. The upper bound is allowed to be varied within the fit.

Fragmentation and Convolution For the neutrinos being produced inside of b-jets, the Peterson fragmentation provides an analytical expression of the unmeasured energy as discussed in Section 4.3.5.

During the development and the implementation of the underlying physics in TFTool it was recognised that there are computational problems. These are worth being discussed since they are directly related to future developments of TFTool and hence to the development of the transfer function.

TFTool uses BAT as underlying statistical tool. During all the studies BAT 0.9.2 was used since this is the default version that was used during the development of TFTool. By default, Root 5.34.25 provides all necessary libraries for BAT 0.9.2.

In order to respect each of the effects observed, a convolution of the analytic description is needed. This guarantees that all effects are considered in the correct way. For the functions used there is no analytical expression of the convolution. The TF1Convolution packages provides an algorithm to calculate convolutions within Root. The general idea of a numerical convolution is based on numerical integrals. In addition, the products of the two convoluted functions need to be evaluated after each integration step.

The TF1Convolution package is only provided after Root 6.04.02. Since Root 6 onwards is not supported by BAT 0.9.2, BAT 0.9.4 or higher needs to be used. In the development of more recent BAT versions, internal references and classes have been changed that are used in and required by TFTool. Hence, the versions are not compatible at the current stage and require major changes in TFTool. An overview of this issue is given in Table 4.4.

To test TF1Convolution in combination with TFTool, the package was manually reimplemented. By carefully disabling some functionalities and safety procedures used by the package, it is used together with Root 5.34 and hence in the current setup. In principle this version of TF1Convolution can be used in a newer version of TFTool even though an upgrade to Root 6 should be preferable to provide the full functionality.

With these changes it was possible to calculate convolutions of the Peterson fragmentation function and the Gaussian central spectrum that can now be used to fit the spectra

Unfortunately, the fitting function is called up to 20000 times for each histogram. The convolution needs to be evaluated in every of these calls again in order to provide a result for a given fitting step. This results in a massive slow down of the machine eventually resulting in a termination of the fitting process by the operating system. In further developments of TFTool the implementation of convolutions is therefore one of the major tasks.

The fitting procedure is only finished for very few histograms in some limited cases where

Table 4.4: An overview of the versions used within TFTool and the conflicts that arise between them.

BAT	Root	Comment
0.92	5.34	Default
	6.04 onward	Not supported by BAT
0.94(.1)	5.34	no TF1Convolution
	6.04 onward	Not supported by BAT
1.00	5.34	no TF1Convolution
	6.04 onward	Not supported by BAT

only two histograms in one $|\eta|$ region are considered. These requirements make it possible to validate if at least if the fitting procedure worked.

Figure 4.27(a) shows one example of a fit in case of a b-jet. It is compared with Figure 4.27(b) where the tuning and the fit is performed independently of TFTool. Even though the output from TFTool looks like an unconvoluted Gaussian distribution, the external fit yields the required shape. This shows that studying the parameters can help to improve the fit quality even though no optimal result was achieved. Within TFTool, it is rather complicated to study the parameters due to the instability of the fitting procedure. Since the parameters change from histogram to histogram it is not guaranteed that the fitting procedure is capable of fitting all histograms if the starting parameters and the boundaries have been tuned on one specific histogram. The fit uses an additional free parameter for the normalisation.

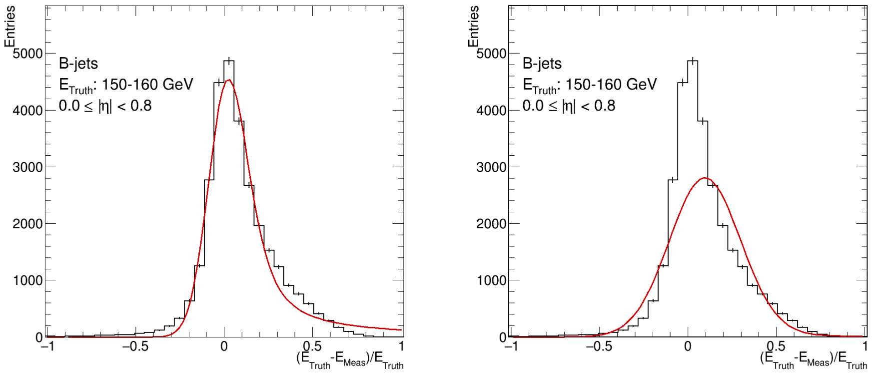

(a) Manual fit result.

(b) TFTool fit result.

Figure 4.27: One example for the local fit result in TFTool using a convolution of a Peterson function and a Gaussian distribution. It is compared to the fit result where the parameter limits have been manually tuned and fitted outside of TFTool.

Alternatives Since at the current stage the implementation of a convolution does not deliver the desired result, alternatives have been studied in parallel. These alternatives do not represent the physical motivation that was studied before but can describe the shape quite well. To study whether a function is able to describe the underlying physics a convolution of the Peterson fragmentation function (Equation 2.16) and a Gaussian distribution is formed. For eleven different sets of parameters, random numbers according to the convolution have been generated ten thousand times. The parameters that have been varied between the different simulations are the width σ of the Gaussian and the hardness ϵ of the Peterson fragmentation. The mean of the Gaussian is set to zero which is in agreement with the observations made during these studies. The scale factor of the Peterson function and the Gaussian is set to unity in order to achieve a good agreement with the $\Delta\,\mathrm{E}$ spectra from the MC sample. With these variations the $\Delta\,\mathrm{E}$ spectrum is simulated by only assuming the energy losses due to neutrinos as an underlying effect. As a result, eleven histograms based on the physical motivated convolution are obtained. These can now be fitted by alternative functions to check whether a sufficient fit result is achieved. The tested functions are a double Gaussian (dG), defined in Section 4.3.1, a Crystal Ball function (CB) [90, 91], defined as

$$\begin{aligned}
\mathrm{CB}(x;\alpha,n,\bar{x},\sigma) &= N\cdot\begin{cases}\exp(-\frac{(x-\bar{x})^2}{2\sigma^2}), & \text{for } \frac{x-\bar{x}}{\sigma} > -\alpha\\ A\cdot(B-\frac{x-\bar{x}}{\sigma})^{-n}, & \text{for } \frac{x-\bar{x}}{\sigma} \leqslant -\alpha\end{cases}\\
A &= \left(\frac{n}{|\alpha|}\right)^n\cdot\exp\left(-\frac{|\alpha|^2}{2}\right)\\
B &= \frac{n}{|\alpha|}-|\alpha|\\
N &= \frac{1}{\sigma(C+D)}\\
C &= \frac{n}{|\alpha|}\cdot\frac{1}{n-1}\cdot\exp\left(-\frac{|\alpha|^2}{2}\right)\\
D &= \sqrt{\frac{\pi}{2}}\left(1+\operatorname{erf}\left(\frac{|\alpha|}{\sqrt{2}}\right)\right)
\end{aligned} \tag{4.23}$$

and a convolution of a Gaussian and a Landau function (LanGau) where the Landau is given by the approximation

$$p(x) = \frac{1}{2\pi i}\int_{c-i\infty}^{c+i\infty} e^{s\log s+xs}\,ds \tag{4.24}$$

$$\approx \frac{1}{\sqrt{2\pi}}\exp\left\{-\frac{1}{2}(x+e^{-x})\right\}. \tag{4.25}$$

The scaling for the fit function is fixed based on the integral over the range of the histogram. Figure 4.28 shows three examples for the three fit functions considered. The results of all eleven fits are shown in Table 4.5. Overall, it can be concluded that the LanGau performs best in most of the cases. The double Gaussian fit delivers the second best overall result. In particular for small values of σ the tails are modelled quite well. The Crystal Ball Function is not capable of describing some of the tails in the examples presented. This shows that the physical motivation can also be described by alternative function of which the implementation is capable of performing actual fits.

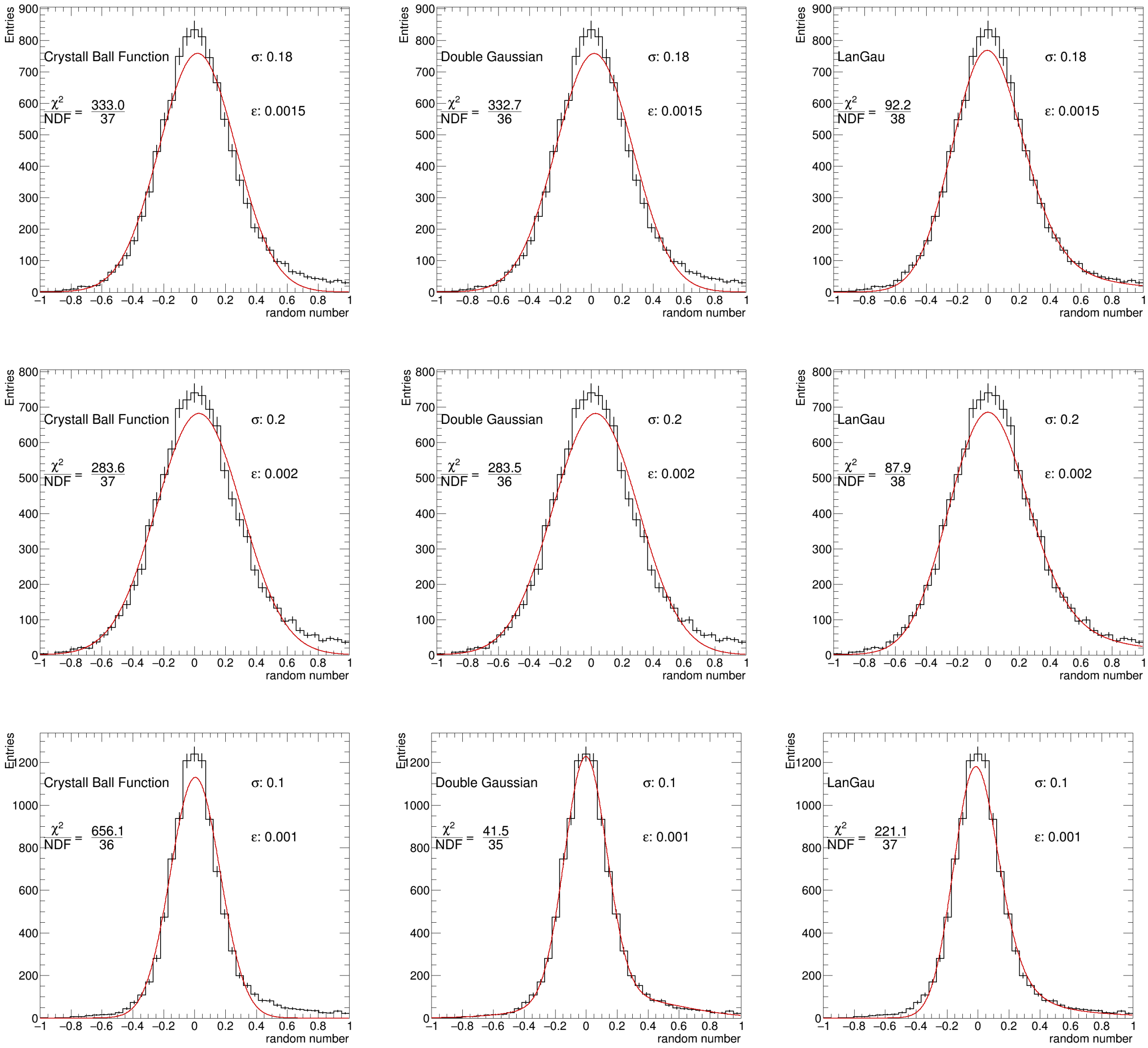

Figure 4.28: Alternative fits to the spectra generated by a convolution of the Peterson fragmentation function and a Gaussian.

Table 4.5: Results of the alternative fits to a spectrum generated with random numbers according to a convolution of a Gaussian and a Peterson function.

σ / ϵ	Fit Function	χ^2	NDF	$\frac{\chi^2}{\mathrm{NDF}}$
0.18 / 0.0015	CBF	333.0	37	8.9
	Double Gaussian	332.7	36	9.2
	LanGau	92.2	38	2.4
0.18 / 0.0010	CBF	324.2	37	8.8
	Double Gaussian	323.9	36	9.0
	LanGau	95.2	38	2.5
0.18 / 0.0020	CBF	360.4	37	9.7
	Double Gaussian	360.1	36	10.0
	LanGau	110.6	38	2.9
0.18 / 0.0030	CBF	352.3	37	9.5
	Double Gaussian	352.1	36	9.8
	LanGau	110.0	38	2.9
0.18 / 0.0005	CBF	262.0	37	7.1
	DoubleGaussian	261.7	36	7.3
	LanGau	80.9	38	2.1
0.15 / 0.0015	CBF	470.8	37	12.7
	Double Gaussian	50.1	36	1.4
	LanGau	144.9	38	3.8
0.10 / 0.0015	CBF	698.6	36	19.4
	Double Gaussian	39.7	35	1.1
	LanGau	3212	37	86.8
0.05 / 0.0015	CBF	1035.2	36	28.7
	Double Gaussian	70.1	35	2.0
	LanGau	390.5	37	10.6
0.20 / 0.0015	CBF	282.8	37	7.6
	Double Gaussian	282.6	36	7.9
	LanGau	81.7	38	2.2
0.20 / 0.0020	CBF	283.6	37	7.7
	Double Gaussian	283.5	36	7.9
	LanGau	87.9	38	2.3
0.10 / 0.0010	CBF	656.1	36	18.2
	Double Gaussian	41.5	35	1.2
	LanGau	221.2	37	6.0

4.3.7 Electrons and Muons

Within this thesis, no explicit studies for electrons and muons have been performed. However, some considerations can still be made based on the knowledge gained by studying jets. Examples for the $\Delta\,\mathrm{E}$ spectra that are used within TFTool are shown in Figure 4.29.

First of all, the observed spectra are narrower than for jets. Typical values of the width $\sigma(\Delta\,\mathrm{E})$ for a Gaussian fitted in the central region are in the order of $\sigma(\Delta\,\mathrm{E}) \approx 0.04$, whereas for jets $\sigma(\Delta\,\mathrm{E}) \approx 0.18$ is typical at $\mathrm{E}_{\mathrm{Truth}} \approx 200\,\mathrm{GeV}$. For muons $\sigma \approx 0.05$ is typical at $\mathrm{p}_{\mathrm{T,Truth}} = 200\,\mathrm{GeV}$. This is a direct consequence of the better energy resolution for electrons as shown in Equation 3.5 and muons ($\frac{\sigma_{p_\mathrm{T}}}{p_\mathrm{T}^2} \approx 2\%$ [92]) compared to jets.

Secondly, no edge in the histograms is observed at low energy- or p_T-values respectively. For muons, this is clear since they are classified by p_T and hence no geometry related energy cut needs to be considered.

For electrons, the $|\eta|$-dependent cut is still expected since the energy is measured in the electromagnetic calorimeter. The fact that an edge is not observed in the histograms can be explained by looking at the energy binning of the histograms. Table 4.6 compares the first energy bin that was generated by the binning procedure of TFTool with the lowest $\mathrm{E}_{\mathrm{cut}}$-value in each $|\eta|$ region. $\mathrm{E}_{\mathrm{cut}}$ was calculated according to Formula 4.9 for a $\mathrm{p}_\mathrm{T} > 25\,\mathrm{GeV}$ cut.

The table shows that the minimum energy bin is always above the energy cut-value. This is not the case for jets where a significant number of histograms has an energy bin below $\mathrm{E}_{\mathrm{cut}}$ (see Figure 4.14). This is a consequence of the better resolution for electrons which corresponds to smaller deviations from $\mathrm{E}_{\mathrm{Truth}}$ on average. As shown in Figure 4.29 higher values of $|\Delta\,\mathrm{E}|$ are 0.1-0.15 in the case of electrons and muons, whereas for jets $|\Delta\,\mathrm{E}| >> 0.15$ is often the case as shown in Figure 4.8.

For energy regions above $\mathrm{E}_{\mathrm{cut}}$, on average, the energy of electrons is not underestimated enough to fail the p_T-cut. In energy regions below $\mathrm{E}_{\mathrm{cut}}$ electrons are on average not overestimated enough to not pass the $|\eta|$-dependent p_T-cut.

Hence, histograms where an edge would be visible do not have enough statistics to be used within TFTool and histograms above $\mathrm{E}_{\mathrm{cut}}$ do not show an edge.

Thirdly, the underlying effects that lead to unmeasured energy are different between electrons, muons and jets. Both leptons are produced by the decay of a W-boson. Fragmentation is not involved in this process and does not have to be considered for leptons. For electrons, Bremsstrahlung needs to be considered as a significant energy loss, whereas for muons the main energy loss in the detector is ionisation which is expected to be small (see Bethe-Bloch formula in e.g. [12]).

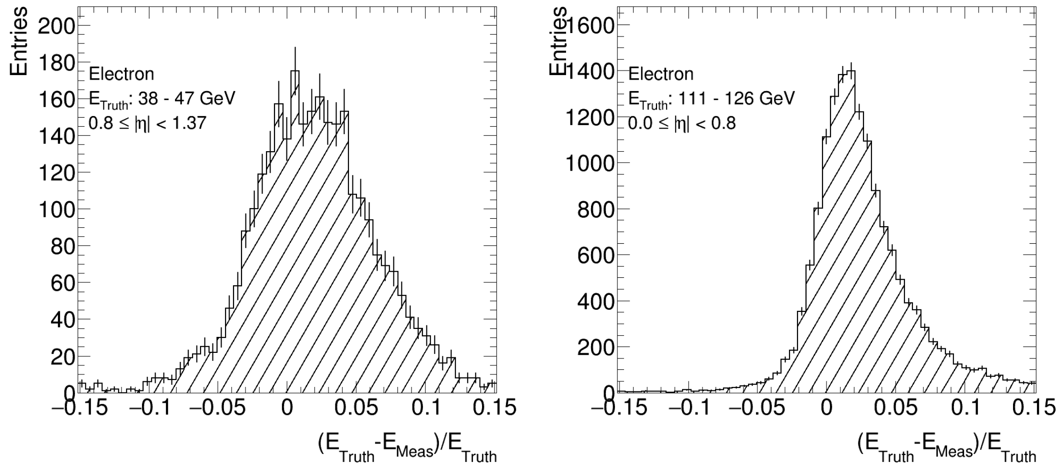

(a) Low energetic electron (b) Medium energetic electron

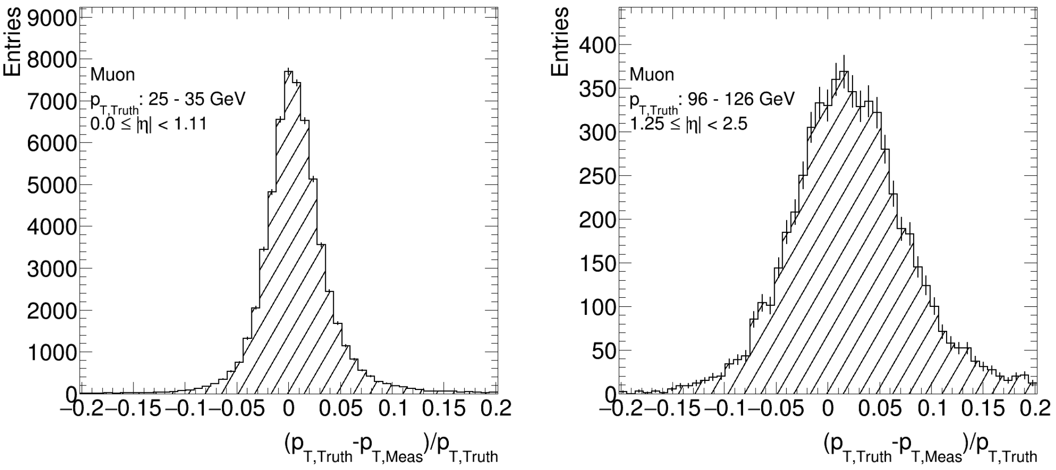

(c) Low energetic muon (d) Medium energetic muon

Figure 4.29: Examples for the Δ E spectra from TFTool for electrons and muons.

Table 4.6: Comparison of the $|\eta|$-dependent energy cut and the minimum energy bin for all four $|\eta|$-regions in the case of electrons.

$\|\eta\|$	E_{cut} [GeV]	Lowest energy bin [GeV]
0.0	25.0	(28,37)
0.8	33.3	(38,47)
1.37	51.8	(100,130)
1.52	59.2	(67,80)

5 Conclusion and Outlook

In the previous chapters it was demonstrated that, although KLFitter proved itself in the past to be a successful tool in top-quark physics, its performance is limited by the event selection. The main issue is the usage of additional jets that do not originate from a $t\bar{t}$-decay. Acceptance cuts were found to be the reason why an additional jet not belonging to the decay is used in the likelihood calculation. KLFitter needs four jets to form the likelihood since otherwise no constraints on the top-quark and W-boson masses can be made. As a consequence, in the case that one of the correct jets does not pass the cut criteria, an additional jet is automatically selected. This results in 50% of events having not all jets labelled as present.

Additionally, it was shown that jet merging plays an important role for boosted events. A likelihood based on three jets would avoid the problem of one missing jet.

By introducing a likelihood cut on selected events, the percentage of events with a falsely selected jet can be reduced. Still, the shape of the likelihood for events where all jets are present and events where not all jets are present is similar and no perfect separation can be achieved.

Furthermore, the development of new transfer functions for the 13 TeV run was presented. The shift of the mean value in the $\Delta\,\mathrm{E}$ spectrum at low energies occuring together with an upper bound is caused by $\mathrm{p_T}$-cuts in the reconstruction. Due to the geometrical relation, given in Equation 4.9, this effect vanishes for higher $\mathrm{E_{Truth}}$ bins. The exact behaviour depends on the $|\eta|$ region and the type of jet considered. With this knowledge, first steps for an analytical implementation in the KLFitter package have been presented. It was shown that an upper bound can be implemented within TFTool by introducing additional $|\eta|$ regions. The $\mathrm{E_{Truth}}$ bin widths do not become too large and a sufficient number of histograms per $|\eta|$ region can be fitted.

Additionally, the tail for $\Delta\,E\ >0$ was discussed. Within a jet, neutrinos are produced in additional decays. The energy of the neutrino cannot be measured and therefore the energy of the jet is not fully reconstructed. The spectrum of the energy that is not measured can be described by fragmentation. This effect is stronger for higher generations of quarks due to decay chains of heavy hadrons into lighter ones. Within these decay chains, additional neutrinos occur.

The last part covered first steps for the implementation within TFTool. The main problem that was presented is the implementation of a convolution that can be used together with the fitting procedure on all histograms. At the current stage this procedure is too computationally intensive but is worth studying in more detail to provide well motivated Transfer Functions.

A Additional Content

A.1 Comparison of Quark Generations

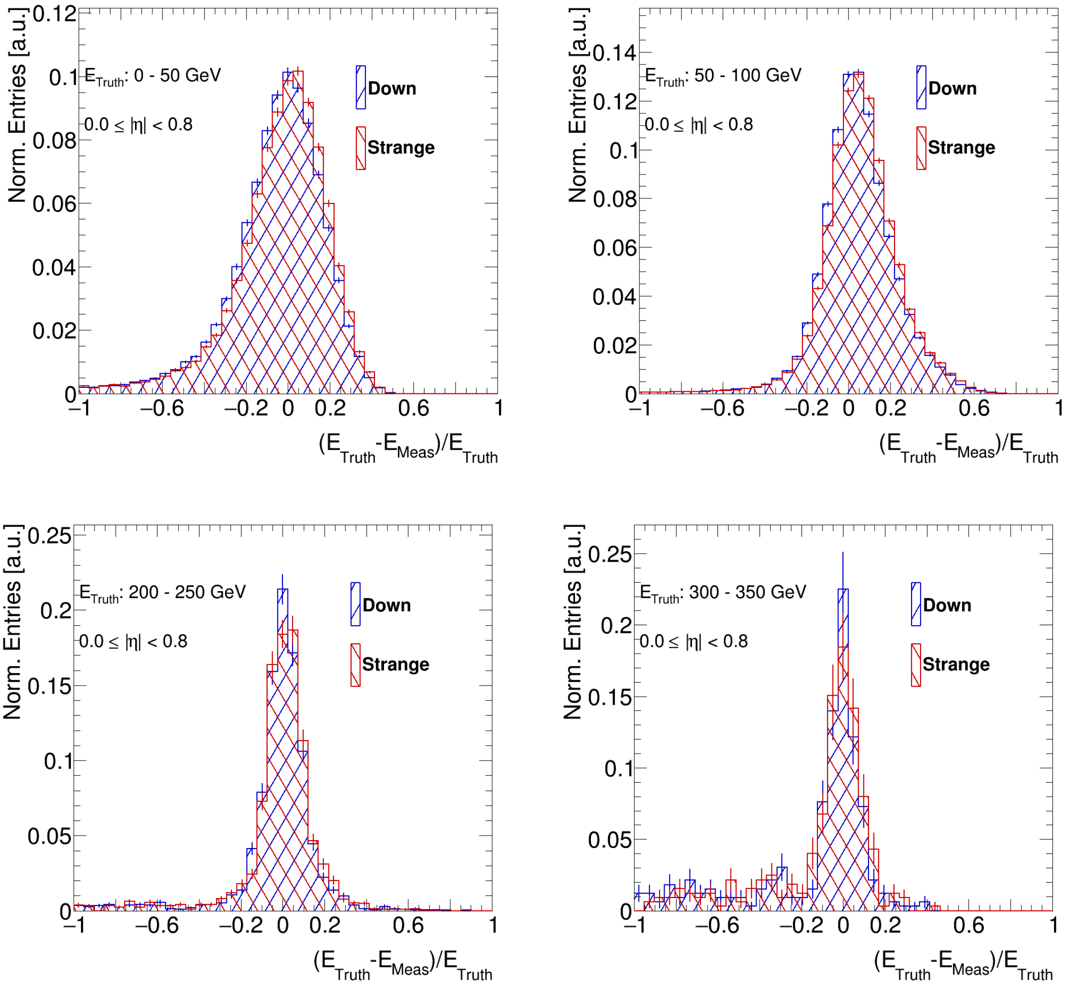

Figure A.1: Comparison of the ΔE spectra for the strange and down flavour in the central pseudorapidity region. E_{Truth} bins with a size of 50 GeV are shown.

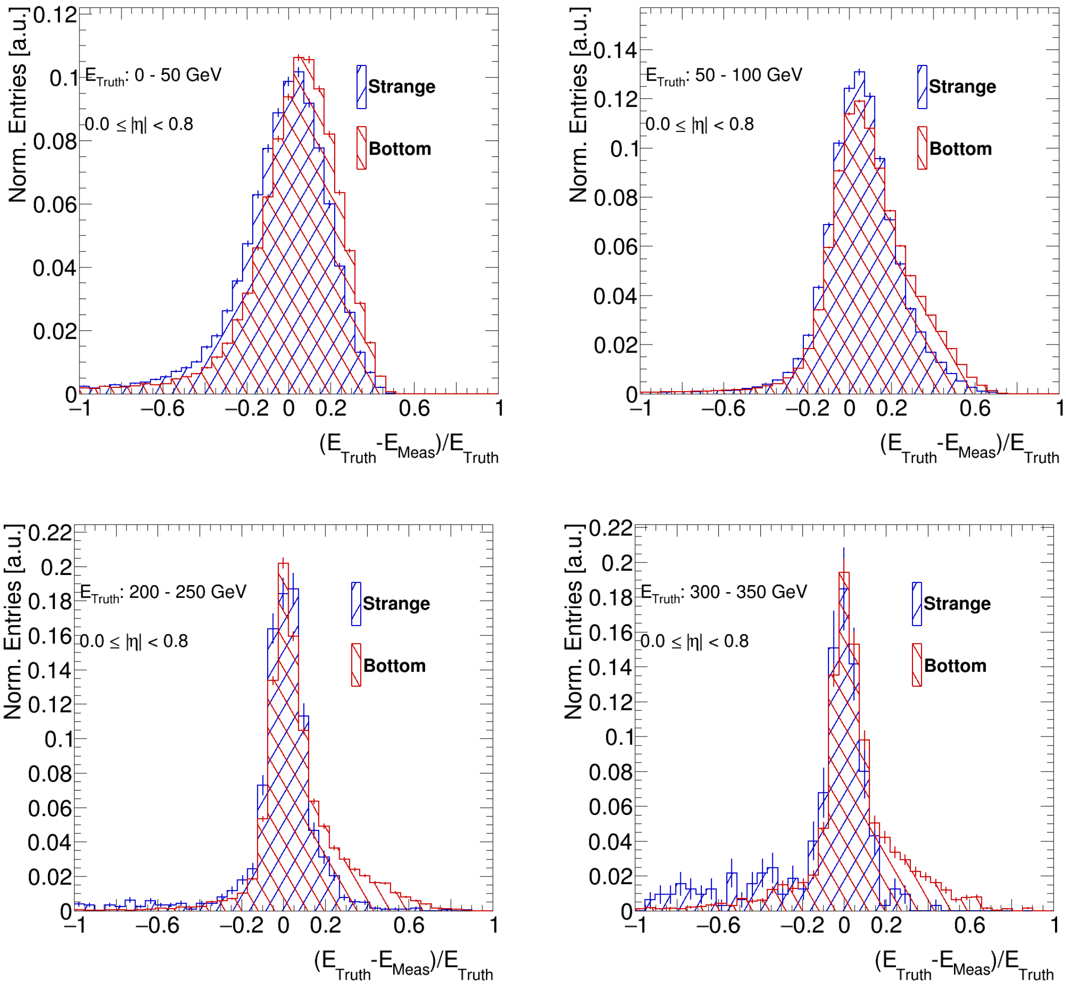

Figure A.2: Comparison of the Δ E spectra for the strange and bottom flavour in the central pseudorapidity region. E_{Truth} bins with a size of 50 GeV are shown.

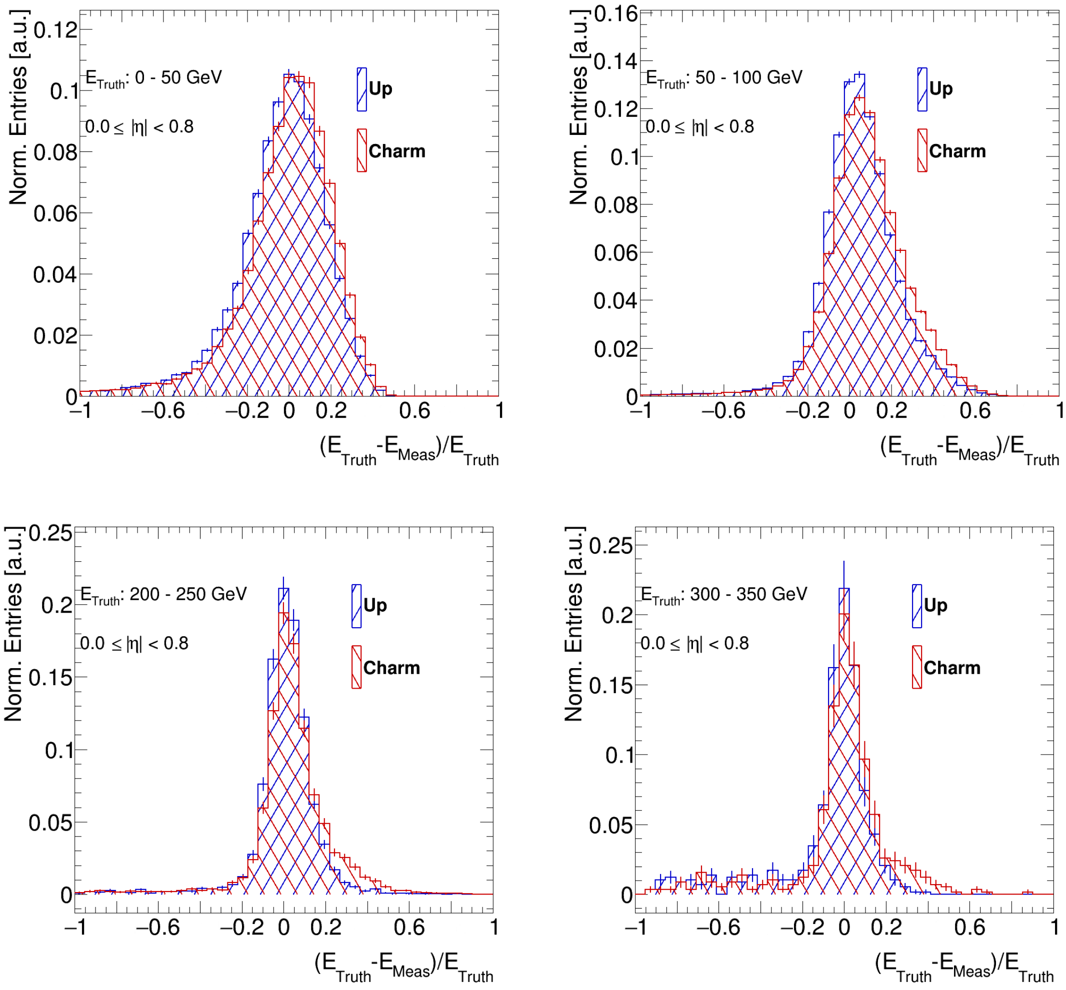

Figure A.3: Comparison of the Δ E spectra for the up and charm flavour in the central pseudorapidity region. E_{Truth} bins with a size of 50 GeV are shown.

A.2 Plots for B-Jet Comparison

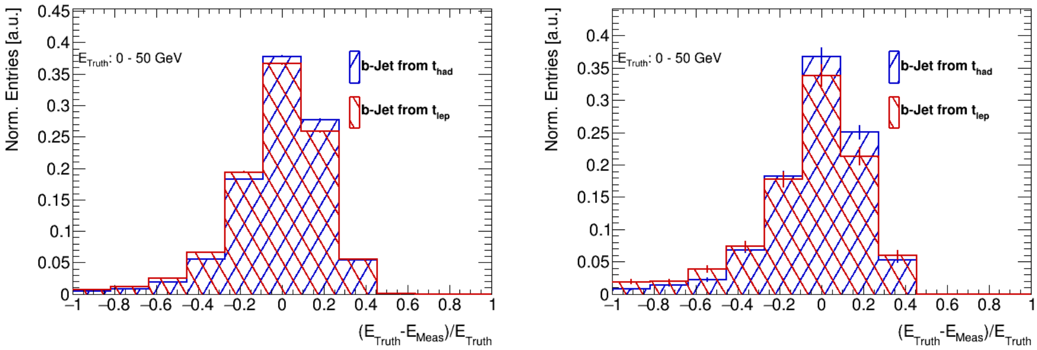

(a) Muon matched (b) Muon unmatched

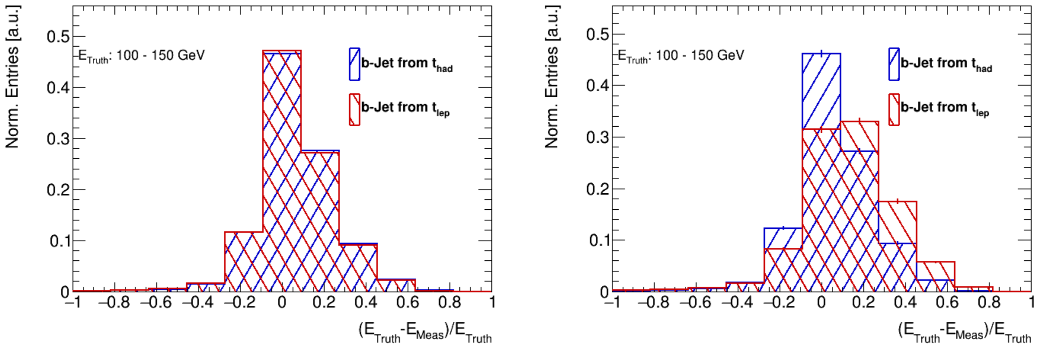

(c) Muon matched (d) Muon unmatched

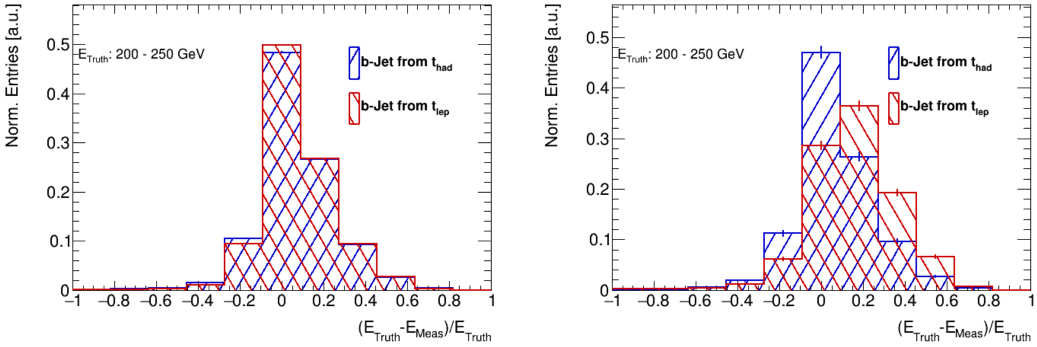

(e) Muon matched (f) Muon unmatched

Figure A.4: Comparison of the b-jets from the hadronic/leptonic decaying top-quark in different energy regions in the cases of no overlap between the muon and the jet. The bin errors are partly below the line width.

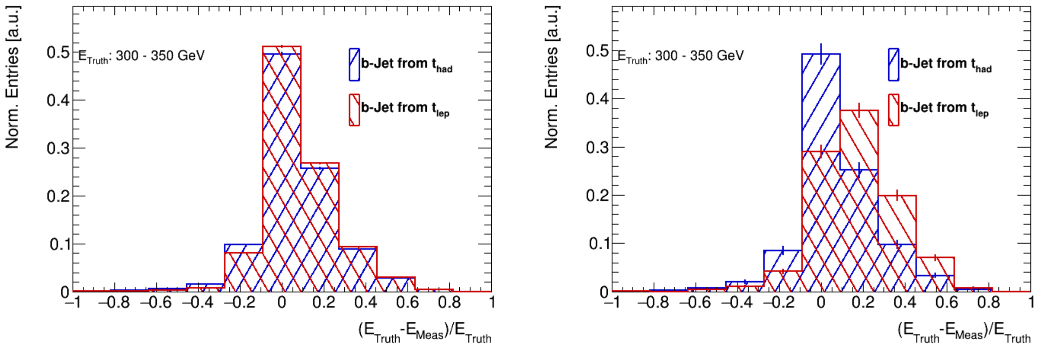

(a) Muon matched (b) Muon unmatched

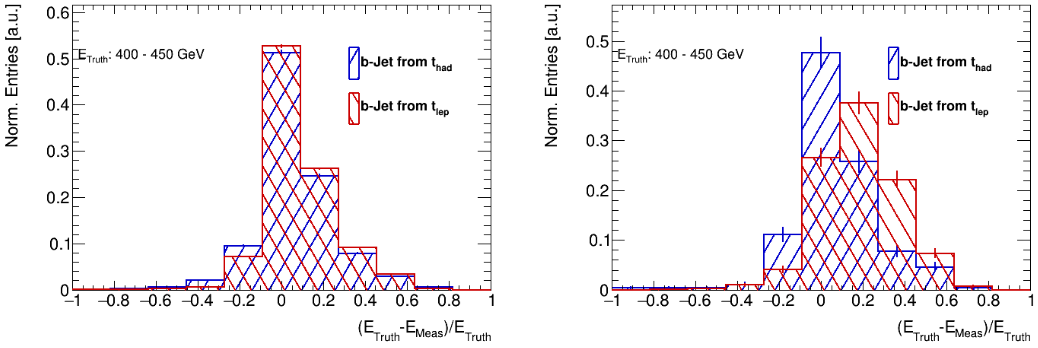

(c) Muon matched (d) Muon unmatched

Figure A.5: Comparison of the b-jets from the hadronic/leptonic decaying top-quark in different energy regions in the cases of no overlap between the muon and the jet. Partly the bin errors are below the line width.

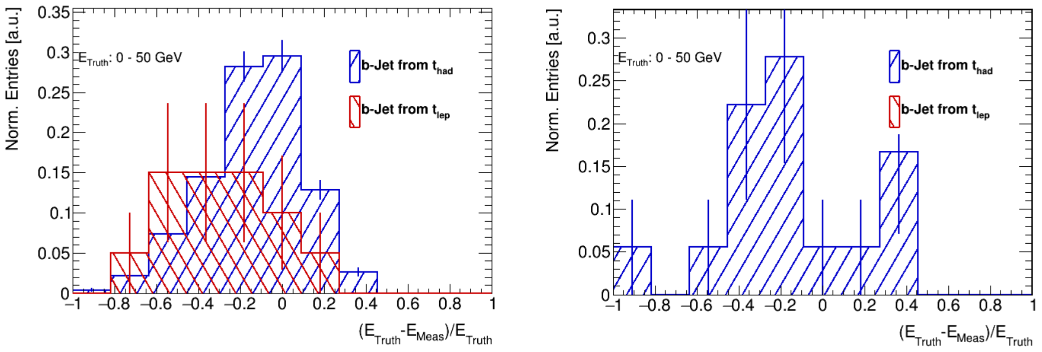

(a) Muon matched (b) Muon unmatched

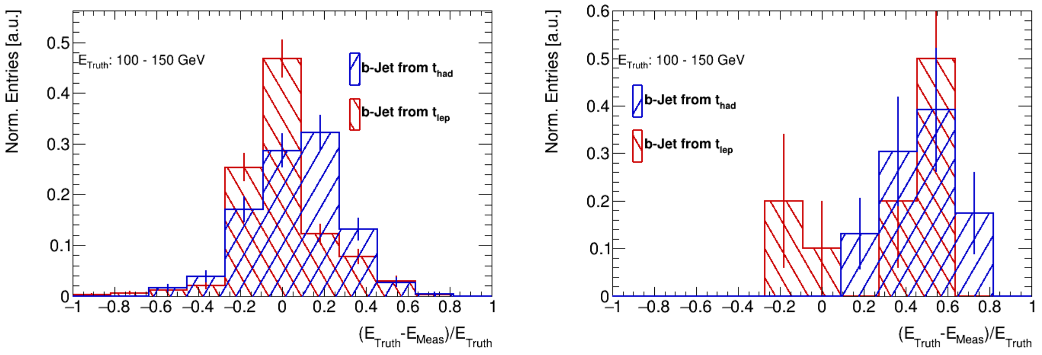

(c) Muon matched (d) Muon unmatched

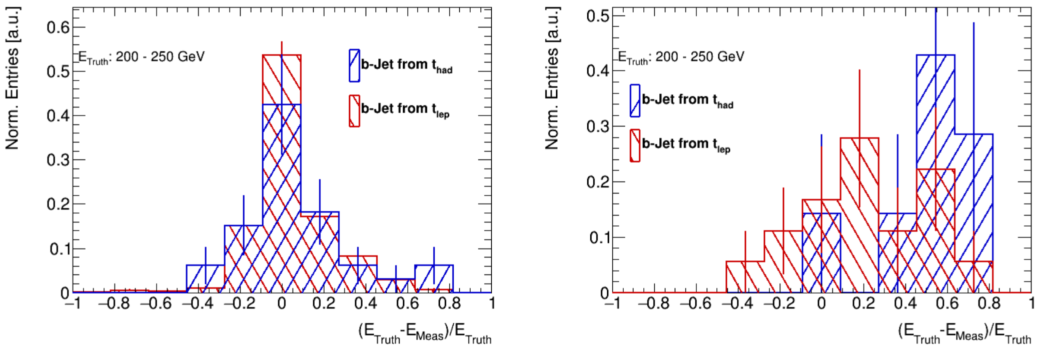

(e) Muon matched (f) Muon unmatched

Figure A.6: Comparison of the b-jets from the hadronic/leptonic decaying top-quark in different energy regions in the cases of an overlap between the muon and the jet. Partly the bin errors are below the line width.

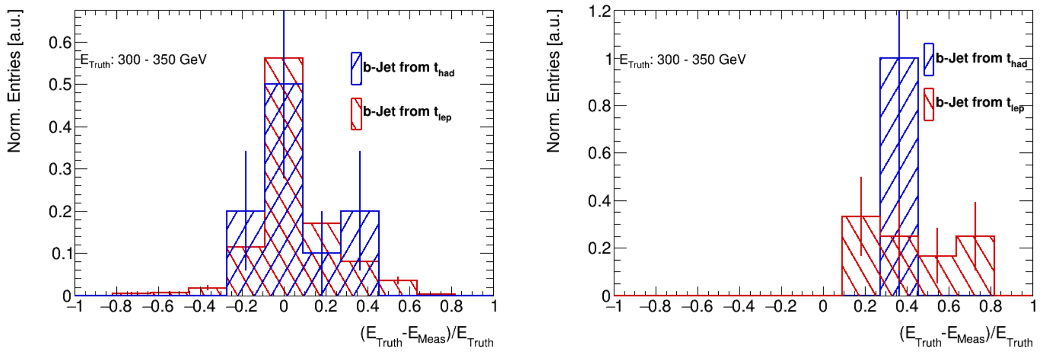

(a) Muon matched (b) Muon unmatched

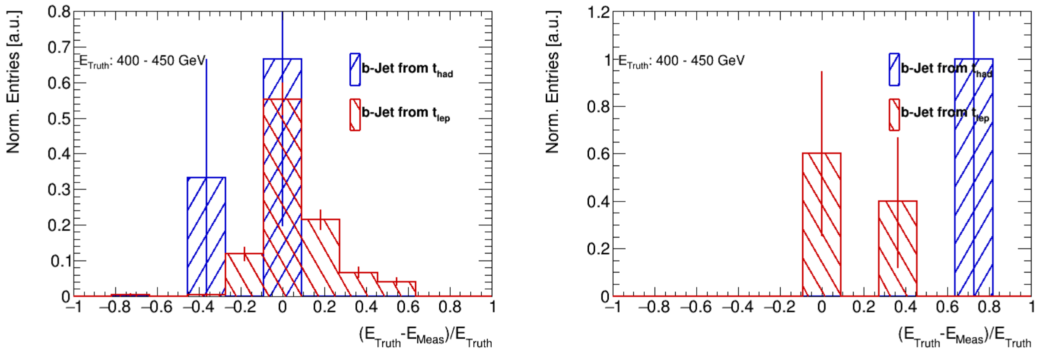

(c) Muon matched (d) Muon unmatched

Figure A.7: Comparison of the b-jets from the hadronic/leptonic decaying top-quark in different energy regions in the cases of an overlap between the muon and the jet. Partly the bin errors are below the line width.

A.3 Alternative Functions

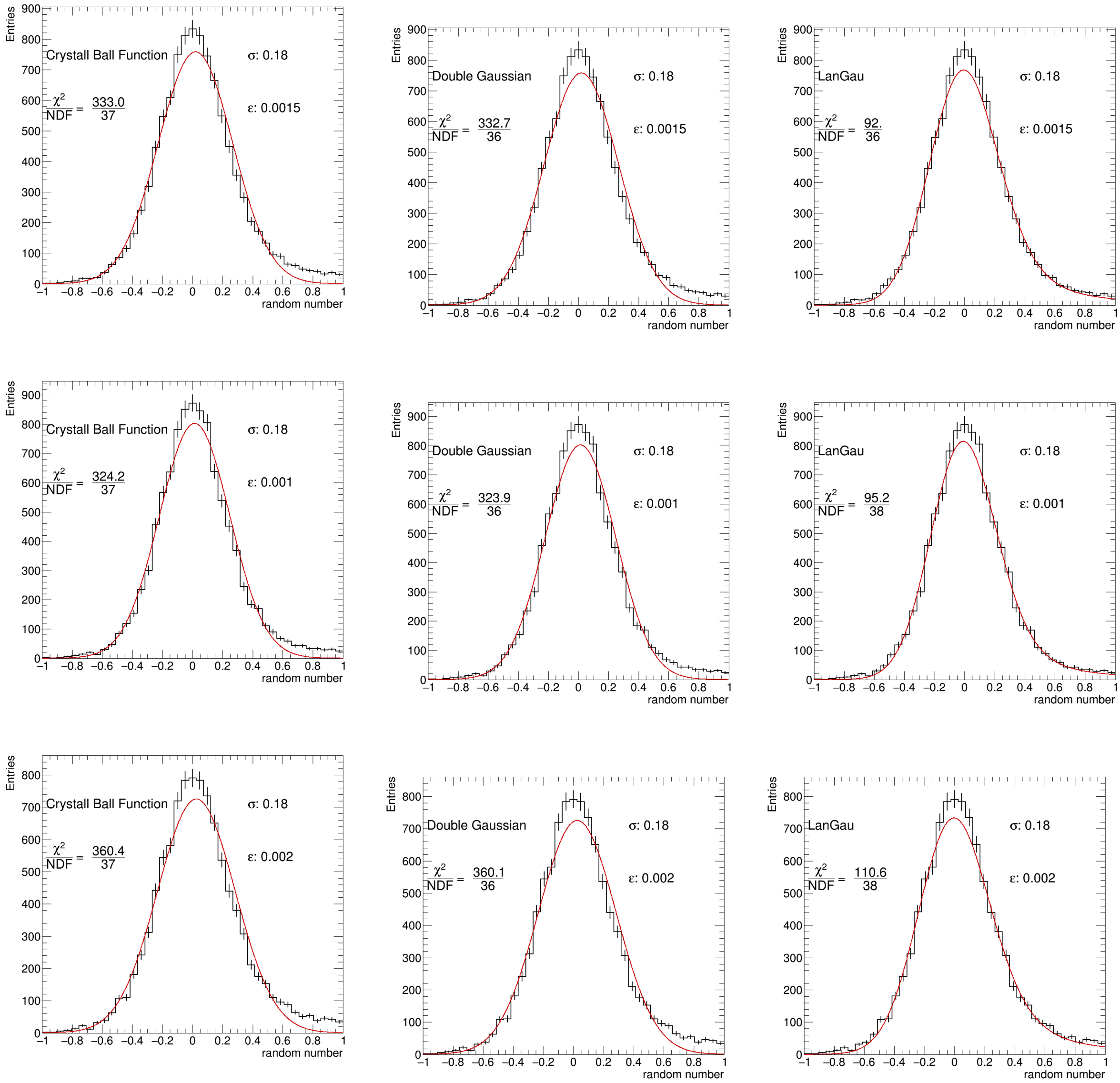

Figure A.8: Alternative fits to the spectra generated by a convolution of the Peterson fragmentation function and a Gaussian.

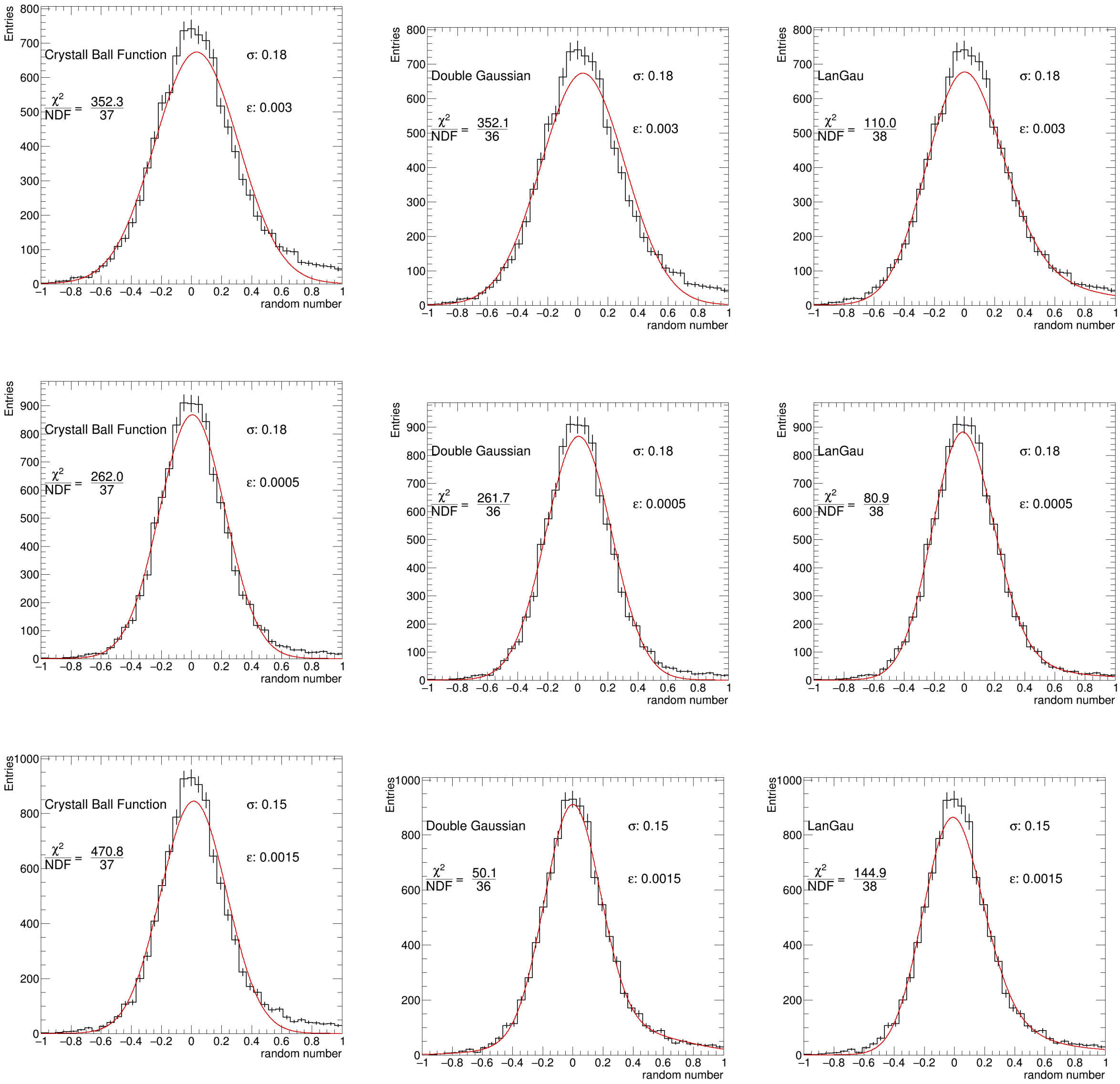

Figure A.9: Alternative fits to the spectra generated by a convolution of the Peterson fragmentation function and a Gaussian.

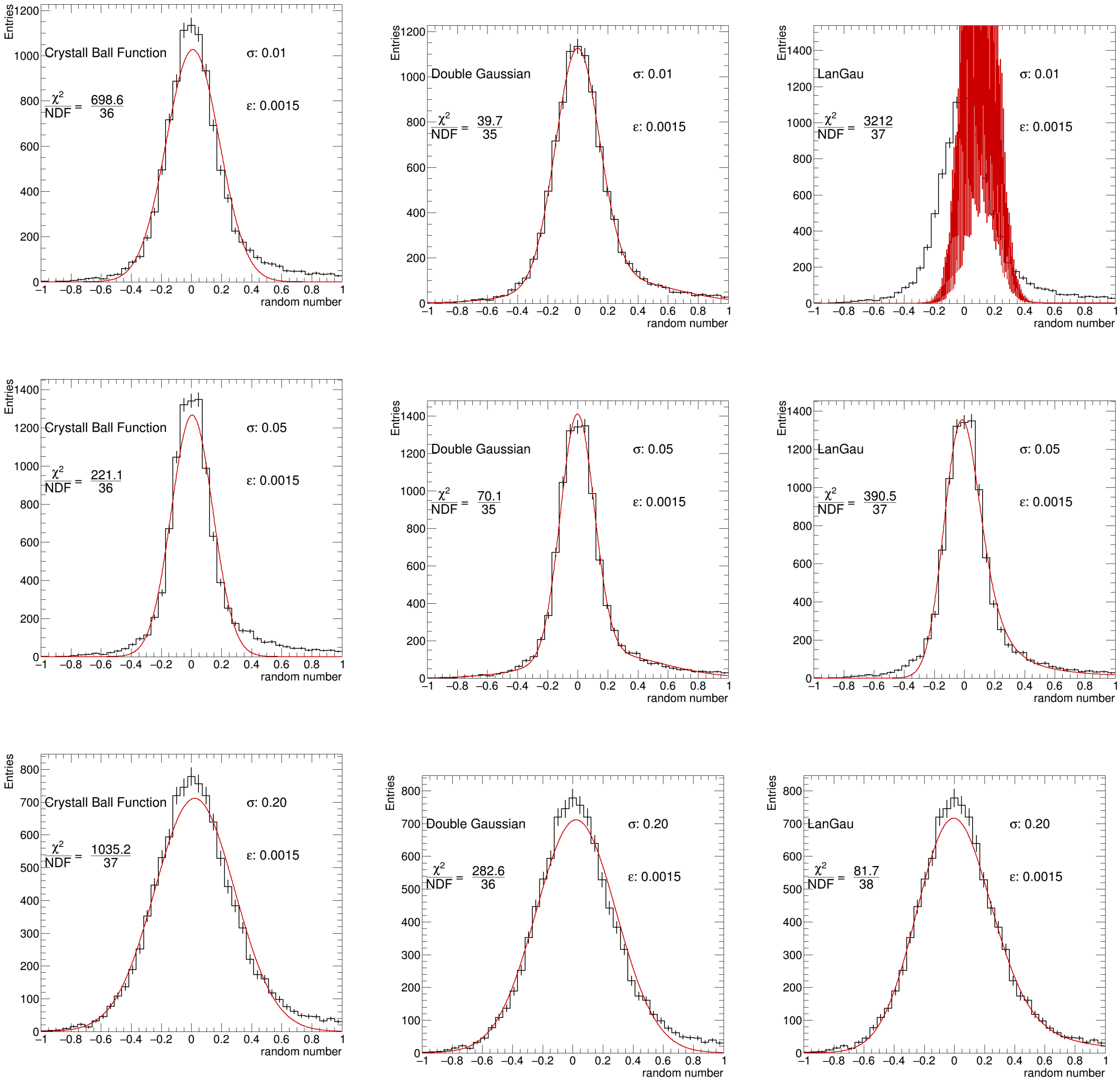

Figure A.10: Alternative fits to the spectra generated by a convolution of the Peterson fragmentation function and a Gaussian. The fit in the upper right corner failed.

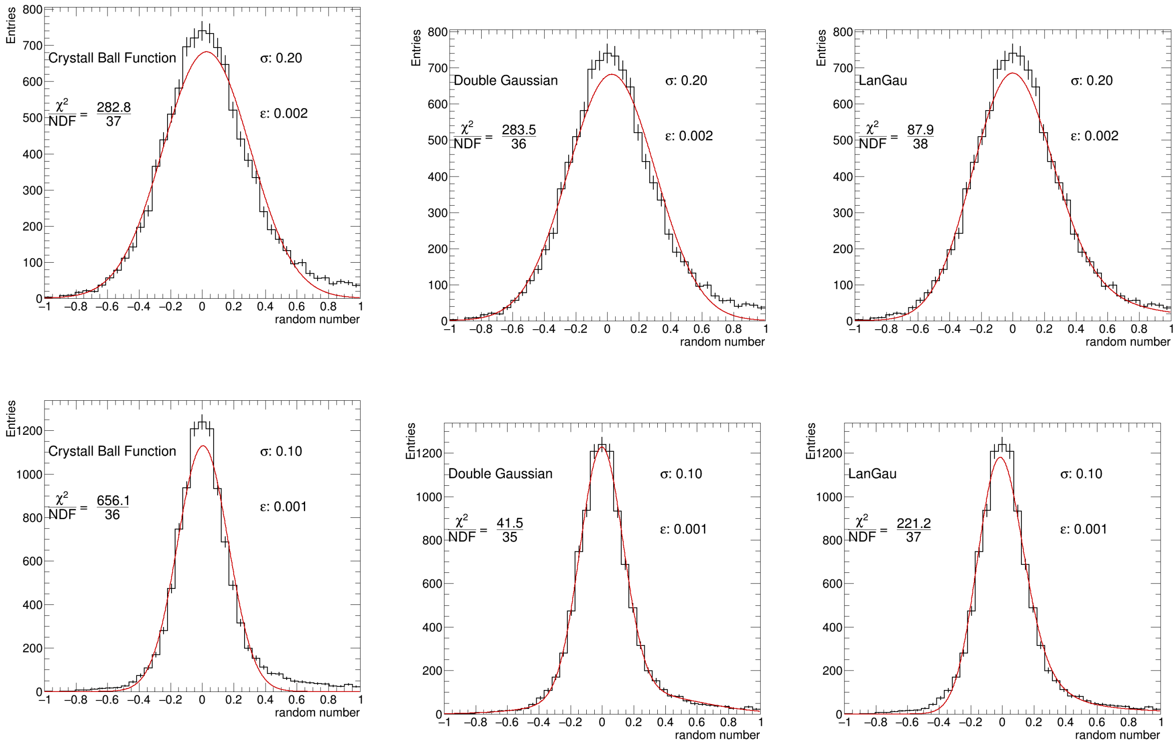

Figure A.11: Alternative fits to the spectra generated by a convolution of the Peterson fragmentation function and a Gaussian.

Bibliography

[1] J. Erdmann, et al., *A likelihood-based reconstruction algorithm for top-quark pairs and the KLFitter framework*, Nucl. Instr. Meth. Phys. Res. **748**, 18 (201)

[2] F. Abe, et al. (CDF Collaboration), *Observation of Top Quark Production in $p\bar{p}$ Collisions with the Collider Detector at Fermilab*, Phys. Rev. Lett. **74**, 2626 (1995)

[3] S. Abachi, et al. (DØ Collaboration), *Observation of the Top Quark*, Phys. Rev. Lett. **74**, 2632 (1995)

[4] S. Chatrchyan, et al., *Observation of a new boson at a mass of 125 GeV with the CMS experiment at the LHC*, Phys.Lett. B **716(1)**, 30 (2012)

[5] G. Aad, et al. (ATLAS Collaboration), *Observation of a new particle in the search for the Standard Model Higgs boson with the ATLAS detector at the LHC*, Phys. Lett. **B716**, 1 (2012)

[6] P. W. Higgs, *Broken Symmetries, Massless Particles and Gauge Fields*, Phys. Lett. **12**, 132 (1964)

[7] F. Englert, R. Brout, *Broken Symmetry and the Mass of Gauge Vector Mesons*, Phys. Rev. Lett. **13**, 321 (1964)

[8] G. S. Guralnik, C. R. Hagen, T. W. B. Kibble, *Global Conservation Laws and Massless Particles*, Phys. Rev. Lett. **13**, 585 (1964)

[9] G. Bertone, D. Hooper, J. Silk, *Particle dark matter: evidence, candidates and constraints*, Phys. Rep. **405(5-6)**, 279 (2005)

[10] K. Hirata, et al., *Observation of a small atmospheric v_μ/v_e ratio in Kamiokande*, Phys.Lett. B **280(1)**, 146 (1992)

[11] B. Lemmer, *Measurement of Spin Correlations in $t\bar{t}$ Events from pp Collisions at $\sqrt{s} = 7$ TeV in the Lepton + Jets Final State with the ATLAS Detector* (2014), II.PHYSIK-UNIGÖ-DISS-2014-02

[12] C. Patrignani, et al. (Particle Data Group), *Review of Particle Physics*, Chin. Phys. **C40(10)**, 100001 (2016)

[13] S. L. Glashow, *Partial Symmetries of Weak Interactions*, Nucl. Phys. **22**, 579 (1961)

[14] S. Weinberg, *A Model of Leptons*, Phys. Rev. Lett. **19**, 1264 (1967)

[15] A. Salam, *Weak and Electromagnetic Interactions*, Almqvist & Wiksell, Stockholm, nobel symposium 8 edition (1968)

[16] C. S. Wu, et al., *Experimental Test of Parity Conservation in Beta Decay*, Phys. Rev. **105**, 1413 (1957)

[17] M. Goldhaber, L. Grodzins, A. W. Sunyar, *Helicity of Neutrinos*, Phys. Rev. **109**, 1015 (1958)

[18] B. Grinstein, S.-J. Rey, M. B. Wise, *CP violation in charged-kaon decay*, Phys. Rev. D **33**, 1495 (1986)

[19] N. Cabbibo, *Unitary Symmetry and Leptonic Decays*, Phys. Rev. Lett. **10**, 531 (1963)

[20] M. Kobayashi, T. Maskawa, *CP Violation in the Renormalizable Theory of Weak Interaction*, Prog. Theor. Phys. **49**, 652 (1973)

[21] K. Massri (NA48/2), *Precision tests of the Standard Model with Kaon decays at CERN*, J. Phys. Conf. Ser. **631(1)**, 012040 (2015)

[22] H. D. Politzer, *Asymptotic Freedom: An Approach to Strong Interactions*, Phys. Rept. **14**, 129 (1974)

[23] D. J. Gross, F. Wilczek, *Asymptotically Free Gauge Theories*, Phys. Rev. D **8**, 3633 (1973)

[24] D. J. Gross, F. Wilczek, *Ultraviolet Behavior of Non-Abelian Gauge Theories*, Phs. Rev. Lett. **30**, 1343

[25] J. C. Collins, D. E. Soper, *The Theorems of Perturbative QCD*, Ann. Rev. Nucl. Part. Sci. **37**, 383 (1987)

[26] G. Altarelli, *Partons in Quantum Chromodynamics*, Phys. Rept. **81**, 1 (1982)

[27] F. Arleo, *(Medium-modified) Fragmentation Functions*, Eur. Phys. J. **C61**, 603 (2009)

[28] G. Bocquet, et al., *Transverse momentum spectra of charged particles in pp collisions at* $\sqrt{s}$*=630 GeV*, Phys. Lett. B **366(1)**, 434 (1996)

[29] C. Peterson, et al., *Scaling violations in inclusive* e^+e^- *annihilation spectra*, Phys. Rev. D **27**, 105 (1983)

[30] H. Albrecht, et al., *Inclusive production of D0, D+ and D*(2010)+ mesons in B decays and nonresonant e+ e- annihilation at 10.6 GeV*, Z. Phys. **52(3)**, 353 (1991)

[31] R. Akers, et al. (OPAL), *A Measurement of the production of* $D^{*\pm}$ *mesons on the* Z^0 *resonance*, Z. Phys. **C67**, 27 (1995)

[32] D. Buskulic, et al. (ALEPH), *Measurement of the effective b quark fragmentation function at the Z resonance*, Phys. Lett. **B357**, 699 (1995)

[33] J. H. Christenson, et al., *Evidence for the* 2π *Decay of the* K_2^0 *Meson*, Phys. Rev. Lett. **13**, 138 (1964)

[34] M. L. Perl, et al., *Evidence for Anomalous Lepton Production in* e^+-e^- *Annihilation*, Phys. Rev. Lett. **35**, 1489 (1975)

[35] S. W. Herb, et al., *Observation of a Dimuon Resonance at* 9.5 GeV *in* 400 GeV *Proton-Nucleus Collisions*, Phys. Rev. Lett. **39**, 252 (1977)

[36] S. L. Glashow, J. Iliopoulos, L. Maiani, *Weak Interactions with Lepton-Hadron Symmetry*, Phys. Rev. D **2**, 1285 (1970)

[37] H. Georgi, S. Glashow, *Making do without the t quark*, Nucl.Phys. B **167(1)**, 173 (1980)

[38] G. L. Kane, M. E. Peskin, *A Constraint from B Decay on Models with no t Quark*, Nucl. Phys. B **195**, 29 (1982)

[39] H. Georgi, A. Pais, *Generalization of the Glashow-Iliopoulos-Maiani mechanism: Horizontal and vertical flavor mixing*, Phys. Rev. D **19**, 2746 (1979)

[40] F. Gürsey, P. Ramond, P. Sikivie, *A universal gauge theory model based on E6*, Phys.Lett. B **60(2)**, 177 (1976)

[41] A. Bean, et al. (CLEO), *Improved Upper Limit on Flavor Changing Neutral-Current Decays of the b Quark*, Phys. Rev. D **35**, 3533 (1987)

[42] G. 't Hooft, M. Veltmann, *Regularization And Renormalization Of Gauge Fields*, Nucl. Phys. B **44**, 189 (1972)

[43] LEP-Electroweak Working Group and the LEP Collaborations: ALEPH, DELPHI, L3 and OPAL, *Electroweak Parameters of the Z^0 Resonance and the Standard Model*, Phys. Lett. B **276**, 247 (1992)

[44] V. M. Abazov, et al. (DØ Collaboration), *Experimental discrimination between charge 2e/3 top quark and charge 4e/3 exotic quark production scenarios*, Phys. Rev. Lett. **98** (2007)

[45] T. Aaltonen, et al. (CDF Collaboration), *Exclusion of an Exotic Top Quark with* $-4/3$ *Electric Charge Using Soft Lepton Tagging*, Phys. Rev. Lett. **105**, 101801 (2010)

[46] G. Aad, et al. (ATLAS Collaboration), *Measurements of spin correlation in top-antitop quark events from proton-proton collisions at* $\sqrt{s} = 7$ *TeV using the ATLAS detector*, Phys. Rev. **D90(11)**, 112016 (2014)

[47] M. Aaboud, et al., *Measurement of the top quark mass in the* $t\bar{t} \rightarrow$*dilepton channel from* $\sqrt{s} = 8$ *TeV ATLAS data*, Phys.Lett. B **761**, 350 (2016)

[48] G. Breit, E. Wigner, *Capture of Slow Neutrons*, Phys. Rev. **49**, 519 (1936)

[49] A. R. Bohm, Y. Sato, *Relativistic resonances: Their masses, widths, lifetimes, superposition, and causal evolution*, Phys. Rev. D **71**, 085018 (2005)

[50] M. Jeżabek, J. H. Kühn, *QCD Corrections to Semileptonic Decays of Heavy Quarks*, Nucl. Phys. B **314**, 1 (1989)

[51] I. I. Y. Bigi, et al., *Production and decay properties of ultraheavy quarks*, Phys. Lett. B **181**, 157 (1986)

[52] J. C. Collins, D. E. Soper, G. Sterman, *Heavy Particle Production in High-Energy Hadron Collisions*, Nucl. Phys. B **263**, 37 (1986)

[53] The Durham HepData Project, *Online PDF plotting and calculation* [Online, accessed 23.03.2016], `hepdata.cedar.ac.uk/pdf/pdf3.html`

[54] *LHCTopWG Summary Plots* [Online, accessed 23.03.2017] `https://atlas.web.cern.ch/Atlas/GROUPS/PHYSICS/CombinedSummaryPlots/TOP/tt_xsec_vsroots/history.html`

[55] T. Stelzer, Z. Sullivan, S. Willenbrock, *Single Top Quark Production via W-Gluon Gusion at Next-to-Leading Order*, Phys. Rev. D **56**, 5919 (1997)

[56] T. Aaltonen, et al. (CDF Collaboration), *Observation of Electroweak Single Top-Quark Production*, Phys. Rev. Lett. **103**, 092002 (2009)

[57] V. M. Abazov, et al. (DØ Collaboration), *Observation of Single Top-Quark Production*, Phys. Rev. Lett. **103**, 092001 (2009)

[58] A. Giammanco, *Single top quark production at the LHC*, Rev.Phys. **1**, 1 (2016)

[59] H. P. Nilles, *Supersymmetry, supergravity and particle physics*, Phys. Rep. **110**, 1 (1984)

[60] H. E. Haber, G. L. Kane, *The search for supersymmetry: Probing physics beyond the standard model*, Phys. Rep. **117**, 75 (1985)

[61] J. F. Gunion, et al., *The Higgs Hunters Guide*, (Addison-Wesley, Redwood City, California, 1990)

[62] M. Carena, H. E. Haber, *Higgs Boson theory and phenomenology*, Prog. Part. Nucl. Phys. **50**, 63 (2003)

[63] J. Fleischer, F. Jegerlehner, O. V. Tarasov, *Two Loop Heavy Top Corrections to the Rho Parameter: A Simple Formula Valid for Arbitrary Higgs Mass*, Phys. Lett. B **319**, 249 (1993)

[64] Y. Qin (ATLAS), *Search for the Standard Model Higgs boson produced in association with top quarks with the ATLAS detector*, EPJ Web Conf., Proceedings, 4th International Conference on New Frontiers in Physics (ICNFP 2015): Kolymbari, Greece, August 23-30, 2015 **126** (2016)

[65] U. Baur, M. Buice, L. H. Orr, *Direct measurement of the top quark charge at hadron colliders*, Phys. Rev. D **64**, 094019 (2001)

[66] G. Aad, et al. (ATLAS), *Observation of top-quark pair production in association with a photon and measurement of the $t\bar{t}\gamma$ production cross section in pp collisions at $\sqrt{s} = 7$ TeV using the ATLAS detector*, Phys. Rev. **D91(7)** (2015)

[67] B. Lillie, J. Shu, T. M. Tait, *Top compositeness at the Tevatron and LHC*, JHEP **2008(04)**, 087 (2008)

[68] T. Aaltonen, et al. (CDF Collaboration), *Evidence for $t\bar{t}\gamma$ production and measurement of $\sigma_{t\bar{t}\gamma}/\sigma_{t\bar{t}}$*, Phys. Rev. D **84**, 031104 (2011)

[69] M. Aaboud, et al. (ATLAS), *Measurement of the $t\bar{t}Z$ and $t\bar{t}W$ production cross sections in multilepton final states using 3.2 fb^{-1} of pp collisions at $\sqrt{s}$ = 13 TeV with the ATLAS detector*, Eur. Phys. J. **C77(1)**, 40 (2017)

[70] *The Large Hadron Collider LHC at CERN*, http://lhc-new-homepage.web.cern.ch (2000)

[71] L. R. Evans, *The Large Hadron Collider (LHC)*, Eur. Phys. J. C **34**, S11 (2004)

[72] L. R. Evans, *Challenges of the LHC: The Accelerator Challenge*, Eur. Phys. J. C **34**, 57 (2004)

[73] L. R. Evans, *The Large Hadron Collider (LHC)*, IEEE Trans. Appl. Supercond. **14**, 147 (2004)

[74] A. Airapetian, et al. (ATLAS Collaboration), *ATLAS: Detector and physics performance technical design report. Volume 1* (1999)

[75] E. Halkiadakis, *Introduction to the LHC Experiments*, in *Physics of the large and the small, TASI 09, proceedings of the Theoretical Advanced Study Institute in Elementary Particle Physics, Boulder, Colorado, USA, 1-26 June 2009*, pages 489–518 (2011)

[76] G. L. Bayatian, et al. (CMS Collaboration), *CMS technical design report, volume II: Physics performance*, J. Phys. **G34(6)**, 995 (2007)

[77] K. Aamodt, et al. (ALICE Collaboration), *The ALICE experiment at the CERN LHC*, JINST **3**, S08002 (2008)

[78] S. Amato, et al. (LHCb Collaboration), *LHCb technical proposal* (1998)

[79] ATLAS Experiment - Public Results, *LuminosityPublicResultsRun2* [Online, accessed 28.03.2017] `https://twiki.cern.ch/twiki/bin/view/AtlasPublic/LuminosityPublicResultsRun2`

[80] G. Aad, et al. (ATLAS Collaboration), *The ATLAS Experiment at the CERN Large Hadron Collider*, JINST **3(08)** (2008)

[81] Y. Nakahama, *The ATLAS Trigger System: Ready for Run-2*, J. Phys.: Conf. Ser. **664(8)** (2015)

[82] G. Aad, et al. (ATLAS Collaboration), *Technical Design Report for the Phase-I Upgrade of the ATLAS TDAQ System*, Technical Report CERN-LHCC-2013-018. ATLAS-TDR-023 (2013)

[83] S. Haywood, et al. (ATLAS Collaboration), *ATLAS inner detector: Technical design report. Vol. 2* (1997)

[84] Hugging, F., et al. (ATLAS Collaboration), *The ATLAS Pixel Insertable B-Layer (IBL)*, Nucl. Instrum. Meth. **A650**, 45 (2011)

[85] A. Airapetian, et al. (ATLAS Collaboration), *ATLAS calorimeter performance Technical Design Report* (1996)

[86] K. Sliwa (ATLAS), *ATLAS Overview and Main Results*, Proceedings, International School on High Energy Physics: Workshop on High Energy Physics in the near Future. (LISHEP 2013): Rio de Janeiro, Brazil, March 17-24, 2013 (2013), `hep-ex1305.4551`

[87] ATLAS Collaboration, *ATLAS muon spectrometer: Technical design report* (1997)

[88] A. C. Caldwell, D. Kollár, K. Kröninger, *BAT - The Bayesian Analysis Toolkit*, J. Phys.: Conf. Ser. **219(3)**, 032013

[89] M. Cacciari, G. P. Salam, G. Soyez, *The Anti-k(t) jet clustering algorithm*, JHEP **04**, 063 (2008)

[90] J. Gaiser, *Charmonium Spectroscopy From Radiative Decays of the J/ψ and ψ'*, Ph.D. thesis, SLAC (1982), [Online, accessed 14.03.2017] `http://www-public.slac.stanford.edu/sciDoc/docMeta.aspx?slacPubNumber=slac-r-255.html`

[91] M. Oreglia, *A Study of the Reactions $\psi' \to \gamma\gamma\psi$*, Ph.D. thesis, SLAC (1980), [Online, accessed 14.03.2017] `http://www-public.slac.stanford.edu/sciDoc/docMeta.aspx?slacPubNumber=slac-r-236.html`

[92] G. Aad, et al. (ATLAS), *Muon reconstruction performance of the ATLAS detector in proton - proton collision data at $\sqrt{s}$ =13 TeV*, Eur. Phys. J. **C76(5)**, 292 (2016)

Danksagung

Zunächst möchte ich mich bei Prof. Arnulf Quadt und Dr. Boris Lemmer für die außerordentliche Unterstützung während meiner gesamten Zeit im II. Physikalischen Institut danken. Mit zahlreichen hilfreichen Tipps haben sie diese Arbeit möglich gemacht und wesentlich zu meinem persönlichen Fortschritt beigetragen. Vielen Dank! Ebenso bedanke ich mich bei meinen Kollegen aus dem II. Physikalischen Institut, welche mir im täglichen Umgang, nicht zuletzt der Kaffepause, Freude an der Arbeit bereitet und so zu einer langzeitigen Motivation beigetragen haben.

Einen nicht unwesentlichen Beitrag haben Helen und meinen Eltern geleistet. Sie haben mich bei meinen Entscheidungen unterstützt und mir mit Rat und Tat in kritischen Situationen zur Seite gestanden. Ohne einen so guten Rückhalt wäre mir die Konzantration auf die Arbeit und mein gesamtes Studium deutlich schwerer gefallen. Vielen lieben Dank!

Erklärung nach §17(9) der Prüfungsordnung für den Bachelor-Studiengang Physik und den Master-Studiengang Physik an der Universität Göttingen:

Hiermit erkläre ich, dass ich diese Abschlussarbeit selbständig verfasst habe, keine anderen als die angegebenen Quellen und Hilfsmittel benutzt habe und alle Stellen, die wörtlich oder sinngemäß aus veröffentlichten Schriften entnommen wurden, als solche kenntlich gemacht habe.
Darüberhinaus erkläre ich, dass diese Abschlussarbeit nicht, auch nicht auszugsweise, im Rahmen einer nichtbestandenen Prüfung an dieser oder einer anderen Hochschule eingereicht wurde.

Göttingen, den 27. Juni 2017

(Fabian Sohns)